Modeling Piezoelectric Wave Energy Harvesters and Novel Carbon Capture Solid Sorbents

by
Mahpara Habib

Submitted to the Graduate Faculty of

the Swanson School of Engineering in partial fulfillment

of the requirements for the degree of

Doctor of Philosophy

University of Pittsburgh
2023

UNIVERSITY OF PITTSBURGH
SWANSON SCHOOL OF ENGINEERING

This dissertation was presented by
Mahpara Habib

Defended on
May 12, 2023
And approved by

Markus Chmielus, Ph.D., Professor, Mechanical Engineering and Materials Science

Jeffrey Vipperman, Ph.D., Professor, Mechanical Engineering and Materials Science

Debangsu Bhattacharyya, Ph.D., Professor, Chemical and Biomedical Engineering, West Virginia University

Dissertation Director: Katherine Hornbostel, Ph.D., Professor, Mechanical Engineering and Materials Science

Acknowledgements

I would like to express my heartfelt gratitude to my thesis advisor, Dr. Katherine Hornbostel, for her invaluable mentorship throughout my PhD journey. Dr. Hornbostel has not only shared with me her immense expertise on the subject of my research and provided me with learning opportunities and challenges that have helped me to build new skills, but also provided me with the moral support and counsel required to complete this program. I am thankful to Dr. Debangsu Bhattacharyya and his lab at West Virginia University for helping me to learn how to design a fixed bed adsorber model for carbon capture. I would also like to thank Michael Matuszewski for offering his valuable feedback and expert guidance on my work on the FLECCS project.

I would like to express my gratitude to my doctoral committee, which consists of the following members: Dr. Jeffrey S. Vipperman (ME, Pitt)), Dr. Markus Chmielus (MSE, Pitt), Dr. Debangsu Bhattacharyya (Chem. & Biomed. Engr, WVU) and Dr. Katherine Hornbostel (ME, Pitt). Thank you for providing me with the guidance and suggestions that helped me to better define my work.

I would like to acknowledge Mascaro Center for Sustainable Innovation (MCSI) for funding my work on the piezoelectric energy harvesting project. I would also like to acknowledge ARPA-E for funding the research on the carbon capture fixed bed adsorber model under the program Flexible Carbon Capture and Storage (FLECCS)-Phase 1 (grant number DE-AR0001308).

I would like to thank my fellow students at the University of Pittsburgh for sharing their knowledge and experience as we tackled the hurdles faced during our coursework and while

conducting research. I would especially like to thank my lab mates, Joanna Rivero, Austin Lieber and Iza Lantgios, for always being helpful and supportive, as well as being the group of people who have lent a sympathetic ear during times of stress and pressure.

Last but not the least, I am grateful to my parents for their encouragement and support of my academic pursuits. I would especially like to thank my spouse, without whose constant support I would not have been able to come this far. This work is dedicated to my father, who will forever serve to be my inspiration for striving to do my best.

Modeling Piezoelectric Wave Energy Harvesters and Novel Carbon Capture Solid Sorbents

Mahpara Habib, PhD

University of Pittsburgh, 2023

The aim of this thesis is to explore ways to mitigate climate change, namely by establishing new methods to harvest renewable energy and by enhancing carbon capture processes. The first part of this thesis explores the different classes of piezoelectric materials (ceramics, polymers and composites) from a materials science viewpoint and suggests the applications they are best suited for based on each class's strengths and weaknesses, with particular emphasis on sensor and energy harvesting applications. It is concluded that since composite materials can be tailor-fit to possess the most desirable set of properties needed for any given application, these are the class of piezoelectric materials that hold the greatest promise moving forward. Next, this thesis presents two piezoelectric energy harvester models that can be used to harvest wave energy for powering ocean observation buoys. The direct wave piezoelectric energy harvester model places piezoelectric elements in direct contact with ocean waves, which mechanically deform the flexible polyvinylidene difluoride (PVDF) elements to produce electrical energy. The indirect wave piezoelectric energy harvester, on the other hand, has its piezoelectric elements placed above water level and is indirectly excited by wave motion transferred to them via a frequency conversion mechanism. It is found that the indirect wave piezoelectric energy harvester produces better voltage and power output and thus has lower cost and volume associated with it. The last part of this thesis discusses the design of a fixed bed adsorber model packed with metal organic framework (MOF) solid sorbents, which can be retrofitted to a natural gas combined cycle (NGCC) power plant. This solid sorbent system can operate in two different modes to adsorb carbon dioxide emissions from the power plant, as well as from air during off-peak operation. It is shown that the solid sorbent system, when working in conjunction with a carbon capture membrane system, can achieve near-net zero carbon footprint for the NGCC power plant. The projects involved in this thesis share the common goal to curb global warming and climate change by promoting the use of clean energy and reducing the level of CO_2 emissions.

Keywords: piezoelectric materials, piezoelectric energy harvesting, ocean wave energy, carbon capture, direct air capture, fixed bed reactor modeling

Table of Contents

List of Tables

List of Figures

1. Introduction

1.1. Executive Summary

Although solar and wind energy are rapidly getting adopted, wave energy is a relatively untapped renewable power source that requires further research. On the fossil side of climate change mitigation, natural gas remains the cheapest and most practical source of energy to-date, but carbon capture technology is needed to make it environmentally sustainable long-term. The over-encompassing goal of this PhD thesis is to address climate change mitigation with a two-pronged approach: renewable power production and carbon capture. The first part of this thesis focuses on modeling piezoelectric materials for wave energy harvesting, while the second part focuses on modeling solid sorbents for direct air carbon capture. Chapters 2 and 3 of this thesis (which correspond to two first-author journal papers, listed below) will be on the topic of piezoelectric energy harvesters. Chapter 4 of this thesis (which corresponds to one first-author journal paper), is on the topic of metal-organic-framework packed bed modeling for direct air capture. Each of these projects is described in more detail in the following paragraphs.

The first part of the thesis is based on my published first-author review paper on piezoelectric materials, which can be sub-divided into three major classes of materials---ceramics, polymers and composites. The most prominent materials under each class, their piezoelectric properties, strengths and weaknesses, applications and most recent advances are examined. Comparisons are made between the material classes, as well as among the materials within each class. Ceramic piezoelectric materials are shown to possess very strong piezoelectric

properties. On the other hand, though piezoelectric polymers exhibit weaker piezoelectric properties in general, they are flexible and lightweight and can offer a great variety of uses such as wearable electronics and biomedical applications. The review concludes that composite piezoelectric materials are the most versatile and effective piezoelectric materials due to the ability to optimize and tailor-fit their properties to the desired application, and further research is encouraged into composite piezoelectric materials to promote more efficient renewable energy harvesting.

The next section of this work involves developing a piezoelectric energy harvester that is capable of harvesting energy from water waves. Two separate 2-dimensional models of piezoelectric energy harvesters made from flexible polyvinylidene difluoride (PVDF) were developed. The first model is a direct wave energy harvester, where the piezoelectric device is directly impacted by the waves and produces electric energy. The second model involves an indirect harvester that is excited and set into motion by the waves but is not in contact with them directly. The ultimate goal of both models was to maximize the voltage and power outputs of a novel piezoelectric wave energy harvester that could be used to supply renewable energy to ocean observation buoys.

The third part of this thesis covers the work done in developing a carbon capture system to remove CO_2 from the exhaust of a natural gas combined cycle (NGCC) power plant as well as direct air capture (DAC) the atmosphere. This system is a part of a hybrid carbon capture system that combines a membrane-based carbon capture system with a packed bed direct air capture system. This is to be retrofitted to a natural gas combined cycle (NGCC) power plant, with the goal of achieving negative CO_2 emissions. The solid sorbent packed bed will operate in two

modes: 1) removing CO_2 from just the membrane exhaust (normal operation), and 2) removing CO_2 from air in addition to the membrane exhaust (off-peak operation). An isotherm model for the sorbent used in the system was developed at first in order to define its adsorption behavior. A direct air capture model was designed and optimized in order to maximize the amount of carbon captured.

1.1.1. Intellectual Merit

The projects undertaken for this thesis contribute to the establishment of clean energy production. The first part of this thesis focuses on reviewing piezoelectric materials that are used for energy harvesting as well as sensing applications. An abundance of reviews exist that explore piezoelectric materials, their fabrication methods and their applications. However, this review paper offers a fresh perspective by not only providing a comprehensive overview of the existing piezoelectric materials, but also by classifying them into materials classes and comparing the strengths and weaknesses of each class. This in turn will help the reader to identify which set of piezoelectric materials are the best candidates for certain applications, as well as the set of piezoelectric materials that hold the greatest potential for future applications. The next section of this thesis presents work done on modeling piezoelectric energy harvesters that can potentially be used to harvest energy from water waves, with the purpose of supplying power to observation buoys deployed at sea. Although piezoelectric energy harvesters made from flexible PVDF have previously been studied for water wave or vortex energy harvesters, to my knowledge, it has yet to be shown that an indirect harvester, such as the one presented in this thesis, can result in better power output as well as a more practical design for an energy harvester

deployed at sea. Moreover, to my knowledge, no study exists on how the frequency of vibrations affects the power output of bimorph PVDF energy harvesters. The work presented in this section explores these topics and aims to produce results that can help optimize the design of the wave energy harvester. On the other hand, the work presented here on the fixed bed solid sorbent carbon capture model is the first of its kind because it seeks to not only capture CO_2 from the exhaust of the power plant, but also from atmospheric air during the off-peak operational hours of the power plant. The purpose of this model is to optimize the capture of CO_2 by the DAC system, thus enabling overall negative CO_2 emissions by the power plant. The results of this work will promote the practicality of establishing DAC systems retrofitted to existing fossil-fuel power plants.

1.1.2. Broader Impact

The projects undertaken for this thesis are designed to have a positive impact on the environment. It has already been stated that the work done on piezoelectric energy harvesters and direct air capture was driven by the need to establish clean energy sources and production methods. The first part of this thesis, which involves the review paper on piezoelectric materials, intends to inform the audience about the classes of piezoelectric materials available for energy harvesting, as well as to identify which materials are best suited to energy harvesting applications. The project on investigating piezoelectric energy harvesters seeks to establish a way to extract energy from waves and can potentially be used to power ocean observation buoys that provide valuable data. On the other hand, the work done on the direct air capture system project intends to not just reduce the amount of CO_2 being released into the atmosphere by the power

plant it is attached to, but also to capture CO_2 directly from the air, thus supporting large-scale initiatives such as the Paris Agreement. All three projects involved in this thesis, hence, have been designed to promote clean energy and to curb the effects of global warming.

1.1.3. Hypotheses

The first part of this thesis, which is the review on piezoelectric materials, helped to gather detailed knowledge regarding suitable materials for piezoelectric energy harvesting and thus aided in making an informed decision regarding the design and materials choice for the energy harvesters used for ocean wave energy harvesting in the second part of the thesis. It can be noted that the two research projects involved in this thesis were almost entirely based on modeling work. These projects were designed to lay down the groundwork for establishing the efficacy of the device or system modeled. The hypotheses for these projects are as follows:

Design Exploration of Piezoelectric Energy Harvesters For Buoys:

> Piezoelectric energy harvesting from ocean waves, using a flexible piezoelectric energy harvesting device, can provide auxiliary power to run equipment aboard an ocean observation buoy.

Flexible Carbon Capture Using MOF Fixed Bed Reactors at an NGCC Plant:

> A natural gas combined cycle power plant can be retrofitted with a hybrid carbon capture system consisting of a membrane system and a sorbent-based adsorber system in order to produce negative CO_2 emission from the plant.

Details of how these hypotheses have been tested and whether they have been established or refuted are provided in each of the relevant chapters. Chapter 3 discusses the project on piezoelectric energy harvesting for buoys and chapter 4 the project on carbon capture using MOF solid sorbents.

1.2. Publications and Conferences

Publications

- **Mahpara Habib,** Iza Lantgios**,** Katherine M. Hornbostel, "A Review of Ceramic, Polymer and Composite Piezoelectric Materials", *Journal of Physics D: Applied Physics*, Aug. 2022. (doi.org/10.1088/1361-6463/ac8687)
    - Chapter 2 of this PhD Thesis
- **Mahpara Habib,** Aaron M. Esquino, Austin Lieber, Trevone Jon-William Quarrie, Katherine M. Hornbostel, "Design Exploration of Piezoelectric Energy Harvesters For Buoys".
    - Submitted to *Applied Ocean Research* on May 2, 2023
    - Chapter 3 of this PhD Thesis
- **Mahpara Habib,** Aaron M. Esquino, Ryan Hughes, Debangsu Bhattacharyya, Frits Byron Soepyan, Michael S. Matuszewski, Zhien Zhang, Md Emdadul Haque, David R. Luebke, Leo R. Nemetz, G. Glenn Lipscomb, Katherine Hornbostel, "Flexible Carbon Capture Using MOF Fixed Bed Reactors at an NGCC Plant".
    - Submitting response to reviewers at *International Journal of Greenhouse Gases* by May 10, 2023
    - Chapter 4 of this PhD Thesis
- Frits Byron Soepyan, **Mahpara Habib,** Leo R. Nemetz, Debangsu Bhattacharyya, Zhien Zhang, Md Emdadul Haque, Aaron M. Esquino, Joanna R. Rivero, G. Glenn Lipscomb,

Michael S. Matuszewski, Katherine Hornbostel, “Optimization of a Natural Gas Power Plant with Membrane-Based and Solid Sorbent-Based Carbon Capture Systems to Achieve High Carbon Capture and Near-Zero Emission”.

- Submitted to Industrial & Engineering Chemistry Research on April 21, 2023 and currently under review

Conferences

- Poster: “Harvesting Energy from Hurricane Waves”, **Mahpara Habib**, Katherine Hornbostel, *Engineering Sustainability 2019.*
- Poster: “Modeling Piezoelectric Wave Energy Harvesters for Powering Ocean Observation Buoys”, **Mahpara Habib**, Austin Lieber, Aaron M. Esquino, Trevone Jon William Quarrie, Katherine Hornbostel, *Ocean Visions Summit 2023.*
- Presentation: “Retrofitting Direct Air Capture Systems to Natural Gas Combined Cycle and Nuclear Power Plants”, **Mahpara Habib**, Iza Lantgios, Katherine Hornbostel, *2023 AIChE Annual Meeting*. (Abstract submitted)

2. A Review of Ceramic, Polymer and Composite Piezoelectric Materials for Energy Harvesting

Piezoelectric materials have been studied for nearly a century now. Initially employed in sonar technology, piezoelectric materials now have a vast set of applications including energy harvesting, sensing and actuation, and have found their way into our everyday lives. Piezoelectric material properties are being further enhanced to improve their performance and be used in novel applications. This review provides an overview of piezoelectric materials, and offers a material science and fabrication perspective on progress towards the development of practical piezoelectric energy harvesters and sensors. Piezoelectric materials have been divided into the three following classes for this review: ceramics, polymers and composites. The prominent materials under each class are examined and compared, with a focus on their linear piezoelectric response in the d_{33} mode. The three classes of piezoelectric materials are also compared qualitatively for a range of metrics, and the applications that each material class are best suited for is discussed. Novel piezoelectric materials such as ferroelectrets and nanogenerator devices are also reviewed here. It is shown that ceramic piezoelectric materials have strong piezoelectric properties but are stiff and brittle, whereas polymer piezoelectric materials are flexible and lightweight but do not exhibit very good piezoelectric performance. Composite materials are concluded to possess the advantages of both ceramic and polymer materials, with room to tailor-fit properties by modifying the structure and composition.

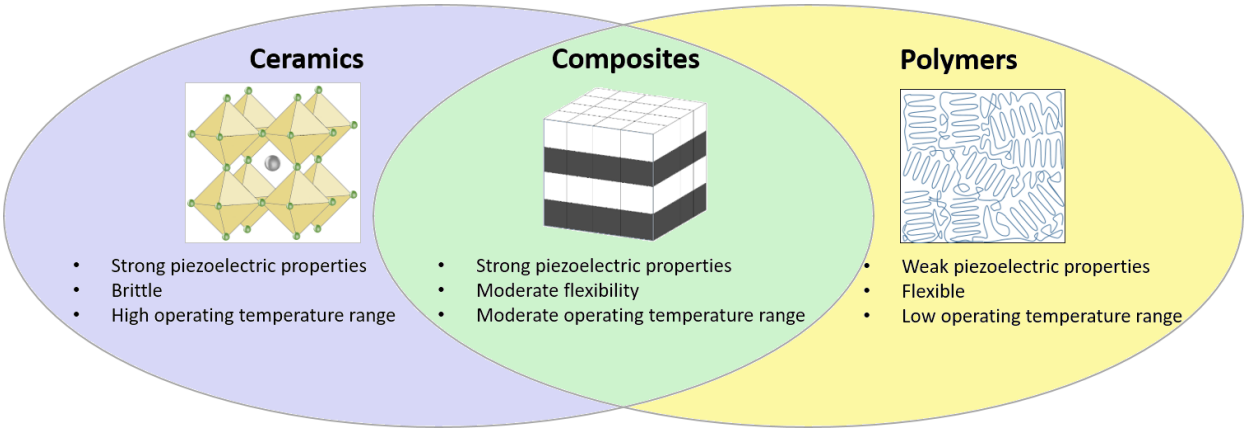

Figure 1: Classification of the different piezoelectric materials explored in this review paper. Ceramics possess higher piezoelectric properties and operating temperatures than polymers, while polymers possess higher flexibility than ceramics. Composites possess the benefits of both the ceramic and polymer classes.

2.1. Nomenclature

Acronyms

AD	Aerosol deposition
AlN	Aluminum nitride
BCZT	$(Ba,Ca)(Zr,Ti)O_3$
BNT	Bismuth sodium titanate
BT	Barium titanate
FOM	Figure of merit
GSV	Granular spray in vacuum

KNN	Potassium sodium niobate
MEMS	Microelectromechanical system
PDMS	Polydimethylsiloxane
PEH	Piezoelectric energy harvester
PENG	Piezoelectric nanogenerator
PMN-PT	Lead magnesium niobate-lead titanate
POPh	Polyorganophosphazene
PVDF	Polyvinylidene difluoride
PVDF-TrFE	Poly(vinylidene fluoride-co-trifluoroethylene)
PZT	Lead zirconate titanate
WSN	Wireless sensor network

Symbols

d_{31}	Piezoelectric constant in the transverse mode
d_{33}	Piezoelectric constant in the longitudinal mode
g_{31}	Voltage constant in the transverse mode
g_{33}	Voltage constant in the longitudinal mode
k_p	Electromechanical coupling constant

T_c Curie temperature

2.2. Introduction

2.2.1. Concept of Piezoelectricity

Piezoelectricity may be defined as the linear interaction between mechanical and electrical energy that occurs in specific types of crystals that lack inversion symmetry, or in other words, have a non-centrosymmetric structure [1]. Piezoelectric materials react to mechanical stress by producing an electrical potential (the direct piezoelectric effect), and produce mechanical strain in response to an applied electrical field (the indirect piezoelectric effect) [2]. The direct piezoelectric effect as a function for stress can be defined by the following equation:

$$D_k = d_{kij} T_{ij} \tag{2-1}$$

where D_k is the electric displacement tensor given in units of [C m^{-2}], d_{kij} is the piezoelectric charge coefficient tensor of the material in [C N^{-1}], and T_{ij} is the stress tensor in [N m^{-2}]. The indirect piezoelectric effect, on the other hand, is defined by the following equation:

$$S_i = d_{ijk} E_{jk} \tag{2-2}$$

where S_i is the strain tensor [dimensionless], d_{ijk} is the piezoelectric strain coefficient tensor of the material in [m V^{-1}], and E_{jk} is the applied electric field tensor in [N C^{-1}].

The aspect of piezoelectricity that has been most studied, and will be the emphasis of this review is the linear response in the longitudinal mode ('d_{33}'). It is, however, useful to recognize that linear piezoelectricity displays higher degrees of coupling than just this. Materials with high piezoelectric response in one direction typically have high piezoelectric response in other directions, so the results and trends presented in this review are generally applicable to other cases as well.

2.2.2. Principles of Piezoelectricity

2.2.2.1. General Mechanism of Piezoelectricity in Crystalline Materials

Piezoelectricity occurs in materials that possess a non-centrosymmetric crystal structure. Twenty out of the existing thirty-two crystal classes can possess piezoelectric properties. For example, quartz and berlinite are two naturally occurring piezoelectric materials whose crystallinity lacks a center of symmetry, thus allowing them to be naturally piezoelectric. On the other hand, engineered materials such as barium titanate and lead zirconate titanate have to be poled in order for them to exhibit piezoelectricity [2]. Perovskite materials, which are crystalline materials that have the formula ABX_3, are particularly effective at being poled to yield enhanced piezoelectric properties. [2].

The concept of crystallinity and piezoelectricity can be explained very simply. In Figure 2, a non-centrosymmetric molecule is shown, whose center of negative and positive charges coincide and result in a neutral molecule. However, when it undergoes compressive forces, its

centers for negative and positive charges separate, thus producing a dipole. This is how pressure or deformation causes piezoelectric materials to produce an electric field.

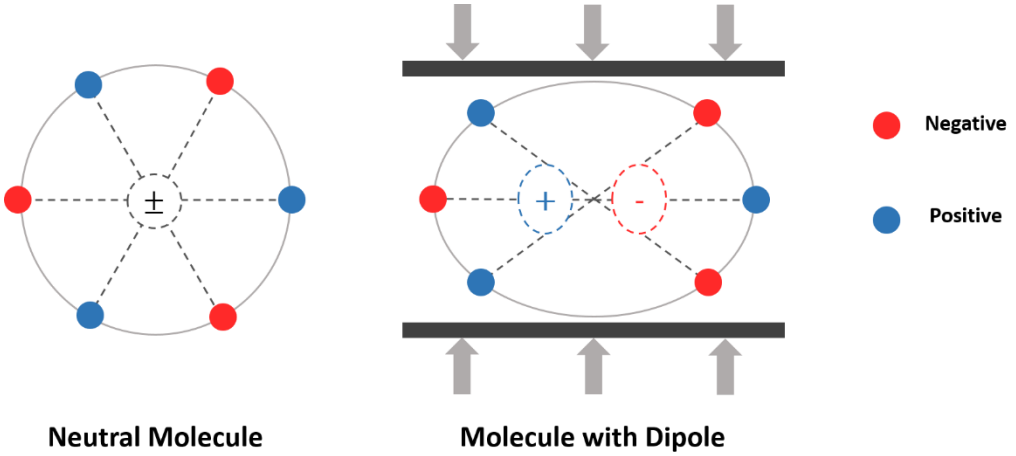

Figure 2: Graphic depiction of how compressive forces can result in polarization of a molecule and produce an electric field

*2.2.2.2. **Poling***

Poling is the process of imparting or enhancing existing piezoelectric properties of a material by subjecting it to high temperature and a high electric field [1]. Under normal circumstances, the dipoles of a material are randomly oriented and thus cancel each other out to eliminate any pronounced piezoelectric effect. Applying an electric field that is higher than the saturation field but lower than the breakdown field causes the dipoles to align [3]. The temperature is elevated to facilitate the shifting and rearrangement of the dipoles, but is kept below the Curie temperature. This causes the dipoles to align and create directionality within the

material. In order to retain this effect, the material is cooled down in the presence of the high electric field. Two of the most popular methods for poling are contact poling and corona poling (Figure 3). In contact poling, the bulk material is sandwiched between two electrodes and subjected to a current [4]. Cooling occurs in the presence of the electric field so as to preserve the dipole alignment [5]. In corona poling, only one side of the material is connected to an electrode while the other surface is free. A sharp corona tip is held at a high voltage in the range of kilovolts right above that free surface, while the material itself is supplied with a low voltage by the electrode. The highly charged tip ionizes the gas molecules around it, which then accelerate towards and deposit themselves on top of the material's free surface, thus poling the material [6].

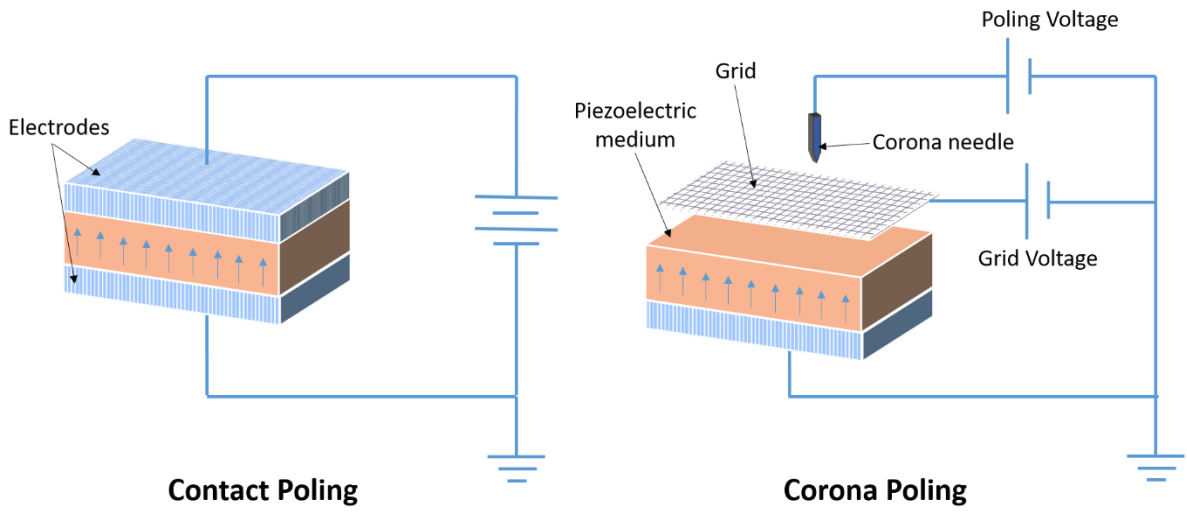

Figure 3: Contact poling versus corona poling

2.2.2.3. *Bending Modes (d_{31} and d_{33})*

There are two primary modes of operation for a piezoelectric material as shown in Figure 4. The d_{33} mode, also known as the longitudinal mode, is the operation mode where the direction of polarization and the direction of stress are parallel. The d_{31} mode, or the transverse mode, on the other hand, is the mode where the polarization direction and the direction of applied stress are perpendicular to each other [1]. Piezoelectric materials have different values for metrics (e.g. piezoelectric constant and voltage constant) for these two bending modes. In general, it can be stated that d_{33} is of higher value than d_{31} and thus a larger voltage may be yielded when bending in this mode [7]. Thus, the d_{33} mode is preferred for applications such as piezoelectric energy harvesting.

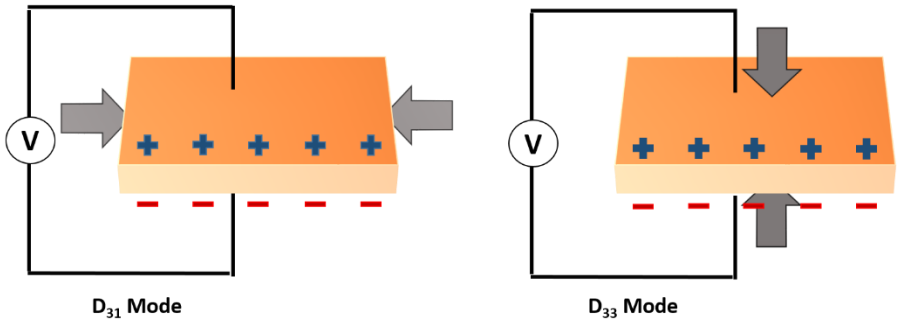

Figure 4: Primary bending modes for piezoelectric materials: d_{31} (left) and d_{33} (right)

2.2.2.4. *Figures of Merit (FOMs)*

Figures of Merit (FOMs) are a means of gauging and comparing the properties of piezoelectric materials. Piezoelectric material FOMs enable the selection of optimum materials

based on the targeted application. For example, the FOMs to be compared for sensors differ from those of actuators [8]. Since the focus of this paper is to primarily discuss piezoelectric materials and their linear behavior in the bending mode, the FOMs discussed have been assumed to be in that mode and defined without any further reference to the direction of bending. The three FOMs that are of importance for piezoelectric energy harvesters and sensors are listed below:

- Piezoelectric Charge/Strain Constant: *d*, used to denote the piezoelectric charge constant here, is defined as the relation between the charge density, *x*, induced by an applied mechanical stress, *T*. Alternatively, d can also be defined as the relation between the strain, *S*, which results when an external electric field, *E*, is applied. This FOM is important in both energy harvesting and actuator applications. The equations for the piezoelectric constant are given below:

$$d = \frac{x}{T} \tag{2-3}$$

$$d = \frac{S}{E} \tag{2-4}$$

- Piezoelectric Voltage Constant: Used as an FOM in comparing piezoelectric sensors, the piezoelectric voltage constant, g, is used to define the relation between the induced electric field, E, and the external stress applied, T, as given by Equation (2-5) below. This is related to the piezoelectric charge coefficient through the Legendre transformation and does not possess a simple inverse relationship.

$$g = \frac{E}{T} \tag{2-5}$$

- Electromechanical Coupling Factor: Given by k^2, the electromechanical coupling factor is defined as the ratio of input and stored energies, both for the direct and reverse piezoelectric effect. This FOM plays a significant role in piezoelectric energy harvester applications. The equations for this FOM are given below:

$$k^2 = \frac{stored\ mechanical\ energy}{input\ electrical\ energy} \tag{2-6}$$

$$k^2 = \frac{stored\ electrical\ energy}{input\ mechanical\ energy} \tag{2-7}$$

Other FOMs that are of significance include the mechanical quality factor and the acoustic impedance. These FOMs are mainly used in the design of transducers and therefore will not be discussed in detail here.

2.2.3. Motivation for this Work

Piezoelectric materials hold great promise to be implemented in a wide range of practical applications. Ambient vibrational and kinetic energy--such as those found in wind or water waves or machinery vibrations--are abundant sources for potential piezoelectric energy harvesting. Energy scavenging from these sources via piezoelectric conversion could potentially lead to an alternate source of clean energy. In the case of MEMS devices and sensors, bulky energy sources like batteries prove to be a hindrance, especially due to having to be replaced repeatedly. Piezoelectric materials can be used to build self-powered wireless sensing devices that do not

need batteries and can be placed in remote locations. Piezoelectric materials also hold the promise of potential application in medical devices placed inside the body [1]. Materials that are biocompatible could find use in biomedical devices that either measure or regulate functions of the body.

The scope of this work is to provide the reader with a broad outlook on the existing piezoelectric materials and their potential applications, especially in the areas of sensing and energy harvesting. This work compares the different sub-classes of piezoelectric materials (ceramic, polymer, composite) and discusses their advantages and disadvantages. Advanced materials and their applications are also explored in this paper to bring the reader up to date with the current research being conducted on piezoelectric materials.

2.3. Piezoelectric Materials

2.3.1. Ceramic Piezoelectric Materials

Ceramic materials are perhaps the most widely used class of piezoelectric materials due to their affordability, stability and high piezoelectric performance. Piezoelectric ceramics mainly have a perovskite structure and are very often lead-containing compounds. However, lead-free piezoelectric ceramics, such as barium titanate ($BaTiO_3$) and potassium sodium niobate ($K_{0.5}Na_{0.5}NbO_3$), have been developed to avoid the hazardous properties of lead compounds. Ceramic piezoelectric materials have many advantages: excellent piezoelectric properties, low cost of manufacturing, simple fabrication techniques, and the ability to be rendered into a variety of shapes. For this reason, ceramic piezoelectric materials are prevalent in many applications, including transducers, sensors and actuators [9]. This section describes and compares the

properties of conventional piezoelectric ceramics to the properties of enhanced piezoelectric ceramics. Table 1 at the end of this section summarizes the comparison of properties of the ceramic piezoelectric materials that will be discussed in this section.

2.3.1.1. Common Piezoelectric Ceramics

2.3.1.1.1. Lead Zirconate Titanate (PZT)

Discovered in the early 1950's at the Tokyo Institute of Technology, lead zirconate titanate, $Pb(Zr_{1-x}Ti_x)O_3$ or PZT for short, is a perovskite-structured ceramic material that possesses superior piezoelectric properties. Bernard Jaffe's work on this newly discovered material in the next few years greatly accelerated its popularity as a piezoelectric material. PZT has a high electromechanical coupling coefficient (0.69) and high piezoelectric constant (360 pC N^{-1}) [10], which leads to higher conversion from mechanical to electrical energy. It also possesses the unique property of retaining its piezoelectric properties at high temperatures and has a Curie temperature of 350^{o}C [11]. In addition, PZT is chemically stable, mechanically robust and does not degrade in a humid environment, so it can be used in a wide range of applications. For example, PZT can be used in sensors that need to operate in a reactive environment, or in energy harvesting applications that require it to withstand large loads [12].

PZT has become the most widely used piezoelectric material, with applications ranging from aerospace vibration control to atomic force microscopy [13], [14]. The main advantage of PZT is its performance—typical voltage outputs can be as high as a hundred volts, though current output is on the order of nano and milli-amps [15]. Research is also being conducted to explore

the possibility of employing PZT micro-sensors for energy harvesting [16]–[19]. A few recent works using PZT have been described in more detail in the following sections.

One of the biggest disadvantages of PZT is that it is a bad fit for applications that require flexibility. Due to its high Young's modulus (65 GPa) and high density [11], it is brittle and is unable to undergo extensive deformation. Since bulk PZT is stiff, it has a high resonant frequency and thus is not suitable for harvesting energy from low frequency ambient vibrations. Additionally, since lead is considered hazardous to human health and the environment, the use of PZT in certain applications, such as devices implanted within the human body, is not possible [20].

2.3.1.1.2. Potassium Sodium Niobate (KNN)

Lead-free ceramic piezoelectric materials are a more environmentally-friendly alternative to PZT. Potassium sodium niobate, $K_{1-x}Na_xNbNO_3$ or KNN for short, is one such lead-free piezoelectric ceramic material. Although unmodified KNN has a low piezoelectric constant (ranging anywhere between 80-160 pC N^{-1}), modified structures can attain piezoelectric properties closer to that of PZT [21]. Saito et al. used the reactive template grain growth (RTGG) method to fabricate highly textured polycrystals of $(K,Na,Li)(Nb,Ta,Sb)O_3$ that possessed a high piezoelectric constant of 416 pC N^{-1}, comparable with that of PZT [22]. In a more recent work, Li et al. showed that the piezoelectric constant can be further enhanced to 550 pC N^{-1} by the combined effect of the RTGG method for texturing and the tuning of the polymorphic phase boundary by changing the concentration of $(Bi_{0.5}K_{0.5})HfO_3$ added into the matrix of $(K_{0.5}Na_{0.5})(Nb_{0.965}Sb_{0.035})O_3eCaZrO_3$ [23]. In another study by Li et al., a highly textured form of a similar KNN-based ceramics was fabricated and shown to have a piezoelectric constant of up to

700 pC N^{-1} and a high Curie temperature of 242 ^{o}C [24]. Though the high Curie temperature of KNN ceramics makes it usable in high temperature applications, KNN's greatest advantage is that it does not contain lead, and thus is safe for use in medical implants and energy harvesting [20].

2.3.1.1.3. Barium Titanate (BT)

Barium titanate, $BaTiO_3$ or BT, was the first perovskite-structured ferroelectric material to be discovered by scientists during World War II and became widely used in sonar detection and in phonograph needles [25]. It was initially known for its high capacitance (with a dielectric constant of 1100) [2]. However, it was not until later that the material was electrically-poled and shown to acquire piezoelectric properties [25]. Pure, unmodified BT has a low piezoelectric constant (191 pC N^{-1}) relative to PZT, a voltage constant of 11.4 x 10^{-3} V*m N^{-1} and a low Curie temperature of 130^{o}C [26]. However, electromechanical properties of BT ceramics have been greatly enhanced to give piezoelectric properties comparable to PZT. Reducing the domain size has resulted in dramatic improvement in BT's piezoelectric properties [26]. For example, hydrothermally grown BT with a grain size of the order 1-2 µm yielded a d_{33} value of 460 pC N^{-1} [27]. Another way to enhance BT's piezoelectric performance is by substituting in the A and B-sites of the perovskite crystal. Liu and Ren used this method to fabricate a binary system comprised of $Ba(Zr_{0.2}Ti_{0.8})\ O_{3-x}(Ba_{0.7}Ca_{0.3})TiO_3$(BZT–BCT) that possessed d_{33} values as high as 620 pC N^{-1} [28].

2.3.1.1.4. Bismuth Sodium Titanate (BNT)

Bismuth sodium titanate, $Bi_{0.5}Na_{0.5}TiO_3$ or (BNT), which possesses a perovskite structure, is a lead-free piezoelectric ceramic. Discovered in 1960 by Smolensky et al., BNT has excellent

piezoelectric properties for a lead-free ceramic [29]. For example, it has a piezoelectric constant of 75 pC N^{-1}. BNT has a depolarization temperature that can range up to 290 ^{o}C [30]. It has been found useful in actuator applications due to its high strain response. Adding dopants to BNT has been shown to enhance its piezoelectric properties. For example, $[Bi_{0.5}(Na_{1-x}Li_x)_{0.5}]0.84Sr_{0.16}TiO_3$ (BNLST-100x), which resulted from doping BNT with Li^+ and Sr^{2+} simultaneously, has a higher piezoelectric constant (173 pC N^{-1}) and high operating temperature (>300 ^{o}C) [31].

2.3.1.1.5. Aluminum Nitride (AlN)

Aluminum nitride (AlN), which has a wurzite crystal structure, is another lead-free alternative to PZT. Though it has a low piezoelectric constant of 5 pC N^{-1} [32], its advantages include a Curie temperature of greater than 1000^{o}C, stability in the presence of moisture, and better CMOS (complementary metal oxide semi-conductor) processing compatibility, which is why it is mostly applied in microelectromechanical system (MEMS) devices [33]. Its high thermal conductivity and low dielectric and acoustic losses make AlN thin films the perfect material for resonators and sensors [34]. AlN thin films are more prevalently used than AlN single crystal bulk material because it is easier to grow oriented thin films of AlN than high quality AlN single crystals [35]. For example, AlN thin films of thickness up to 2µm were deposited via a low-temperature sputter deposition method and gave a d_{33} value of up to 5.57 ± 0.34 pm V^{-1} [36].

2.3.1.1.6. Lithium Niobate

Lithium niobate ($LiNbO_3$) is another lead-free piezoelectric ceramic that has a very high Curie temperature exceeding 1000^{o}C [35], [37], [38]. This material has been widely applied in high temperature transducers because of it stability at elevated temperatures. Above the Curie

temperature, the material exists in the para-electric state and is not polarized, but below that temperature, the Li and Nb atoms are arranged between layers of oxygen atoms in such a way that spontaneous polarization occurs, i.e. it is in its ferroelectric state [37]. Although lithium niobate has a low piezoelectric constant relative to PZT (6 pC N^{-1}) [38], it has become a popular material for use in MEMS resonators due to its excellent electromechanical coupling and very high quality-factor [39]–[41]. Yang et al. have built a MEMS resonator using a lithium niobate thin film that has a mechanical quality factor of 406 and 474 for the fifth and seventh order asymmetric Lamb-wave modes respectively, the highest reported values for the K. frequency range for piezoelectric MEMS resonators [41].

2.3.1.2. Enhanced Piezoelectric Ceramics

2.3.1.2.1. $(Ba,Ca)(Zr,Ti)O_3$

PZT remains the most commonly used piezoelectric ceramic material, though concern for the effect of lead-based materials has caused increased demand for lead-free alternatives. However, lead-free ceramics do not have as high piezoelectric properties as PZT and thus are not proper substitutes for the material. It was, therefore, important to develop a lead-free ceramic that exhibits piezoelectric performance comparable to PZT.

$(Ba,Ca)(Zr,Ti)O_3$, or BCZT for short, was initially studied in 1954 for application in capacitors [42]. However, it was not until 2009 that Liu and Ren showed that BCZT had phenomenal piezoelectric properties, including a piezoelectric coefficient that is comparable to, if not greater than, PZT (the value changes with stoichiometry and grain size), thus making it one of the most popular lead-free piezoelectric ceramics available [43]. BCZT properties have been

shown to improve with the addition of dopants. Merselmiz et al. showed that BCZT combined with $BaTi_{0.89}Sn_{0.11}O_3$ (BTSn) led to enhanced properties, where adding 0.2BTSn to the system led to a d_{33} value of 228 pC N^{-1} [44]. Adding a BNT precursor prepared by the molten salt method to BCZT was shown to produce an optimal d_{33} value of 450 pC N^{-1} and a k_p value of approximately 53% [45]. In another work, Li et al. showed that doping BCZT with 0.5% amphoteric Tm^{3+} caused the dopant to occupy both A and B sites and increased the piezoelectric coefficient to 523 pC N^{-1} [46]. Unfortunately, BCZT's low Curie temperature (~102 ^oC) is its limiting factor and disqualifies it for applications needing a higher temperature range. Doping has also been used to improve the Curie temperature. Kumari et al. doped BCZT with Bi^{3+} and found that it increased T_c to 159 ^oC [46]. In another work, Zhang et al. found that doping with 0.1% $LiTaO_3$ increased the Curie temperature to 129 ^oC [47].

2.3.1.2.2. Zinc Oxide Nanogenerators

Piezoelectric energy conversion on the macroscale is mostly limited to sensing application due to low conversion efficiency, especially in the case of low frequency ambient vibrations. Nano-structured piezoelectric materials, on the other hand, can convert energy more efficiently than typical piezoelectric materials because they can withstand higher strain and thus are capable of producing a greater voltage output. Since voltage produced is directly proportional to strain, piezoelectric nanomaterials are generally capable of producing greater voltage for a given strain. Another contributing factor to the higher efficiency of nanoscale piezoelectric devices is that nanomaterials have high surface-to-volume ratio in comparison with bulk materials [48].

Zinc oxide (ZnO) nanostructures, typically of diameters ranging between 20-100 nm, exhibit good piezoelectric properties and have been used in self-powered nano-devices [49]. ZnO nanowire arrays have a larger effective piezoelectric constant than bulk ZnO [50]. It has been shown that the effective piezoelectric constant of ZnO nanowires increases steadily with increasing diameter [50]. Wang et al. [51] demonstrated that aligned ZnO nanowires can be formed on an α-Al_2O_3 substrate by the vapor-liquid-solid process. 10 μm^2 area of nanowires can produce enough power to run a single nanotube/nanowire based device. In another study by Zhou et al., ZnO piezoelectric fine wires (nano and microscale wires) were used to build a force/pressure trigger that created an electrical response in approximately 10 milliseconds when acted on by an external impact force [49]. The voltage generated had a lifetime of about 100 seconds and could thus be used as a piezoelectric field effect transistor (PE-FET). In a recent work by He et al., ZnO nanorods were synthesized on conducting textiles and were shown to be able to produce an output voltage of 1.81 V when shaken at a frequency of 26 Hz, enough to turn on an LCD display [52].

2.3.1.3. Enhanced Fabrication Methods

2.3.1.3.1. Aerosol Deposition and Granular Spray in Vacuum of PZT

It is a challenge to use batteries for powering extensive wireless sensor networks (WSN) due to the fact that batteries are bulky and have to be replaced periodically [53]. As such, powering individual sensor nodes with piezoelectric energy harvesting systems could be a promising solution [54]. Though zinc oxide nanogenerators (NG) have shown potential in harvesting energy from ambient mechanical vibrations [55][56], their relatively low power output makes them ineligible for powering WSN. Single-crystal piezoelectric materials generally have

high piezoelectric constants and thus are better candidates for harvesting energy [57], but the high fabrication cost of single crystals is an obstacle to scale-up [58]. Sol-gel deposition is cheap in comparison, but deposition must be halted after every 100 nm of spin-coated layer for heat-treatment to be applied, which results in a tedious process [59].

Aerosol deposition (AD) and granular spray in vacuum (GSV) have been shown to be particularly effective for the fabrication of thick film piezoelectric energy harvesters [60]. Hwang et al. devised a refined method for the aerosol deposition of PZT on a flexible polyethylene terephthalate (PET) substrate [58]. As shown in Figure 5, PZT granules were aerosol-deposited at room temperature on a sapphire substrate and built up to a thickness of 7 μm, which strikes a balance between optimum piezoelectric performance and flexibility. The deposited layer was then annealed at high temperatures (700-900^{o}C) to enhance the piezoelectric properties. The PZT film was transferred by an inorganic-based laser lift-off to a plastic substrate without any damage to the film. This PZT energy harvesting device was capable of producing an open-circuit voltage of 200 V and a short circuit current of 35 μA, and was able to light up 208 blue LEDs, as well as charge a super-capacitor. On the other hand, the granular spray in vacuum (GSV) deposition method has been shown to be an improved version of the aerosol deposition method, where the key difference lies in the fact that GSV uses free-flowing agglomerated powder as the feed so as to avoid agglomeration issues during deposition [60].

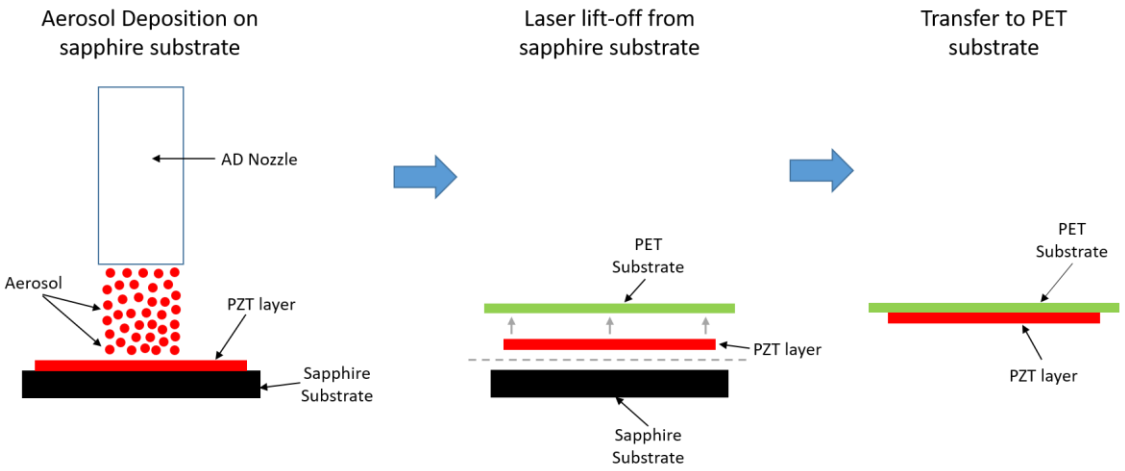

Figure 5: Aerosol deposition of PZT on a sapphire substrate followed by laser lift-off and transfer of PZT layer to a PET substrate, adapted from [58]

2.3.1.3.2. Micro-fabricated PZT

Micro-fabricated PZT has been employed in microelectromechanical systems (MEMS) for energy harvesting from ambient vibrations. The piezoelectric material is typically attached to a backing which acts as a cantilever, with a proof mass at the free end that amplifies vibrational motion. However, since the rigid backing has a high spring constant and thus a high resonant frequency, low frequency vibrations such as human body movements fail to excite it enough to produce adequate power. More flexible piezoelectric materials–such as polyvinylidene difluoride (PVDF)– have lower resonant frequencies, but also possess significantly lower dielectric and piezoelectric constants in comparison to PZT.

Cho et al. fabricated a flexible, microscale PZT cantilever that harvested energy in the d_{33} mode in order to produce a larger voltage than in the d_{31} mode, which is the more common mode for a cantilever setup [18]. Bulk micromachining was used to synthesize a multi-layered PZT

cantilever on a flexible polyimide layer. Inter-digitated electrodes were etched out on the surface of the cantilever and a silicon proof mass formed using KOH wet-etching on the backside. This flexible PEH was able to harvest energy from low frequency vibrations and yielded an output voltage of 1.2 V and a power output of 117 nW at a resonant frequency of 97.8 Hz and acceleration of 5 m s^{-2}. Figure 6 shows the setup for this device.

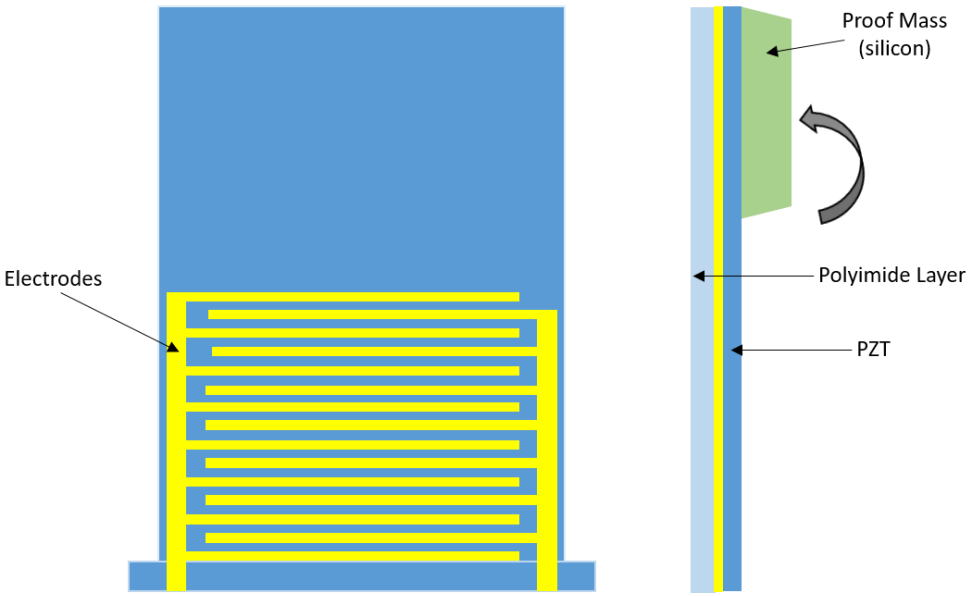

Figure 6: Schematic drawing of flexible PZT cantilever that harvests energy in the d_{33} mode, adapted from [18]

2.3.1.4. Shortcomings of Ceramic Piezoelectric Materials

Piezoelectric ceramic materials, in general, possess superior piezoelectric properties, such as high piezoelectric constant and high electromechanical coupling coefficients. This makes them

an ideal choice for energy harvesting applications, particularly in transducers. However, piezoelectric ceramics also have high Young's Modulus values, usually on the order of 10^9 N m^{-2}. These materials are extremely stiff, and consequently have high resonant frequencies. It is thus impractical to employ ceramic piezoelectric materials in energy harvesting from low frequency vibrations, such as vortex induced vibrations or ambient vibrations from vehicles or machinery. Moreover, repeated cycles of deformation can cause premature failure due to the brittleness of ceramic materials.

2.3.1.5. Summary of Ceramic Piezoelectric Materials

From Table 1, it is evident that PZT has the highest piezoelectric constant amongst all the ceramic piezoelectric materials compared in this section. $BaTiO_3$ and modified KNN also have good piezoelectric constants. However, when it comes to high-temperature performance, it seems that AlN and $LiNbO_3$ are better choices. On the other hand, applications where power generation isn't a high priority (e.g. MEMS power harvesting), innovative materials such as zinc oxide nanogenerators and micro-fabricated PZT are good options. With the exception of micro-fabricated PZT, all of the ceramic piezoelectric materials listed here have high Young's modulus values, and thus cannot be used in applications that require high deflection.

Table 1: Ceramic Piezoelectric Materials and their Properties

Material	Piezoelectric Constant, d_{33} ($pC\ N^{-1}$)	Voltage Constant, g_{33} ($V*m\ N^{-1}$)	Electromechanical Coupling Factor	Young's Modulus (GPa)	Curie Temperature (^oC)
PZT	360 [10]	0.025 [10]	0.6-0.7 [26][61]	65 [11]	350 [11]
KNN	80-160 [21]	0.0469 [62]	0.51 [63]	104 [63]	400 [21]
KNN-$LiSbO_3$	283 [64][65]	--	0.46 [65]	64.94 [20]	237 [24]
$BaTi0_3$	191 [26]	0.0114 [26]	0.49 [61]	67 [66]	130 [26]
BNT	75 [67]	--	~0.21 [68]	93.3 [69]	<290 [30]
AlN	5 [32]	0.1 [70]	0.23 [71]	344.83 [72]	>2000 [73]
$LiNbO_3$	6 [38]	0.023 [38]	0.23 [3]	202 [38]	1150 [38]
BCZT	>500 [43]	--	--	117.9 [74]	102 [74]
ZnO nanogenerators	9.2,12.4 [75][76]	0.13 [76]	--	40 [77]	--
Aerosol-deposited PZT	406 [58]	0.0495 [58]	--	60 [58]	--
Micro-fabricated PZT	--	--	--	3.4 [18]	--

2.3.2. Bulk Piezoelectric Polymers

Polymers are not typically associated with piezoelectricity. It was not until the late 1960's that Kawai et al. [78] discovered that polymers could exhibit piezoelectric performance significant enough for practical applications. In order for polymers to be piezoelectric, they must possess molecular dipoles in their structure [1]. Piezoelectric polymers can be either semi-crystalline or amorphous. Semi-crystalline polymers, such as polyvinylidene difluoride (PVDF) and its copolymers, are a mixture of tiny ferroelectric crystals that are suspended in an amorphous matrix [79]. When these polymers are poled, their dipoles reorient and align themselves to give the material pronounced piezoelectric properties. On the other hand, amorphous polymers also possess dipoles, but they do not possess long-range order amongst themselves. These polymers do not achieve a state of thermal equilibrium after poling like semi-crystalline polymers. Rather, their dipoles are locked into a quasi-stable state [80]. The next sections will briefly explore examples of the two types of polymers categorized broadly under conventional and more enhanced piezoelectric polymers.

2.3.2.1. Common Piezoelectric Polymers

2.3.2.1.1. PVDF

Polyvinylidene difluoride, or PVDF for short, was discovered in 1969 [78]. It is a semi-crystalline polymer in which the crystallites are comprised of aligned chains that form dipoles. This crystalline structure is then surrounded by an amorphous matrix. PVDF has been a particularly effective piezoelectric polymer due to its relatively high piezoelectric coefficient among other polymer materials. It also possesses excellent electromechanical response, is

chemically stable and has low acoustic impedance [81]. Poled PVDF has a piezoelectric coefficient of -24 to -34 pC N^{-1} [82]. It notably has a negative d_{33} value, which means that PVDF compresses instead of expanding upon being subjected to an electric field, the common response of other piezoelectric materials being expansion. Though PVDF has a high level of crystallinity (around 50-60%), it still requires stretching before it is poled in order to align the molecular chains to enhance its piezoelectric properties [25].

PVDF has several phases, of which the α and β phases are the most prominent. The α phase is the most stable phase and exists when the polymer solidifies from the melt. It is, however, non-polar because its structure, where hydrogen and fluorine are alternated in position on the carbon chain, results in no dipole moment. The β phase, on the other hand, results in non-zero dipole moment because hydrogen and fluorine atoms are positioned on opposite sides of the carbon chain, thus making this phase polar [81]. However, in order for the β phase to form, a high level of crystallinity must be achieved first. In order for the β phase to dominate, PVDF must first be poled. This is also promoted by the introduction of group defects, which enhances the piezoelectric properties of PVDF [4], [83]. Certain fabrication methods for PVDF, such as ionic liquid-assisted fused deposition modeling (FDM), can help promote the formation of the β phase, thus eliminating the necessity of poling. This method, recently developed by Liu et al., 3D prints PVDF with as high as 98.3% content of the β phase [84]. This 3D printed PVDF device had an output voltage of 4.7 times that of the device made from flat PVDF and a current density of 17.5 nA cm^{-2}.

PVDF has found many applications due to its flexibility and good piezoelectric properties. For example, it has been developed into a highly efficient piezoelectric fabric by Soin et al., which

has the potential to be applied to the apparel industry in the form of wearable piezoelectric energy harvesters [85]. In this material, the β phase PVDF monofilaments have been used as the spacer yarn and Ag-coated polyamide multifilaments have been used as the electrodes. This fabric can achieve impressive power densities of up to 1.1-5.1 mW cm^{-2} at pressures of 0.02-0.10 MPa. PVDF also has potential for application in biomedical engineering because of its biocompatibility. Damaraju et al. [86] tested electrospun PVDF as a scaffold for bone tissue engineering. They found that increasing the accelerating voltage during electrospinning increased the formation of the β-phase in PVDF and thus its piezoelectric properties. They also found that the PVDF scaffolding supported the osteogenic differentiation of human mesenchymal stem cells (MSCs).

While the works mentioned previously focus on harvesting energy for small-scale applications, Hudzik investigated how to employ small PVDF devices for macroscale power generation from hydrokinetic energy from riverbeds [87]. A conical kite, which "caught" the flow of the fluid, was attached to the free end of a cantilever beam, which oscillated when the fluid set the contraption into motion. Subsequently, energy was produced via piezoelectric conversion from the deflection of the PVDF beam, as well as from an electromagnetic inductor excited by the oscillations of the same beam.

2.3.2.1.2. PVDF-TrFE

PVDF-TrFE, poly(vinylidene fluoride-*co*-trifluoroethylene), is a copolymer of PVDF that is exceptional because it does not need to be poled in order for it to be piezoelectric. The TrFE copolymer introduces defect groups into the PVDF chain and thus lowers the energy for the β

phase and lets it form spontaneously during processing [4]. The dipole moment of PVDF-TrFE is lower than PVDF due to the addition of a third fluorine atom in the monomer. However, taking into account the other advantages, PVDF-TrFE has the edge over PVDF in terms of fabrication and piezoelectric applications [81], [88].

Persano et al. used PVDF-TrFE electrospun fiber sheets that were arranged into aligned 3D architectures that have strong piezoelectric properties resulting from the preferential orientation of the polymer chains during the spinning process [89]. This material displayed excellent piezoelectric properties and can be used in a number of applications including highly sensitive impact detectors, power harvesters for micro-mechanical units and self-balancing robots. Li et al. developed a mold-transfer method to fabricate a dome- and bump-shaped PVDF-TrFE film that was used in flexible tactile sensors [90]. These sensors are sensitive enough to pick up forces as low as 40 mN at the bumps and 25 mN at the domes. These sensors can be used in microcatheters. In 2015, Bhavanasi et al. reported enhanced piezoelectric performance with a bilayer film of poled PVDF-TrFE and graphene oxide (GO), where the bilayer film produced 4 V of voltage and 4.41 $\mu W cm^{-2}$ of power output compared to 1.9 V and 1.77 $\mu W\ cm^{-2}$ of power output by PVDF-TrFE poled film alone [91].

2.3.2.2. Enhanced Piezoelectric Polymers

2.3.2.2.1. Polyamide/Nylon

Polyamides, of which nylon is the most well-known, show significant piezoelectric response. What sets nylon apart from other piezoelectric polymers is that it is an established material in the apparel industry. Nylon has been used to make stockings and other clothing

materials from as early as the 1940's [92]. However, it was not until 1970 that Kawai et al. discovered that polyamides possess piezoelectric properties [93]. The study of piezoelectric properties of polyamides was furthered by Scheinbeim and Newman in the following decade, and this development paved the way for the investigation of odd-numbered nylons [88][94][95]. Polyamides arrange themselves to promote maximum hydrogen bonding between the amide and carbonyl groups of adjacent chains (Figure 7). For even numbered polyamides, the dipole moment arising from the bonded amide groups cancels out, whereas odd-numbered nylons are left with more pronounced piezoelectric properties because the amide groups arrange themselves so that their dipole moment adds up [88].

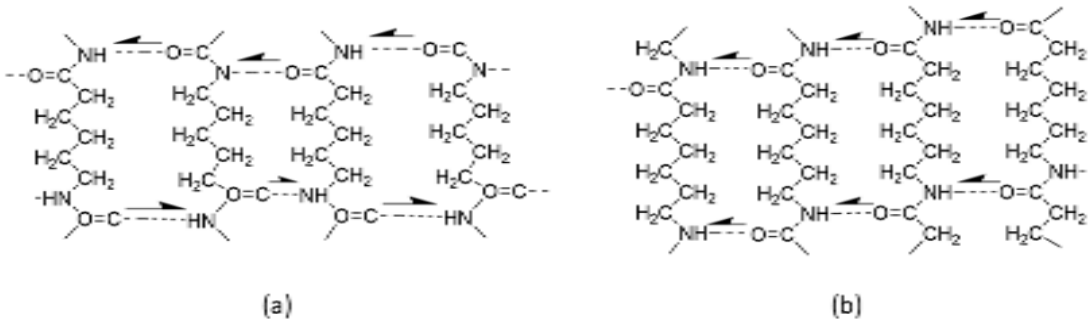

Figure 7: (a) Even-numbered nylon with dipoles cancelling out each other; (b) odd-numbered nylon with dipoles adding up, adapted from [88]

Since nylon is an established material in the apparel industry, these piezoelectric fabrics can be potentially used as a replacement for batteries. Clothes made from piezoelectric polyamide textiles can be used to harvest electric energy from movement, which could then be

used to power small electronic devices. Nylon fabrics can also be used for pressure sensing [92]. For example, Wu et al. fabricated a nylon-11 film by the solution casting method and then unaxially stretched the film, with optimal fabrication conditions leading to a piezoelectric constant of 7.2 pC N^{-1} [96]. Built into a piezoelectric device, it produced an output of 1.5 V and 11 nA.

However, the hindrance in using nylons to harvest energy is that the conventional methods for fabricating nylon fabrics-melt extrusion and melt-spinning do not yield piezoelectric nylon. In order for nylon to be piezoelectric, it must be in its δ-phase, whereas melt spinning and extrusion yield the α-phase [92]. Another setback is that polyamides are hydrophilic; in fact, nylon-5 can adsorb as much as 12% of its weight in water. Water adsorption is detrimental to its piezoelectric and ferroelectric properties, although the negative effects can be reversed by drying [88].

2.3.2.2.2. Polyimides

Polyimides are a family of amorphous piezoelectric polymers known for their excellent thermal, mechanical and dielectric properties [97]. Although PVDF has better piezoelectric properties, polyimides have the edge over PVDF because they can retain their piezoelectric properties at temperatures reaching up to 150^{o}C, whereas PVDF's piezoelectric performance starts to degrade beyond 70-80^{o}C [98], [99]. Polyimides have a high glass transition temperature and are amorphous polymers, which is why their piezoelectric mechanism is markedly different from that of semi-crystalline polymers. Poling is achieved by first exposing the material to a high electric field at a temperature high enough to allow the dipoles to rearrange and align

themselves. The temperature is then lowered below the glass temperature while the electric field is held constant. This process aims to make the amorphous polymer partially retain its polarized state at lower temperatures (e.g. room temperature) [97].

High temperature stability makes polyimides suitable for use in microelectromechanical system (MEMS) devices such as high temperature tactile sensors and pyroelectric sensors, since neither PVDF nor any fluoropolymers are stable under the processing conditions undergone by MEMS devices [97], [98]. Polyimides can also be developed into piezoelectric nanogenerators (PENG) employed in electronic skins or biomedical devices. For example, Yang et al. developed a piezoelectric copolyimide synthesized from pyromellitic dianhydride with p-phenylenediamine and an imidazole ionic liquid which yields a piezoelectric constant of 250 pC N^{-1} at 150 ^{o}C, markedly higher than PVDF and other piezoelectric polymers [100]. 1.17 mW of output power was produced by the PENG developed from this material when exposed to moderate forces of 0.1 N at 3.5 Hz.

2.3.2.2.3. Ferroelectrets

An electret is a material with metastable dipoles, which are either caused by trapped electrostatic charges or temporarily aligned molecular dipoles [101]. Voids within the material are charged by subjecting it to a high voltage, which creates dipoles. As shown in Figure 8, these dipoles are caused by the separation of charges on the internal surfaces of the voids, which impart the material piezoelectric and ferroelectric properties. Electrets are electromechanically similar to common piezoelectric materials. However, unlike true ferroelectric piezoelectric materials, electrets tend to gradually lose polarization at higher temperatures. True piezoelectric

materials, on the other hand, only lose their ferroelectric polarization when heated above the Curie temperature [101].

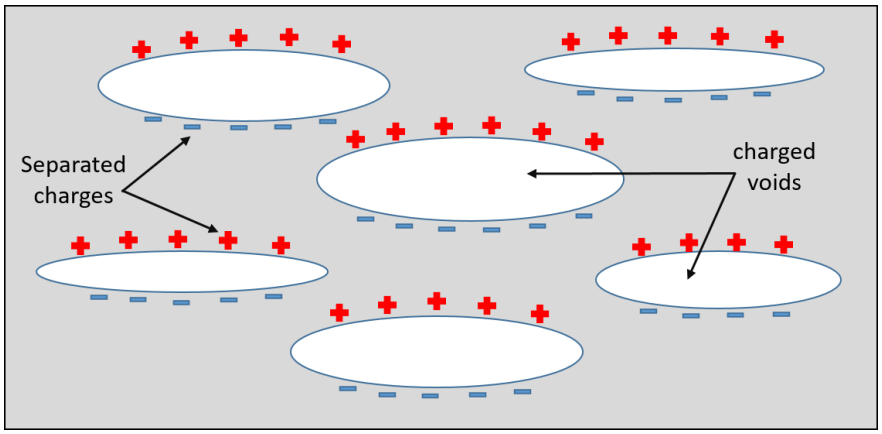

Figure 8: Charge separation in voids within a ferroelectret material

2.3.2.2.3.1. Cellular Polypropylene (PP)

Cellular polypropylene (PP) is amongst the most effective ferroelectrets. Discovered by Kirjavainen, this polymer, when charged, possesses a very high d_{33} value of up to 1200 pC N^{-1} for a single film, but can have any value between 130-2100 pC N^{-1} for multiple layers [102][103][104]. Cellular PP also possesses a low Young's modulus on the order of 1 MPa [105], and has the added benefits of low cost and good fatigue resistance [103]. In addition, it has been shown that the piezoelectric response of cellular PP is directly proportional to the pressure applied to it. These materials have been applied in microphones, transducers and accelerometers. For example, Cao et al. devised a self-powered sensor that measures bending curvature that could potentially be used in baseball or basketball training [106]. In another example, Song et al. used cross-linked

polypropylene (IXPP) ferroelectret films on the inside walls of the cavities in Helmholtz resonators to harvest sound energy, potentially to be applied in roadside applications or high-speed rail transport [107]. It was shown that the d_{33} value of these films was 233 pc N^{-1}, with a power output of 8.66 nW for 4 samples of resonators connected in series.

2.3.2.2.4. Polyorganophosphazenes (POPh)

Polyorganophosphazenes (POPh) are linear organopolymers with piezoelectric properties. The mesophase of POPh is responsible for its piezoelectric characteristics. Fluorination of POPh enhances its piezoelectric properties, since electronegative fluorine atoms induces dipoles which can align with the application of mechanical force. POPhs are categorized as electrets because they exhibit piezoelectric behavior even before poling [108]. Partial conjugation of the alternating single and double bonds in the central P-N-P-N backbone causes it to be positively charged, while the fluorine atoms around it create a negative charge. These positive chains, uniaxially aligned and surrounded by a negative fluorine "cloud," cause the material to have electrical properties prior to poling.

POPh thin films can be fabricated by solvent casting on a glass support in an argon atmosphere then drying under vacuum. Piezoelectricity in POPh can be enhanced by either annealing (to coax the chains to align better) or by doping with other ions. It has been demonstrated that adding $LiSO_3CF_3$ salt to the structure can improve piezoelectric properties significantly [109]. In fact, POPh doped with 10% salt composition has demonstrated a d_{31} value of 150 pC N^{-1}, which is significantly higher than that of PVDF electrets [110]. Also, it has been shown that POPh has high piezoelectric moduli at lower frequencies (< 5 Hz) [109].

2.3.2.3. Shortcomings of Piezoelectric Polymers

Piezoelectric polymers lack mechanical strength, and thus are not ideal under circumstances where they will be subjected to heavy loads. Though they are flexible, lightweight and have some shock-absorbing capacity, piezoelectric polymers tend to deform. Piezoelectric polymers also tend to have a faster decaying piezoelectric response in comparison to piezoelectric ceramics due to the absence of stiffer grain boundaries and subsequent relaxation into lower energy states. Furthermore, they cannot withstand high temperatures. The biggest shortcoming for this class of piezoelectric materials, however, is that they do not, in general, have very high piezoelectric coefficients. Thus, piezoelectric polymers are inefficient energy harvesters.

2.3.2.4. Comparison of Piezoelectric Polymers

Most piezoelectric polymers have low piezoelectric constants, as seen in

Table *2*. The exception presented here is cellular polypropylene, which can also be classified as a ferroelectret, explaining its exceptional properties. It is also worth noting that all the piezoelectric polymers have lower operating temperature ranges due to their low Curie temperatures and lower electromechanical coupling factors than ceramic piezoelectric materials. However, piezoelectric polymers are highly flexible in comparison to piezoelectric ceramics.

Table 2: Polymer Piezoelectric Materials and their Properties

Material	Polymer Type	Piezoelectric Constant, d_{33} (pC N^{-1})	Voltage Constant, g_{33} (V*m N^{-1})	Electromechanical Coupling Factor	Young's Modulus (GPa)	Curie Temperature (°C)
PVDF	Semi-crystalline	-24 to -34[82]	-0.33 [111]	0.20 [112]	4.18 [113]	75-80 [79]
PVDF-TrFE	Semi-crystalline	-25 to -40 [114]	-0.542 [115]	~0.29 [112]	~1.5 [116]	~110 [79]
Cellular Polypropylene	Semi-crystalline	130 to 2100 [104]	30 [79]	--	0.002 [79]	--
Nylon-11	Semi-crystalline	7.2 [96]	--	--	--	--
Polyimide[a]	Amorphous	-2.7 [117]	0.087 [117]	--	--	225 [117]
Polyphosphazenes	Amorphous/semi-crystalline	150(d_{31}) [110]	--	--	0.108[118]	--

[a] values for (β-CN)-APB/ODPA polyimide

2.3.3. Composite Piezoelectric Materials

2.3.3.1. Governing Mechanism of Composite Piezoelectric Materials

Piezoelectric composite materials are a combination of two piezoelectric materials, the arrangement of which is aimed to enhance the piezoelectric properties of the resulting material. The properties of such a material can be further tailored by changing the proportion of the materials, their connectivity and structure, etc. For example, piezoelectric polymers have low piezoelectric constants, but they match well acoustically with living tissue and water, which are two common materials used for harvesting piezoelectric energy. On the other hand, ceramic piezoelectric materials like PZT have a high piezoelectric constant, but are not a good acoustic match to the above-mentioned media. A composite comprised of polymer and ceramic piezoelectric components can result in a material with a good combination of piezoelectric performance and acoustic match that can be fine-tuned to fit the needs of the targeted application [119].

2.3.3.2. Classification According to Connectivity Patterns

Piezoelectric composite materials can be classified according to their connectivity patterns, a system developed by Skinner and Newnham [120]. If diphasic composites are considered, they can be divided into 10 separate groups, namely: (0-0), (0-1), (0-2), (0-3), (1-1), (1-2), (1-3), (2-2), (2-3), and (3-3). Pilgrim et al. suggested 6 additional connectivity patterns: (1-0), (2-0), (3-0), (2-1), (3-1), (3-2) [121]. These notations are in the “a-b” format, where “a” represents the connectivity of the electromechanically active phase and “b” represents the connectivity of the inactive, polymer phase of the composite. The number indicates the extent

of connectivity of that phase, for example, “3” would indicate that the phase is self-connected in all 3 axes and “0” would mean that it is not connected on any of them [119]. The connectivity patterns have been depicted in Figure 9 below.

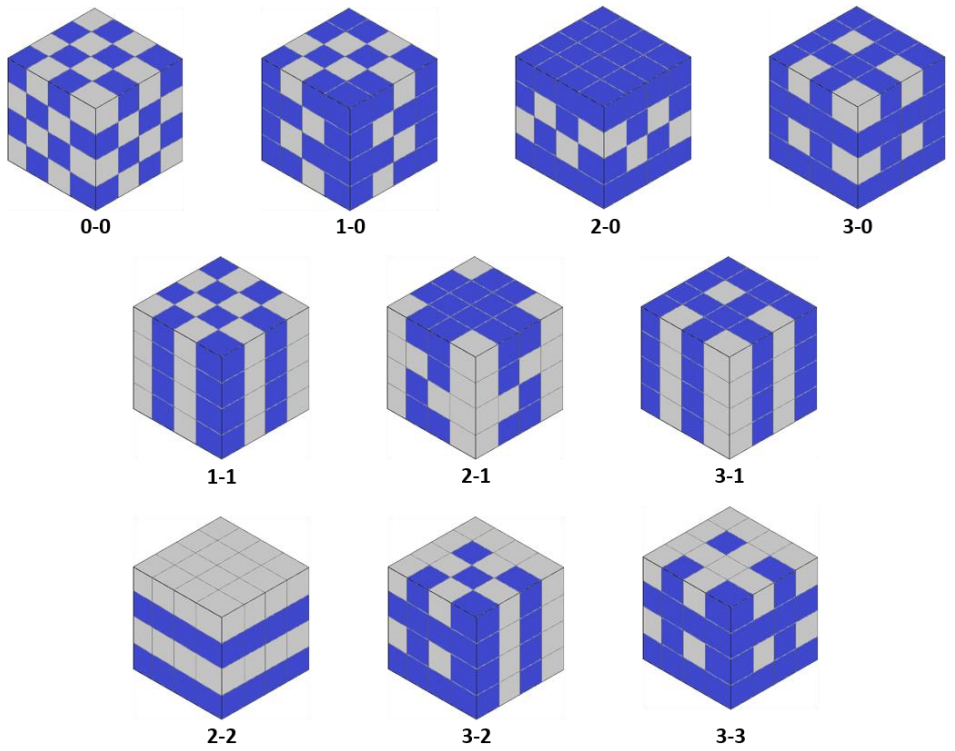

Figure 9: Connectivity patterns of piezoelectric composites

Among these connectivity patterns, the (0-3) pattern offers the advantage of being easy to fabricate and scale up. A (0-3) composite is usually comprised of a three-dimensionally connected polymer matrix with zero-dimensional ceramic particles dispersed within [122]. Molding this composite into various shapes is also relatively easy, and mass production is very much viable with this connectivity pattern. For example, Sappati et al. fabricated a (0-3)

composite of PZT dispersed in PDMS, where it was shown that at 28 v% PZT loading, the d_{33} value of the composite was 78.33 pC/N and the Young's modulus was 10 MPa, making it a pliable enough material to successfully act as a tactile sensor [123]. It produced an open circuit voltage of 4.7 V under pressure from a finger. In another work, Lv et al. developed a (0-3) type ceramic composites where sub-micron particles of Sb-doped ZnO were dispersed in KNN, which achieved a very high piezoelectric constant (~500 pC/N) and high Curie temperature (>250 ^{o}C) [124]. Composite materials evidently hold potential in the development of piezoelectric technology. The following section delves into a few of the more widely explored piezo-composites being studied today.

2.3.3.3. Synthesized Combinations

2.3.3.3.1. PVDF-PZT

PVDF-PZT is one of the most commonly worked with polymer-ceramic piezoelectric composites. Kitayama and Sugawara were the first to report properties of polymer-ceramic piezoelectric composites, starting with the (0-3) type [125]. On its own, PVDF has a relatively low piezoelectric constant and low stiffness, and PZT is too stiff to be used in media like water or blood. A composite of PVDF-PZT overcomes these disadvantages by adapting average properties between PVDF and PZT. This composite has a stiffness coefficient that is much less than that of PZT, while at the same time having a piezoelectric constant that is only slightly smaller than that of PZT [119].

Wankhade et al. fabricated a cheap and durable PVDF-PZT composite nano-hybrid material that was built into a device that yielded an output of 55 V and 36 μW cm^{-2} power density

at optimum performance, which occurs at 30 weight % of PZT filler [126]. They used a solution method to prepare the nano-hybrid films at filler weight percentages of 0, 10, 20, 30 and 40%. A rectangular specimen of the film was cut, coated with polydimethylsiloxane (PDMS), and then cured to give it flexibility and protection. Human movements such as finger tapping, feet tapping and bending were used to test the output.

In another work, a baklava-structured PVDF-PZT piezocomposite sensor was built into a table tennis racket for real-time monitoring of the impact between ball and racket [127]. This can serve the purpose of providing important data to aid in individual training. The composite was manufactured by a 2-step method involving phase separation by a nonsolvent method, followed by hot-pressing. The resulting material, though not doped as significantly, gave a maximum open circuit voltage of 2.51 V.

2.3.3.3.2. $BaTi0_3$/PVDF

Mechanical endurance is a desired quality in heavy load piezoelectric energy harvesting applications, such as piezoelectric energy harvesting from walking or running motion. Barium titanate nanoparticles can be dispersed in a PVDF-TrFE matrix to produce a lead-free piezocomposite, which is then electrospun into nanofibers that are both durable and flexible. This nanofiber is then embedded in PDMS to further distribute pressure and protect the material from damage, as well providing protection from moisture. The composite has excellent piezoelectric performance because of the use of self-poled, highly crystalline PVDF-TrFE and barium titanate nanoparticles, both of which possess positive piezoelectricity. It was found that when placed inside a shoe and loaded with 15 wt% barium titanate, this piezocomposite can

generate a voltage output of 25 V with walking motion at a frequency of 0.6 Hz. At this rate, it can be used to charge a 4.7 μF capacitor after about 72 steps, which can then be used to power a strain sensor. Furthermore, it has been shown to withstand loads close to 600 N [128]. In another work, barium titanate was surface-modified with polydopamine (PDA), then blended with PVDF to form a PDA@BTO/PVDF composite, where the role of PDA is to promote homogeneous dispersion of barium titanate in PVDF and to reduce interfacial defects and cracks [129]. The optimal mixing ratio of this composite was used to produce a sensor with a piezoresponse time of 61 ms and an output voltage of 9.3 V.

2.3.3.3.3. PMN-PT with Polyimide and PDMS

Nanoscale energy harvesting via piezoelectric energy harvesters (PEH) has the potential for powering small electronic devices. Piezoelectric nanowires are a particularly attractive option for energy harvesting from mechanical motion. The man-made crystal, lead magnesium niobate-lead titanate (1-*x*)$Pb(Mg_{1/3}Nb_{2/3})O_3$-*x*$PbTiO_3$, or PMN-PT for short, has a very high piezoelectric constant (d_{33} equal to ~2500 pC N^{-1}) and high electromechanical coupling factor (k_{33} equal to 0.94) [130], [131]. A PMN-PT crystal can produce a piezoelectric coefficient that is 30 orders greater than $BaTiO_3$ and 4 orders greater than bulk PZT [132]. However, the challenge in fabricating PMN-PT devices, as well as transferring the material onto flexible substrates without damage, limits its application in PEHs. PMN-PT are relaxor ferroelectric materials that have a relatively low Curie temperature range, approximately 130-170^oC [37]. Xu et al. used low temperature hydrothermal fabrication to produce PMN-PT nanowires, which were then incorporated into a polymeric matrix to make a nanogenerator [132]. In order to further improve the performance, they used a top-down fabrication method to create a PMN-PT single crystal

nanobelt that acts as a nanogenerator with an output voltage of 1.2 V [133]. Moorthy et al. used a similar method to fabricate PMN-PT nanowire PEH [134]. They then dispersed the nanowires in a polyimide substrate (Figure 10) with Au electrodes and connected the nanowire with the electrodes using focused ion beam (FIB) platinum deposition. This was then poled to build a nanogenerator device with an output voltage of 4 V and a maximum current of 400 nA when subjected to bending cycles.

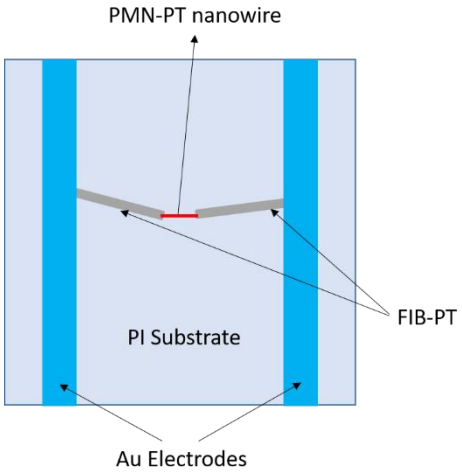

Figure 10: A composite of PMN-PT nanowire on poluimide substrate fabricated by the hydrothermal method, adapted from [134]

However, polymer-ceramic piezocomposites have reduced performance due to low stress transfer from the polymer matrix to the ceramic active component, especially when the active component is inter-connected in fewer dimensions. Zhang et al. have devised a piezocomposite comprised of a 3D "skeleton" of Samarium-doped $Pb(Mg_{1/3}Nb_{2/3})O_3$-$PbTiO_3$ (Sm-PMN–PT)

developed by a biofibril template method and a flexible PDMS foam that fills the pores inside of that structure [135]. Particles of the Sm-PMN-PT powder were mixed into a cellulose powder solution, after which the slurry was cast, dried, calcined and sintered to form the interconnected piezoelectric skeleton. PDMS is then infiltrated into the skeleton structure via the help of vacuum suction, after which it is cured and later poled. The formed piezocomposite has improved mechanical strength, resulting from improved stress transfer due to the interconnected piezoceramic skeleton. Piezoelectric properties were also enhanced: the composite has a short circuit current density of 850 nA cm^{-2} and an open circuit voltage of 60 V. The maximum instantaneous power density yielded was approximately 11.5 μW cm^{-2}, which is reported to be approximately 16 times higher than the power density yielded by polymer composites made from nano-particles.

2.3.3.3.4. ZnO-PVDF

Self-powered wearable electronic devices are being researched intensely because of their numerous applications, which include communication devices and health sensors. Piezoelectric nanogenerators (PENGs) have been shown to be efficient in converting mechanical strain from human motion or ambient vibrations into electrical energy and therefore are being studied for use in powering wearable electronics. Jin et al. demonstrated in one such work where the PENG device used a thin-film composite consisting of doped ZnO nanostructures and PVDF-TrFE [136]. The ZnO nanoparticles were doped with Co, Na, Ag and Li, of which Li-doped ZnO-PVDF showed the highest peak-to-peak voltage of 3.43 V, about 9 times that if pure ZnO was used instead. It was shown that finger-tapping at approximately 2 Hz resulted in power output sufficient enough to charge a capacitor with a power density of 0.45 W cm^{-3} and light an ultraviolet LED. In another

work, Li et al. showed that a PENG device fabricated from PVDF and ZnO nanoparticles and nanorods had a large open circuit voltage of ~85 V and a short circuit current of ~2.2 μA and could light up commercial LEDs and charge capacitors upto 3 V in 25 seconds [137]. The ZnO nanoparticles acted as nucleating sites for the β phase of PVDF and the ZnO nanorods deformed to produce extra piezoelectric charges.

2.3.3.3.5. KNN-BNZ-AS-Fe in PDMS

Another example of a piezoelectric nanogenerator (PENG) developed from composites is the KNN-BNZ-AS-Fe ($0.91K_{0.48}Na_{0.52}NbO_3$–$0.04Bi_{0.5}Na_{0.5}ZrO_3$–$0.05AgSbO_3$–0.2% Fe_2O_3) particles made using a solid-state reaction and embedded in a PDMS matrix [138]. This composite showed a very high piezoelectric coefficient of approximately 500 pC N^{-1}, with an open-circuit voltage of 52 V and a short-circuit current of 4.8 μA under 25 N of vertical force at 2 Hz frequency, which was sufficient enough to light 10 commercial green LEDs. A counter that was incorporated with this PENG allowed the device to accurately register the number of times it was touched by fingers, and it was also shown to be able to function as a pressure sensor in a self-powered smart collision alarm system. This PENG was shown to be able to operate both as an efficient energy harvester, as well as a self-powered sensor, thus making very promising for integration in artificial intelligence technology.

2.3.3.3.6. Sm-PMN-PT in PVDF

Changing the design of a composite material can also affect its piezoelectric performance. For example, Gu et al. added 3D intercalation electrodes in a Sm-PMN-PT/PVDF composite such that the amount of interfacial boundaries and hence the surface for polarization increased,

leading to higher current output of up to 320 μA [139]. This material was shown to be able to light up 100 commercial red LEDs with only a 1.2 cm^2 area of the energy harvester at work and also be able to charge a 1 μF capacitor up to 8 V in as little as 21 cycles. It has been initially tested and shown to be successful in harvesting energy from human gait.

2.4. Comparison between Classes of Piezoelectric Materials

The three different classes of piezoelectric materials presented in this paper each have their strengths and weaknesses, which should be factored in when selecting a material for a given application. Table 3 presents a qualitative comparison of the three classes of piezoelectric materials. It is worth noting that this comparison is based off of values from materials that are a typical representation of each of the classes (i.e. PVDF for piezoelectric polymers), and not based on values from outlier or exceptional materials (e.g. ferroelectrets). It can be inferred that composites piezoelectric materials attempt to bring together the best properties of both piezoelectric polymers and ceramics.

Table 3: Qualitative comparison of the properties of the different classes of piezoelectric materials

Property or Metric	Ceramics	Polymers	Composites
Piezoelectric Constant	High	Low	High
Voltage Constant	Low	High	High
Flexibility	Low	High	Average

Electromechanical Coupling Factor	Average	Low	High
Curie Temperature	High	Low	Subjective[a]
Mechanical Quality Factor	Med	Low	High
Acoustic Impedance	High	Low	High
Chemical Reactivity	Low	Subjective[b]	Subjective[b]
Ease of Manufacturing	High	High	Low
Cost	High	Low	Subjective[a]
Density	High	Low	Average

[a] *Depends on constituents and the manufacturing process*

[b] *Depends on chemical composition and the presence of reactive functional groups*

It is evident that certain materials will be better for certain applications, taking into account the strengths and weaknesses of each class of material. For example, as shown in Figure 11, ceramic piezoelectric materials are generally the choice in MEMS devices and transducers such as the sonar, technology where a good piezoelectric response is required but not flexibility of the material itself. Piezoelectric polymers, on the other hand, are best-suited for flexible applications such as wearable electronic fabrics that sense or harvest energy and for biomedical applications such as self-powered implants or bone tissue scaffolding, due to their compatibility with the human body. Composite materials are the most versatile class of piezoelectric materials,

with applications including, but not limited to, tactile sensors and energy harvesting from human gait.

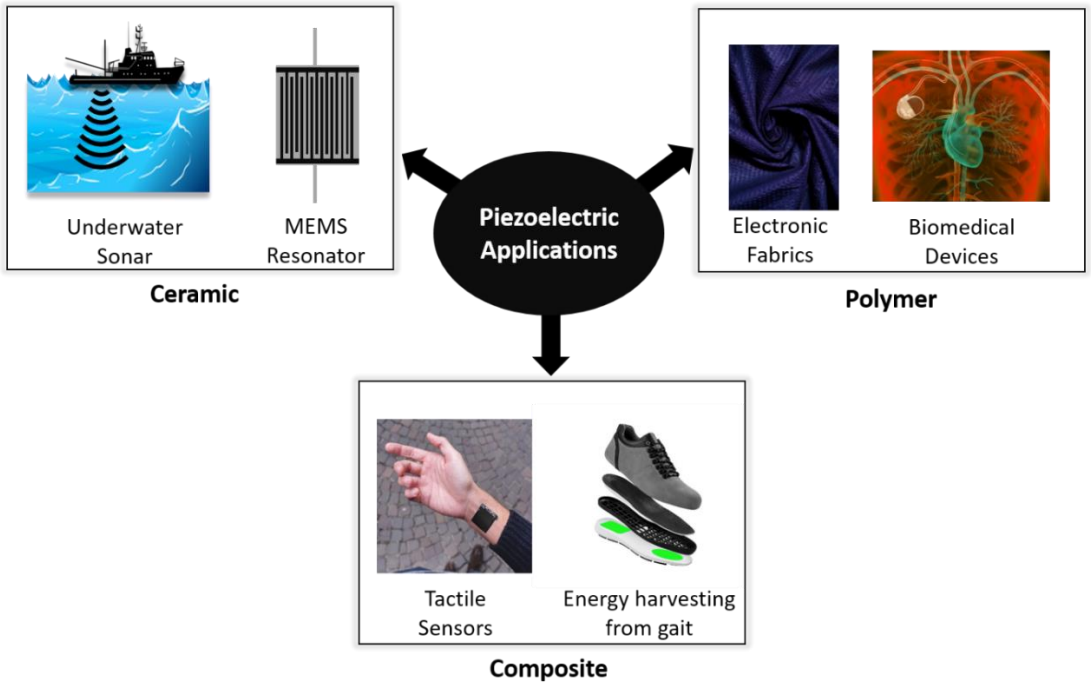

Figure 11: Applications of the different classes of piezoelectric materials

2.5. Conclusions and Suggested Future Work

Piezoelectricity is a phenomenon that has proven useful in applications such as sensing and energy harvesting. This review compared existing piezoelectric materials in terms of their properties, strengths/weaknesses, applications and state-of-the-art research being conducted. The mechanisms of piezoelectricity from a materials science viewpoint have been briefly discussed here. Piezoelectric materials have been subdivided into three broad classes (ceramics, polymers, composites), and their properties have been discussed with a focus on the linear

response in the d_{33} mode. Comparisons have been made between the material classes, as well as between the materials within those classes. Though ceramic piezoelectric materials traditionally possess better piezoelectric coefficients and electromechanical coupling factors, piezoelectric polymers are more flexible and lightweight, and can offer a greater variety of uses such as wearable electronics and biomedical applications. It has been shown that overall, composite piezoelectric materials seem to have the edge in terms of a more useful balance of properties. Newer piezoelectric technology, such as nanogenerators and ferroelectrets, have highly enhanced piezoelectric properties and are currently being explored.

Though piezoelectric materials have come a long way since their initial discovery, there is still ample room for improvement in material properties to enable novel applications. A major setback for piezoelectric materials is that they remain inefficient energy converters. Also, the resonant frequencies of stiffer piezoelectric materials are far too high to be matched to ambient vibrations. Thus, ambient piezoelectric energy harvesting still requires further research to lower the materials' resonant frequency. In addition, increasing the operating temperature in general tends to lower their piezoelectric coefficient [140], so work must be done to prevent performance degradation at elevated temperatures. One way to improve piezoelectric performance would be to fabricate new composite materials that have a better blend of piezoelectric properties. The process could be facilitated by devising a database that holds materials properties of various existing composites, thereby allowing models to design and develop novel composites with the desired properties. Changes in the architecture of a material may be another way to enhance piezoelectric performance. It was previously mentioned that novel electroding methods can increase interfacial area and thus increase charge production.

Enhanced piezoelectric properties could lead to novel applications such as piezoelectric energy harvesters to power sensors in remote locations, for example observation equipment deployed in the ocean that harvests energy from wave motion to power itself. In the biomedical field, piezoelectric energy harvesters based on biocompatible nanocomposites could be used to power cardiac pacemakers and eliminate the need of replacing batteries, thus reducing the risk of complications for heart patients. It can thus be concluded that piezoelectric materials could become more prevalent in sensing and energy-harvesting applications if their material properties were enhanced using composite optimization.

3. Design Exploration of Piezoelectric Energy Harvesters For Buoys

Oceans cover approximately 71% of the earth's surface. Ocean waves, a relatively unexplored resource, are not only one of the most abundant sources of renewable energy, but also one of the most energy-dense. It is, therefore, important to explore ways to effectively harness this renewable resource, especially for smaller off-shore unmanned vessels that are a challenge to recharge. Ocean observation buoys, for example, can be powered by wave energy from the ocean, provided the means of energy harvesting is relatively compact and affordable. In this work, we investigate the feasibility of attaching a flexible piezoelectric energy harvesting device to an ocean observation buoy to provide it power. We look at two separate models of piezoelectric energy harvesters made from flexible polymers: direct and indirect. In the direct wave piezoelectric energy harvester, the piezoelectric elements are directly impacted by the waves to produces electric energy. The indirect wave piezoelectric energy harvester, on the other hand, is not in direct contact with the waves and can oscillate at a higher frequency than the waves using a frequency conversion mechanism. Both models are compared in terms of voltage and power outputs, cost and volume. It is found that the indirect wave piezoelectric energy harvester is the better performing model of these two. Although the cost estimated for the indirect model ($18,000+ for 10W power supply) still exceeds that of existing technology (e.g. solar power), it holds the potential for improvement with better-performing materials and better frequency ramp-up techniques.

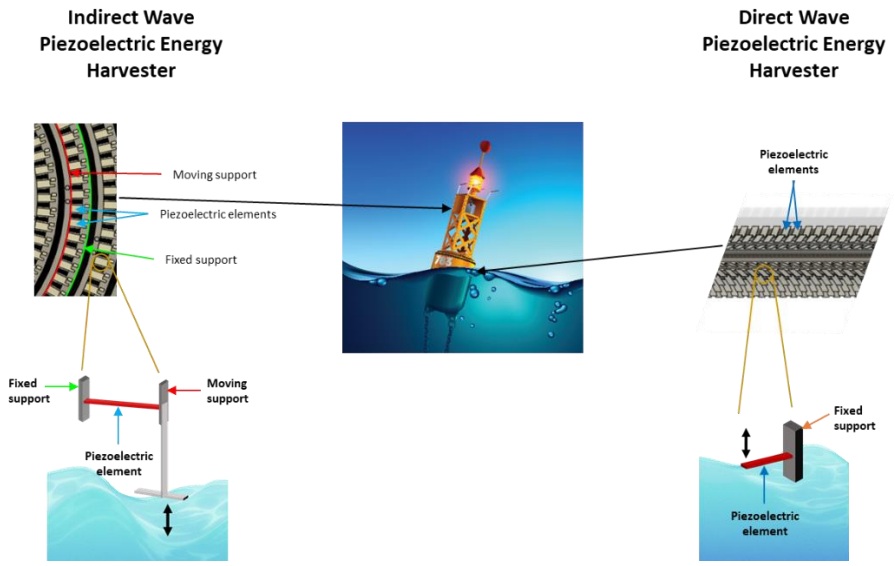

Figure 12: The two piezoelectric energy harvester models presented in this work include the indirect wave piezoelectric energy harvester and the direct wave piezoelectric energy harvester. The indirect wave harvester is placed within the buoy and above the water's surface, with a frequency-ramp up system conveying the motion of the waves to the piezoelectric element through the moving support; the direct wave harvester is placed at the water level and in touch with the waves

3.1. Nomenclature

HCD Hydrokinetic Conversion Device

WEC Wave Energy Converter

OTD Overtopping Device

OWC Oscillating Water Column

WAB Wave Activated Body

VIV Vortex Induced Vibrations

PVDF Polyvinylidene Difluoride

PEH Piezoelectric Energy Harvester

3.2. Introduction

Diminishing fossil fuel supplies, as well as the effects of global warming, have led to a heightened demand for renewable energy sources. Of the renewable sources available, hydropower has the highest energy density (~2-3 kW/m^2) [141]–[143]. The most readily available form of energy in the ocean, wave energy, is thus more energy dense than either solar or wind energy, but unfortunately remains largely unharnessed to-date. Energy harvested from the ocean can conveniently be used to supply power to floating vessels such as ocean observation buoys. The market for observation buoys is growing due to increased demand for tsunami-warning systems, precise prediction of weather patterns and extensive scientific studies in the ocean [144], [145]. The U.S. National Data Buoy Center has deployed a fleet of more than 1300 buoy stations to collect and transmit ocean data [146]. These buoys, which are deployed far from land to collect ocean and meteorological data, require an energy source than is sustainable, since recharging batteries mid-ocean is non-ideal. Some buoys employ solar cells or wind turbines to collect energy. However, solar cells are expensive, unreliable and subject to high maintenance due to deterioration of the cell's surface in a marine environment, and the turbines needed for harvesting wind energy are both cumbersome and detrimental to the environment [142], [147], [148].

Hydrokinetic conversion devices (HCD) can be considered a mature technology [149]. The particular type of HCD used in harvesting energy from ocean waves is called wave energy

converters, or WECs [150][151]. They can be grouped into three major categories: overtopping devices (OTD), oscillating water columns (OWC) and wave activated bodies (WAB). Several of these hydrokinetic conversion devices have been established on a pilot scale or commercial level. For example, the Mutriku Plant off the coast of Spain is a type of OWC which has a collection of chambers, each equipped with its own Wells turbine and produces a total power output of 300 kW, enough to supply about 250 households [152]. CETO, an example of a WAB, is a submerged heaving buoy with vertical motion, of which three prototypes have been established in Australia [151]. The CETO buoy maintains positive buoyancy and the heaving motion of the waves causes it to move up and down, thus compressing an attached hydraulic pump and creating high pressure on the fluid inside. This fluid then operates a hydraulic motor, which powers an electric generator. These devices, which use mechanical to electrical energy conversion, are very promising, but have the disadvantages of moving or hinged parts that are set in constant motion by the impact of waves. This causes friction between parts, which would require constant maintenance in order to prolong life. Another disadvantage for these wave energy converters, in particular overtopping devices and some of the oscillating wave column harvesters, is that they are usually very large and thus cannot be attached to smaller buoys [153].

On the other hand, piezoelectric energy harvesting from ocean waves is not an established technology, although it has been employed previously to harvest energy from ambient vibrations in industries, roadsides and from human motion [154]–[163]. Some work has been done to explore its potential in harvesting energy from ocean waves as well. One way to harness ocean energy is to absorb the vibrations present in a water current. Of the types of vibration that exist in water flow, vortex induced vibrations (VIV) are primarily worked with in

piezoelectric harvesting. A bluff body placed in a flowing water will induce vortices whose frequency and size are determined by the configuration of the body [164]. If a piezoelectric membrane is attached as a trail to the bluff body, it will oscillate with the vortices to generate a voltage. For example, Taylor et al. experimented with such a device which imitates an eel [165]. A piezoelectric polymer strip was attached to the bluff body, and the resulting vortices caused a pressure gradient which made the strip wave in the motion of an eel. To make sure that maximum conversion efficiency is reached, the strip was fabricated so that that its oscillating frequency matched the frequency of the vortices, and as a result, a peak voltage of about 3 V was reached. A similar design was presented by Pobering and Schwesinger, where a flag consisting of two layers of polyvinylidene difluoride (PVDF) was attached to a bar that caused the separation of the water flow and hence the vortices. This then caused the flag to wave and generate electricity. Another concept proposed for energy harvesting from wave motion is the wave carpet. This is a device that made use of a flexible membrane, PVDF due to its flexibility, in deep sea. However, the size of the carpet was predicted to be a few square kilometers at least, and a significant number of piezoelectric elements would have to be installed into the system in order to make power production substantial [167].

The main problem faced by piezoelectric wave energy conversion is that the frequencies of waves and the natural frequency of common piezoelectric materials differ greatly, which leads to inefficient energy conversion. Frequencies of waves are in the range of 10^{-1} Hz, whereas the natural vibrational frequencies of most piezoelectric materials are around ten thousand times more [168]. This work on piezoelectric wave energy harvesters seeks to establish a way to harvest energy from ocean waves efficiently. To achieve that end, two separate models are proposed

here that study the effect of certain parameters of a piezoelectric energy harvester being hit by water waves. The first model, the direct wave piezoelectric energy harvester model, attempts to measure the power and voltage outputs of a flexible piezoelectric energy harvesting element coming directly in contact with ocean waves, as shown in Figure 13. The second model, the indirect wave piezoelectric energy harvester model, replicates the conditions of a piezoelectric element placed above the water and not in direct contact with the waves, but with a setup that not only conveys the motion of the waves to the elements, but also ramps up the frequency such that power output is maximized. Both models are also tested out by experimentation in the lab in order to prove that they are feasible and that the results are within the ranges predicted by the models. Lastly, the average power outputs for the models are calculated, which lead to an estimation of the cost and volume of the devices required to power an ocean observation buoy.

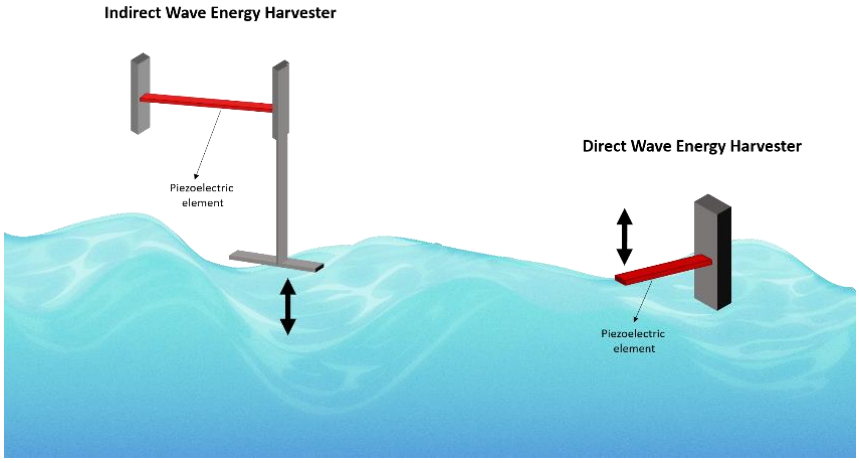

Figure 13: Representation of the two models explored in this paper: the direct wave energy harvester (right) which is situated at the water's surface and is in contact with the waves, and the indirect wave energy harvester (left) which is positioned above the water and has a mechanism to convey the motion of the waves to the piezoelectric elements.

3.3. Methods

3.3.1. Direct Wave Piezoelectric Energy Harvester Model

The direct wave piezoelectric energy harvester model is comprised of a piezoelectric element that protrudes from the lower surface of the buoy and is immersed in water, as shown in Figure 13. When ocean waves hit the piezoelectric element, the mechanical energy deforms it and is converted to electrical energy. The piezoelectric element in this model is in the form of a flat strip of flexible piezoelectric material, polyvinylidene difluoride (PVDF), with one of its ends tethered to the lower surface of the buoy such that it remains submerged in seawater and is always in direct contact with waves. When waves cause the piezoelectric strips to deform, separation of charges occur, which then travel to an insulated circuit connected to a rechargeable battery housed within the buoy.

The direct wave piezoelectric energy harvester is set up as a simplified, 2-dimensional, time-dependent model using COMSOL Multiphysics®. For modeling purposes, a single piezoelectric element is immersed in water at 293.15 K and atmospheric pressure that is enclosed within a rigid tank. The piezoelectric element is hit by periodic waves entering the water tank through an inlet on its left-hand side that causes the piezoelectric element to bend. This in turn will produce an electric potential across the element, which will then discharge through an external electric circuit. As shown in Figure 14, the piezoelectric energy harvester (PEH) element is primarily a flexible piezoelectric strip made from polyvinylidene difluoride (PVDF) that is sandwiched between thin layers of silver ink depositions that function as the electrodes. Each element has dimensions of 45 mm by 10 mm, with a thickness of 0.26 mm. It is attached at one

of its ends to a concrete support protruding down into the wave tank to tether the piezoelectric strip in place and establish electrical connection (Figure 15). The concrete support is assumed to be a solid wall with non-slip boundaries. The water is contained within a tank, whose dimensions measure 300 mm by 100 mm. The dimensions for the water tank used in the model are much smaller than what is used in the corresponding experiment in order to simplify fluid dynamics calculations involved in the model. The left-hand border of the water tank is defined to be the inlet and the right-hand side the outlet. The water medium is assumed to maintain steady temperature and pressure.

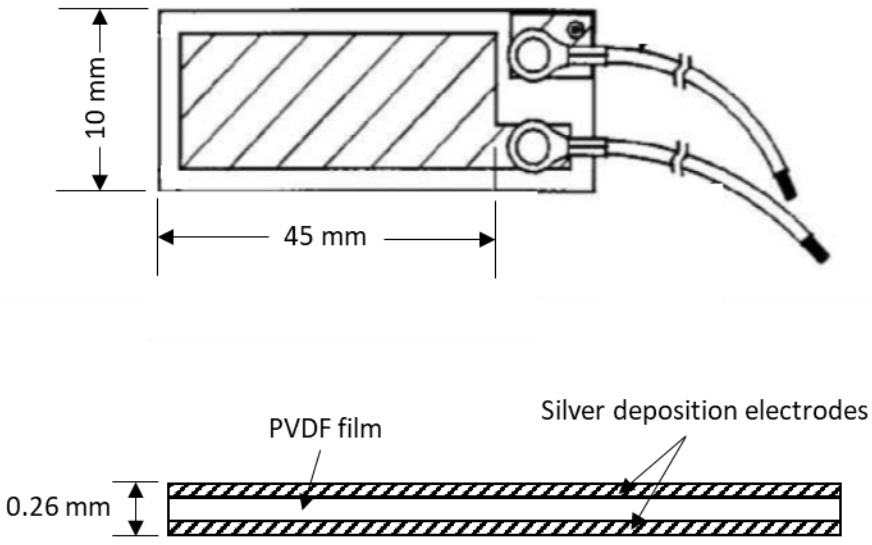

Figure 14: The flexible piezoelectric energy harvester element is made of PVDF film and is flanked by two layers of silver deposition that act as the electrodes.

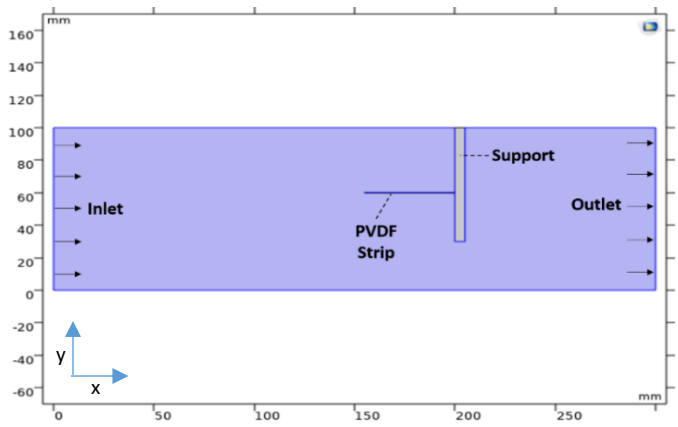

Figure 15: Set-up of direct wave piezoelectric energy harvester model developed in COMSOL Multiphysics®. Water flows into the left boundary (using a simulated wave function), and flows past a flexible PVDF piezoelectric strip attached to a rigid support, causing the strip to deform and generate power. The simulation runs until one simulated wave has passed the strip.

In-built physics included in COMSOL Multiphysics® are used to define this model. Physics interactions used in the model include the Fluid-structure Interaction (which links the effects of the laminar flow physics to solid mechanics) and the Piezoelectric Effect (which links solid mechanics to electrostatics). The wavefront begins to flow through the wave tank at t=0 seconds, and a single wave is simulated to minimize computational time. The medium (pure water) is assumed to be incompressible in this model. Water enters through the inlet (defined as the left-most boundary of the wave tank) at a set velocity, which is defined by the equation

$$V = 0.35 * m * tri(t) \quad (3\text{-}1)$$

where m is a variable by which the base velocity, 0.35 m/s, is multiplied, t is the time in seconds and tri stands for a triangular function. The base velocity was calculated by estimating the velocity of the wave-front if a reservoir of water at a fixed height above the wave tank floor (and

hence, a fixed volume) were to be released through the inlet of the wave tank. The velocity of the waves are defined to have an x-component only. Velocity in the y-direction is neglected in the model in order to simplify terms. Also, laminar flow is assumed for the water wave flowing in, and turbulence has been neglected here, as well as any backflow of the wave medium. The boundary condition at the outlet is defined in terms of pressure, where the static pressure p_0 is set at 0 Pa (i.e. total pressure of 1 atmosphere). The equations governing the laminar flow physics model are given below:

$$\rho \frac{\partial u}{\partial t} + \rho(u.\nabla)u = \nabla.[-pI + K] + F \tag{3-2}$$

$$\rho \nabla . u = 0 \tag{3-3}$$

where equation (3-2) represents the Navier-Stokes equation, where ρ is the density of water, u is the velocity, t is the time, p is the fluid pressure, K is the term accounting for viscous forces, and F is the term accounting for external forces applied to the fluid. (3-3) is the continuity equation for incompressible fluids.

The mechanical deformation is defined with a plain-strain model because the piezoelectric element can be considered significantly thick in the out-of-plain direction (10 mm). It is specified to be a linear elastic material, whereas the rest of the objects/boundaries (e.g. tank walls, support) are defined as fixed and rigid. The linear elastic properties of the piezoelectric strip are considered to be isotropic. The governing equations for the solid mechanics of this model are:

$$\rho \frac{\partial^2 u}{\partial t^2} = \nabla . \sigma + F_v \tag{3-4}$$

where ρ is the solid density, u is the displacement vector, σ is the stress tensor and F_v is the force per unit volume.

Electrostatics is incorporated into the model to replicate the behavior of the charges on the piezoelectric strip separating and causing a voltage to form across the electrodes. The top and bottom layers of the piezoelectric PVDF strip have silver ink electrodes that act as the terminals to draw off the collected charges. An external electrical circuit is added to the terminals of the electrodes to be able to measure the voltage and power outputs of the piezoelectric strip. The nodes are defined for the simple external circuit, with an external resistor of 10^8 ohms being placed in series to match the internal impedance of the piezoelectric component.

A physics-controlled mesh is used for this model in order to accommodate for the interfaces (i.e. the surface of the piezoelectric element). The number of mesh elements used in the simulations was approximately 73,000. The model is solved in a time-dependent study (in increments of 0.05 seconds) for the span of approximately 0 to 0.5 seconds, which is the time it takes for one wave to pass through the wave tank.

A number of assumptions are made for this model in order to reduce its complexity:

1. The model is simulated in 2D instead of 3D to reduce convergence time.

2. Laminar flow is assumed and turbulence neglected in order to simplify the model.

3. Waves do not reflect back (i.e. backflow is suppressed) in order to eliminate the effect of waves interacting with each other.

4. The walls of the tank are rigid, as is the support (no-slip boundary conditions assumed).

5. The piezoelectric element is modeled as an isotropic, linear elastic material.

6. Strain in the out-of-plane direction of the 2D model is considered to be zero.

7. Temperature and pressure of the elements within the wave tank are assumed to remain steady and no heat is generated due to friction or external work.

3.3.1.1. Experimental Setup of Direct Wave Piezoelectric Energy Harvester Model

An experimental demonstration of the wave tank experiment was performed in order to validate the functionality and feasibility of the direct wave piezoelectric energy harvester model. An array of piezoelectric energy harvesters (identical to the piezoelectric element modeled) were fixed to the surface of an acrylic housing using rubber sealant, and the connecting circuitry was encased behind the frame and insulated from water, as shown below in Figure 16. This apparatus was then immersed in a wave tank made from plexi-glass, measuring approximately 7 m long by 0.4 m wide by 0.3 m deep. A column of water at room temperature and pressure was released into the wave tank, thus forming a wavefront that traveled across the tank and impinged on the piezoelectric array, causing the elements to deform. The water passed through an opening below the acrylic housing and drained out through an opening at the end of the tank. Measurements of the voltage outputs for each of the piezoelectric elements in the array were taken, which were then compared to the COMSOL model results.

Key differences between the model and the experiment include the dimensions of the wave tank and the number of piezoelectric elements tested. Tank dimension and the number of

elements have been reduced for modeling purposes in order to cut down on computation time. The wave velocity and piezoelectric element dimensions in the model, however, were matched to the experimental conditions when performing a comparison between results.

Figure 16: The experimental setup for the wave tank for demonstrating the direct wave piezoelectric energy harvester model; a) the wave tank and the positioning of the piezoelectric elements are shown and b) the support that contains the array of piezoelectric strips are shown in a close-up.

3.3.2. Indirect Wave Piezoelectric Energy Harvester Model

The indirect wave piezoelectric energy harvester (PEH) model has a few key differences from the direct wave PEH model. For example, the piezoelectric element is not placed in direct contact with water. Instead, vibrations are conveyed to the elements housed inside the buoy through vertically moving “arms”, as shown below in Figure 17. This structure is an extension of a decoupled spring system housed within the buoy, and is in contact with the water’s surface and captures the heaving motion of the waves. The spring system utilizes the vertical component of

the heaving motion, whose frequency is ramped up via this system and transferred to the piezoelectric elements (also housed within the buoy), thus exciting it to a frequency that is higher than the low frequency of ocean waves. The concept of this mechanism for frequency conversion is described in more details in Murray and Rastegar's work, which proposes a two-stage linear generator design for frequency-ramp up of ocean waves [170].

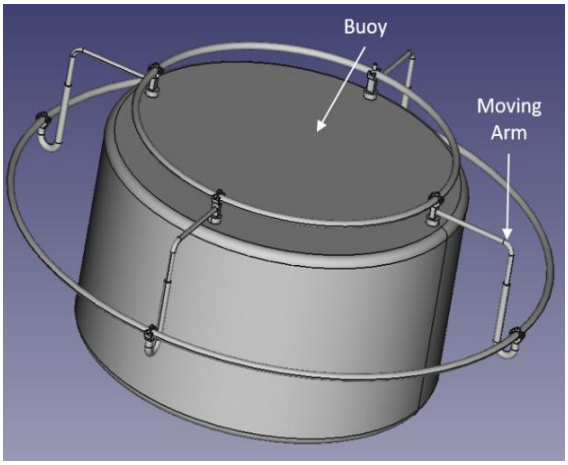

Figure 17: Proposed design for an ocean buoy fitted with the indirect wave piezoelectric energy harvesting device, where the "arms" convey the wave heaving motion to the piezoelectric elements housed within the buoy.

The indirect wave PEH model was built in COMSOL Multiphysics® with 2D geometry and is a steady-state frequency domain study. Dimensions for the piezoelectric element are identical to the flexible PVDF strip used in the direct wave PEH model. As shown below in Figure 18, the setup for the indirect model includes the piezoelectric element and two rigid supports attached to its ends. The left-side support is a fixed, anchored surface and does not move during the vibrations, whereas the right-side support is indirectly set into motion by waves, which eventually

causes the piezoelectric element to deform as it bends with the moving support. Notably, the motion of the right-side support is restricted to the y-direction only. The frequency conversion system used to convey the motion of the waves to the moving support at the free end of the piezoelectric element in this model has been omitted since it is not the primary focus of the simulation.

In-built physics modules in COMSOL Multiphysics® are used to define the model. For the sake of simplicity, the vibrations that are to be passed on to the piezoelectric strip via the displacement of the right-side support have been modeled by using a body load in the downward y-direction. The piezoelectric strip is assumed to be comprised of linear elastic material, with damping caused by an isotropic loss factor of 0.001. All surfaces except the left side of the fixed support is set as free-moving boundaries.

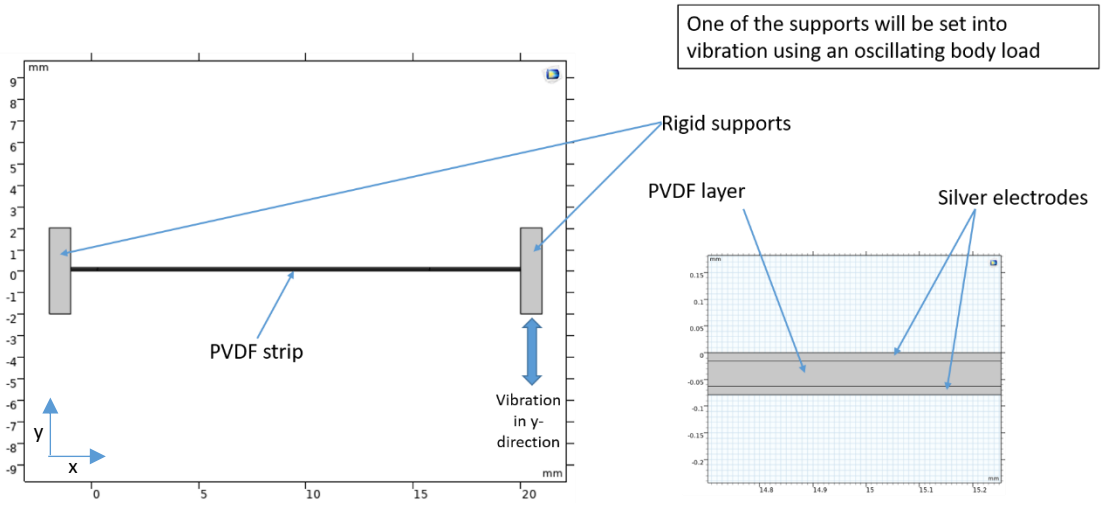

Figure 18: Geometry of the indirect wave piezoelectric energy harvester model on COMSOL® Multiphysics, where the PVDF strip deforms due to vibrations passed though the rigid support moving in the y-direction. This support is connected (not shown in image) to an external arm that is excited by the heaving motion of ocean waves.

The equation that regulates the motion of this setup in the frequency domain study is as follows:

$$-\rho\omega^2 u = \nabla.\sigma + F_v e^{i\phi} \tag{3-5}$$

where ρ stands for solid density, ω stands for frequency, u stands for the displacement vector, σ the stress tensor and F_v the force per unit volume and ϕ stands for the angle in radians which signifies the phase. The equation that defines its piezoelectric response is given by

$$D = d\sigma + \varepsilon_0 \varepsilon_{rT} E \tag{3-6}$$

where D is the electric displacement field, d is the coupling matrix, σ is the stress, ε_0 is the permittivity of free space, ε_{rT} is the relative permittivity at constant stress and E is the electric field.

Electrostatics is incorporated in the model to account for the separation of charges across the piezoelectric element. An external electrical circuit is added to this model, much like in the direct wave model, in order to connect the terminals of the piezoelectric strip and measure the resulting voltage and power outputs. The external resistance used in the electrical circuit is $1.2e^7$ ohms to match the internal impedance of the piezoelectric strip and thus maximize its power output.

A user-controlled free triangular mesh is implemented for this model. The size of the elements are restricted to a minimum of 0.0147 mm and a maximum of 3.28 mm. Frequency domain study has been used here to look at the influence that the frequency of vibrations has on the power and voltage outputs. The frequency range is varied between 0 and 110 Hz in increments of 1 Hz to result in finer resolution of the frequency profile.

Certain assumptions were made to reduce the complexity of the indirect wave piezoelectric energy harvester model, including the following:

1. The body load that acts as the force that excites the piezoelectric element only acts in a downward motion (i.e. negative y-direction) with zero motion in the x-direction.
2. The model is constructed in 2D in order to reduce run times for the simulation, as well as to be able to keep the results comparable to the 2D direct wave model.
3. Heat generated during operation is neglected.

3.3.2.1. Experimental Setup of Indirect Wave Energy Harvester Model

To demonstrate how the indirect wave PEH model could work, an experiment was conducted as shown below in Figure 19. This experiment consisted of a pair of identical springs attached in parallel to a wooden block. The piezoelectric strips were mounted to a separate wooden support, which tethered one end of the strip in a fixed position. The other ends, which were attached to the moving wooden block using alligator clips, are free to move in the y-direction only. A cylindrical dowel was attached to the bottom of the suspended wooden block and was inserted into a makeshift runner, such that the block is restrained to vertical motion and cannot sway or rotate. The experiment was set into motion when the free block is pulled downward manually with a force equivalent to 5 N. The spring system attached to the freely moving block then converted the subsequent oscillations to that of a higher frequency, and the resulting increase in frequency, in theory, led to a higher voltage output. An external circuit was attached to the piezoelectric element through the fixed wooden support and connected to an oscilloscope to measure its frequency and voltage.

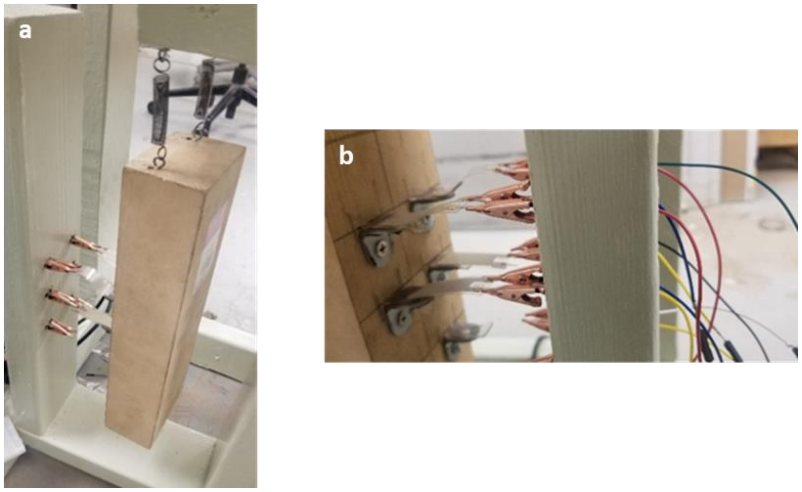

Figure 19: Experimental setup for demonstrating the indirect wave piezoelectric energy harvester model; a) an array of piezoelectric strips were connected to a fixed support and a moving wooden block with springs attached; b) a close-up of the individual piezoelectric elements and how they are connected through the supports to an electric circuit.

3.4. Results and Discussion

3.4.1. Direct Wave Piezoelectric Energy Harvester Model

3.4.1.1. Voltage and Power at Different Orientations

The piezoelectric element in the direct wave PEH model is positioned in two different orientations, at 0 degrees (horizontal) and 90 degrees (vertical) to the floor of the wave tank, as shown below in Figure 20A and Figure 20B. When water is flown at a velocity given by $V = 0.35 * 5 * tri(t)$, where the velocity rises from $V = 0$ at $t = 0$ to $V = 1.75$ m/s at $t = 0.3$ s, after which the velocity falls to 0 again by $t = 0.5$ s (i.e. end of simulation). The variation in velocity leads to

the voltage peaking at approximately 0.35 seconds for the case of both the orientations, where the peak voltage for the horizontal orientation is 2.5 V and 2 V for the vertical orientation (Figure 20C). The power output of the piezoelectric elements vary similarly as well, with the horizontal orientation resulting in $3.2e^{-5}$ mW and the vertical orientation $1.9e^{-5}$ mW, as shown in Figure 20D. Thus, it can be concluded that for the same conditions, the piezoelectric element in the horizontal orientation performs better in terms of both voltage and power output when compared to the element in a vertical position.

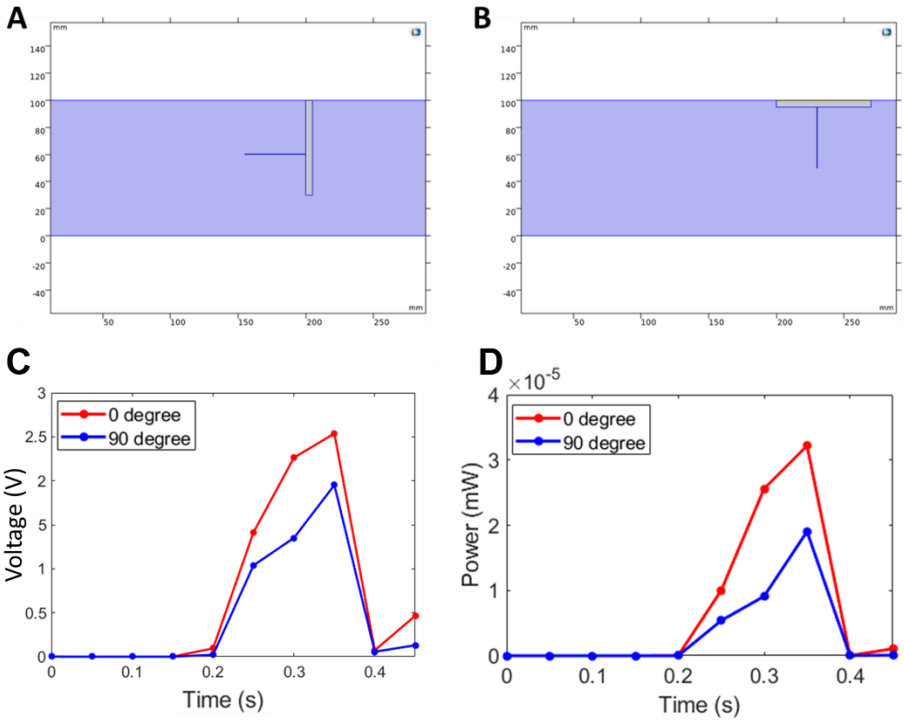

Figure 20: A) 0° orientation, and B) 90° orientation of the piezoelectric element, C) Voltage vs time plots for 0° and 90° orientations, and D) power vs time plots for 0° and 90° orientations.

3.4.1.2. Voltage and Power at Different Wave Velocities

The velocity of the water entering through the inlet of the wave tank is varied for the piezoelectric element at 0^o and its effects studied on the voltage and power outputs of the piezoelectric harvester. The velocity was varied according to equation (3-1) given under Section 3.3.1, where *m* is taken to be 1, 2.5, 5 and 7.5, thus resulting in peak velocities of 0.35 m/s, 0.875 m/s, 1.75 m/s and 2.625 m/s, respectively. The voltage outputs for each of these inlet velocities are shown in Figure 21A Figure 21B, where it is seen that the peak voltage varies between 0.04 V and 5.6 V. It can be concluded that the voltage output increases substantially with wave velocity. Following a similar trend, the power outputs also vary between $7.7e^{-9}$ mW and $1.5e^{-4}$ mW, with higher velocities resulting in higher power output. At higher velocities, the flexible piezoelectric element undergoes deformation to a higher extent, thus yielding more voltage and power. However, power output is still small, even with the fastest waves.

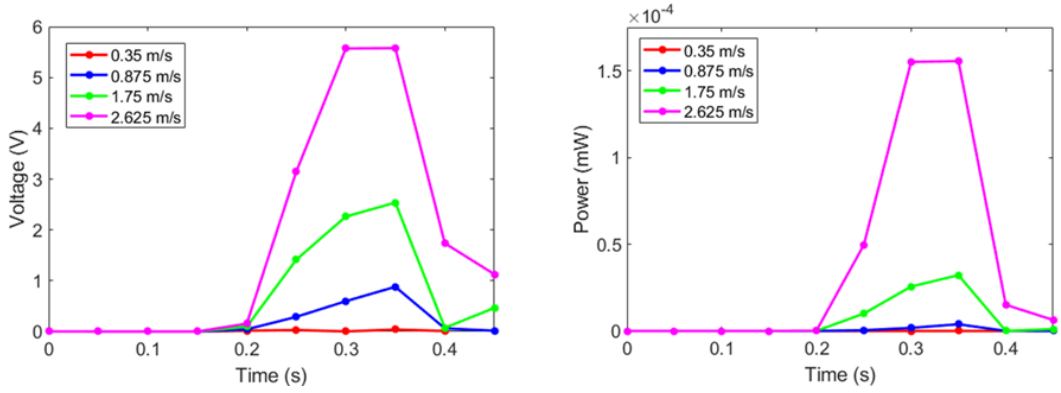

Figure 21: A) Voltage vs time plots for varying velocities show that higher velocities result in higher voltage output; B) Likewise, power vs time plots for varying velocities show that increase in velocity leads to increase in power output.

3.4.1.3. Experimental Demonstration of the Direct Wave Piezoelectric Energy Harvester Model

Representative data collected from the experiment run using the wave tank setup (shown in Figure 16) shows that the resulting voltage output is ~1 V for one of the piezoelectric elements. Though the profile for the other piezoelectric elements differ from one another (e.g. due to the differences in tank dimensions and other factors), all of them have a peak voltage within 1-1.5 V and follow similar patterns to the data shown in Figure 22. These experimental voltages are of the same order of magnitude as the voltage results found from the COMSOL® model for the direct wave PEH. The experimental voltage peaks are sharper than the simulated peaks, which are limited in sharpness by the triangle wave function. However, our model captures the general shape and magnitudes demonstrated by our experimental data.

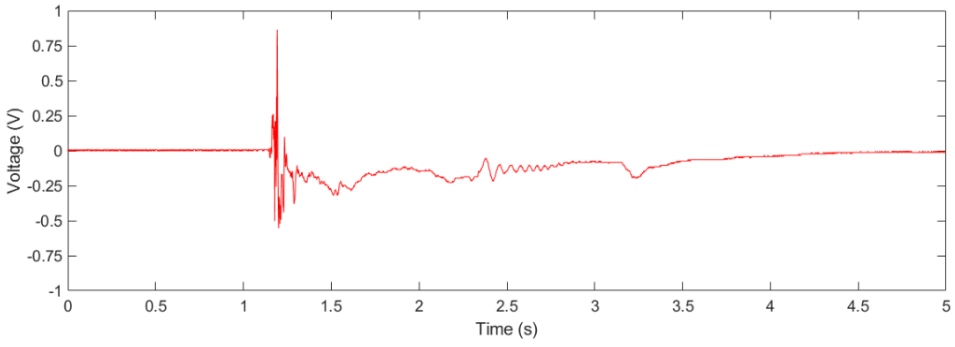

Figure 22: Voltage vs time plot for one of the piezoelectric elements in the wave tank experiment.

3.4.2. Indirect Wave Piezoelectric Energy Harvester Model

3.4.2.1. Voltage, Power and Resonant Frequency Variation at Different Piezoelectric Element Thicknesses

For the indirect wave PEH model, the thickness of the piezoelectric element is varied and its effect on the voltage and power outputs, as well as the resonant frequency of the device is observed. Figure 23A compares the voltage outputs and the resonant frequencies of the piezoelectric energy harvester with varying thicknesses of the PVDF strip, with the length and width being kept constant at 45 mm and 10 mm, respectively. The thicknesses used for this investigation are 0.13125 mm, 0.2625 mm, 0.39375 mm and 0.525 mm, which have been chosen as multiples. The figure shows that the voltage output decreases as the thickness is increased, likely due to the increasing stiffness of the strip and its diminishing ability to bend from the force of the incoming wave. Figure 23B shows that the power output decreases with increasing thickness as well. Lastly, the resonant frequency which results in the peak voltage and peak power outputs increases with thickness. For example, the resonant frequency of the piezoelectric element with the least thickness is ~18 Hz, whereas the thickest variation used in this study (i.e. 0.525 mm) results in a resonant frequency of ~100 Hz. This makes sense since a stiffer element will naturally have a higher resonant frequency. Hence, it can be surmised that the thinner the piezoelectric element, the more pliable it will be and hence the higher the voltage and power output produced by it. Also, the resulting strain produces a proportional voltage field, and hence the thicker the element, the lower the voltage output that will be produced since the voltage

field is distributed through a bigger area. There are, however, restraints on how thin of an element it is possible to fabricate.

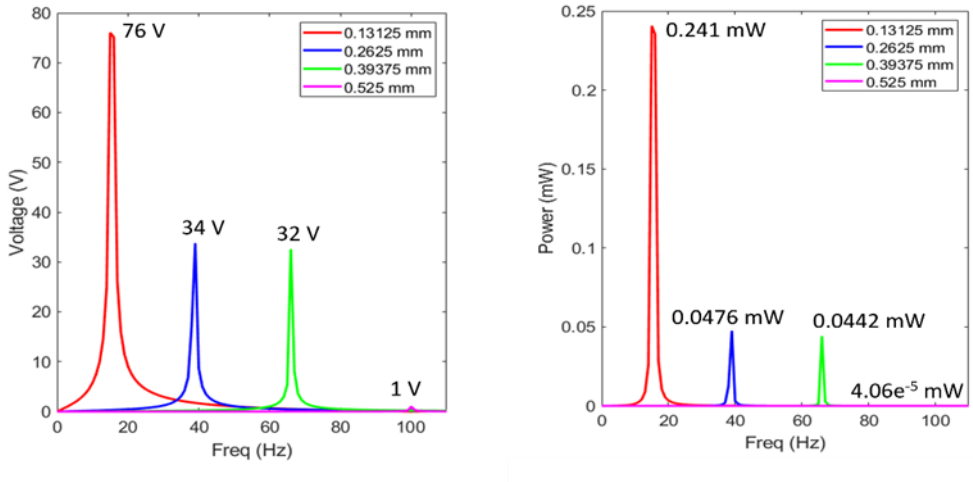

Figure 23: A) Voltage vs frequency plot for varying piezoelectric element thicknesses, where increase in thickness leads to lower voltage output and higher resonant frequency result in higher voltage output; B) Likewise, power vs frequency plot for varying piezoelectric element thicknesses, where increase in thickness leads to lower power output and higher resonant frequency.

3.4.2.2. Voltage, Power and Resonant Frequency Variation at Different Piezoelectric Element Lengths

Figure 24A and Figure 24B show the change in voltage and power outputs with variation in the length of the piezoelectric energy harvester. The length is varied between 25 and 65 mm, in increments of 10 mm, for a constant thickness of 0.2625 mm. Voltage increases as the length of the PEH increases, naturally following the consequence of having more cross-sectional area on the PVDF strip for charge separation. Likewise, the power output also increases with increasing

piezoelectric length. The resonant frequency of the energy harvester, on the other hand, decreases with increasing length. Thus, increasing the length of the piezoelectric element would be beneficial because the voltage and power outputs increase, while the resonant frequency of the element is also reduced (and thus can be matched easily by low frequency excitations).

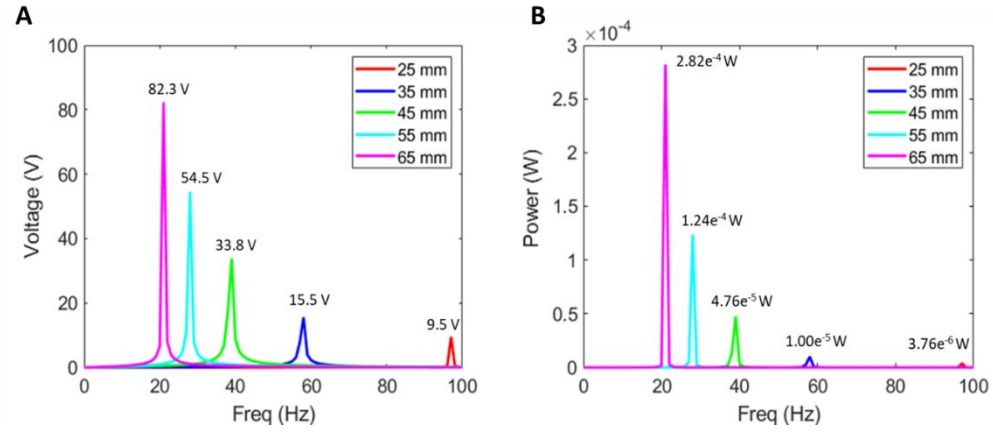

Figure 24: A) Voltage vs frequency plot shows that increase in piezoelectric element length leads to increase in voltage and decrease in resonant frequency; B) Power vs frequency plot shows that increase in piezoelectric element length leads to increase in power and decrease in resonant frequency.

3.4.2.3. Voltage, Power and Resonant Frequency Variation at Different End Loads

The downward load at the free end of the piezoelectric element is varied to show the influence of varying downward force on the voltage and power outputs of the element. Loads are varied between 250 g and 1500 g (approximate forces of 2.5 N and 15 N). It is observed that the higher the load at the end, the higher the voltage output (Figure 25A) and the higher the

power output peak (Figure 25B). This may be explained by the fact that increasing downward forces at the free end of the piezoelectric element enhances the deformation of the flexible strip. Though the voltage and power outputs increase with load, the frequency remains unchanged.

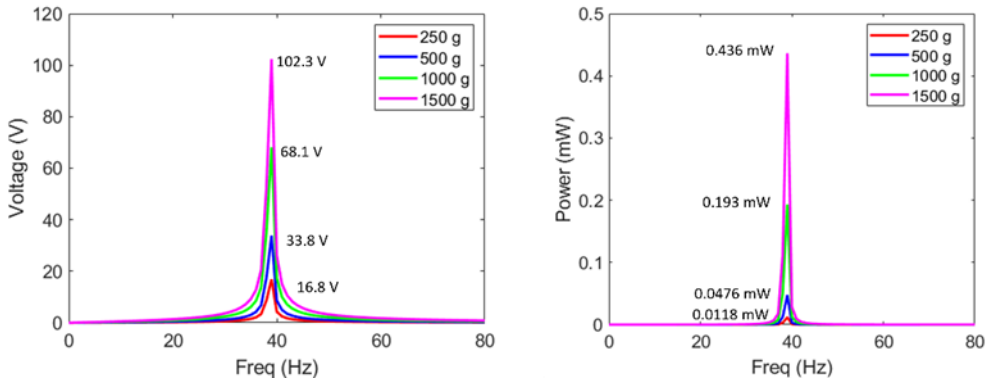

Figure 25: A) Voltage vs frequency plot for varying external physical load, where increase in load (or force) leads to increase in voltage output; B) Likewise, power vs frequency plot for varying loads, where increase in load leads to increase in power output

3.4.2.4. Experimental Demonstration of the Indirect Wave Piezoelectric Energy Harvester Model

Experimental data resulting from the lab setup described in Section 2.2.1 are shown in Figure 26. It is seen that the peak voltage is approximately 1-1.5 V, for a piezoelectric strip that has dimensions equal to 45 mm by 10 mm by 0.26 mm. It has been determined that the frequency of the oscillations that the piezoelectric elements were subjected to has an average value of 4 Hz. Referring back to Figure 23A and Figure 24A, a voltage of the order that was applied during the experiment at a low vibrational frequency of 4 Hz is thus consistent the modeling results that

were obtained. If the piezoelectric element was excited at higher frequencies (e.g. ~40 Hz, which is the resonant frequency for the element used in the experiments, as determined by the COMSOL model for the given dimensions), it would be possible to reach high voltage output values (e.g. ~34 V, as shown in Figure 23A and Figure 24A). However, since the frequency used to excite the piezoelectric element was very low, consequently the voltage output was low as well. Also, there may have been unaccounted dampening effect introduced into the experiment due to the use of multiple joints and hinges to hold the piezoelectric elements into place. Extra dampening could also be responsible for reducing the voltage output.

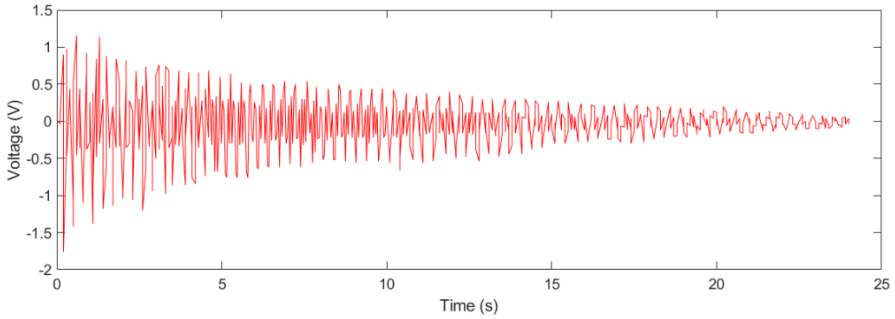

Figure 26: Voltage vs time plot for a single piezoelectric element in the indirect wave PEH experiment.

3.4.3. Techno-economic Analysis of Piezoelectric Energy Harvesting Device for an Ocean Observation Buoy

A brief, simplified techno-economic analysis helps to compare the relative merits of the two proposed designs for a PEH device to power buoys from ocean waves. Real-life

implementation of this device will require estimates of cost and size, which is the purpose of this section.

Of the two models proposed, it seems that the indirect wave piezoelectric energy harvester exceeds the direct wave piezoelectric energy harvester model in peak power production due to the ability to reach higher frequencies. Though modeling results show what the peak voltage and peak power of the different models under varying conditions will be, it is more important to be able to compare their average power production. This is found out by calculating the area under the power versus time curves for the individual models, which will ultimately result in the measurement of energy produced over a given time span. Trapezoidal numerical integration is used in MATLAB to estimate the area under the curves, since they lack any defining equations. Using the equation $P = E/t$, the energy (E) when divided by time (t) gives a measure of the average power (P) produced in the case of each of the models. Figure 27 shows the power vs time plots for the direct wave and indirect wave PEH models under baseline conditions (to be explained shortly), and a line to indicate the calculated average power production for each scenario.

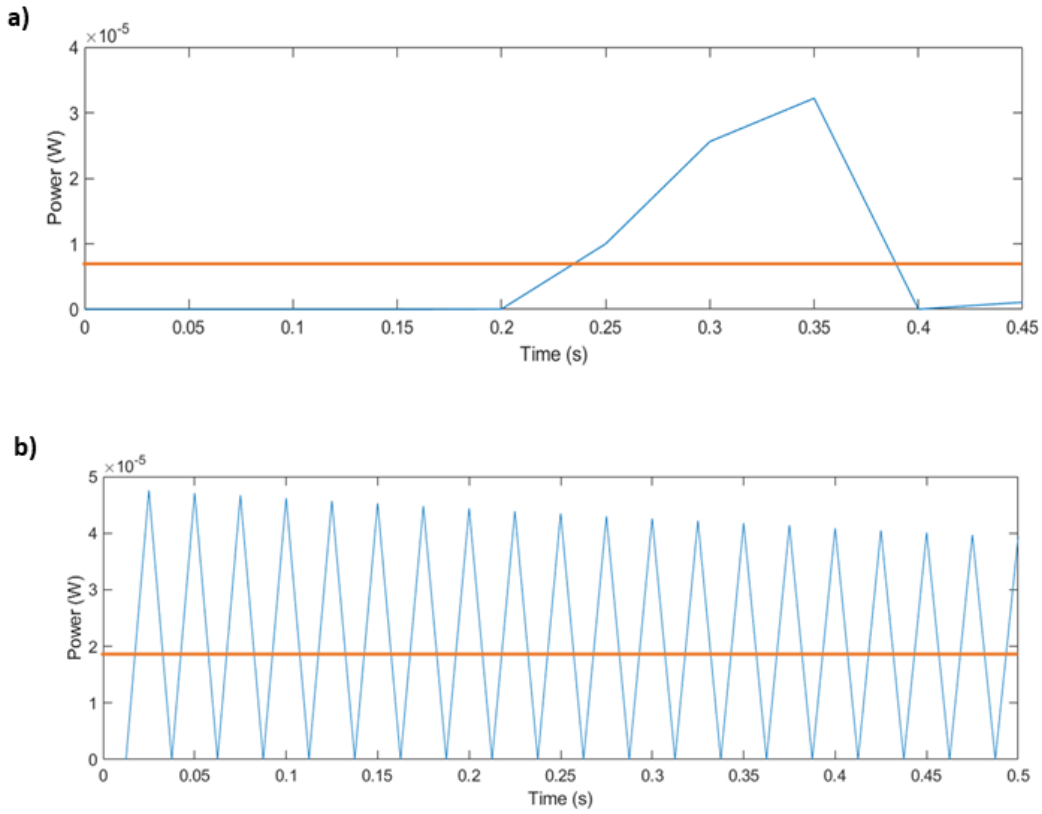

Figure 27: Power vs time plots for the baseline cases for a) the direct wave PEH model, and b) the indirect wave PEH model. Area under the curves are estimated using the trapezoidal numerical integration function in MATLAB, which gives the energy for the measured time span. This is then divided by the time to provide an estimated value for the average power production for each model (as indicated by the red line).

Two cases each were analyzed here for the individual models: a baseline case that replicates the conditions of the experiments conducted, and an optimal case which combines all the conditions that lead to the highest power output during modeling. The input conditions and the energy and power production results of the 4 cases are provided in Table 4 and the average power produced by all 4 cases are depicted in the bar chart in Figure 28. It can be observed that the optimal cases for the direct wave PEH and indirect wave PEH models logically lead to higher

average power. In Figure 27, the power vs time curves for the baseline cases for the direct wave PEH and the indirect wave PEH are shown, along with a line to indicate what the average power production for each of the cases would be. It is seen, however, that the indirect wave PEH model results in power output that is an order higher than the direct wave PEH model. This indicates that the indirect wave PEH model is perhaps the more promising model of the two.

Table 4: The inputs used and the total energy and average power calculations for the 4 different cases for the direct and indirect wave PEH models are listed below.

	Direct Wave PEH Baseline	**Direct Wave PEH Optimal**	**Indirect Wave PEH Baseline**	**Indirect Wave PEH Optimal**
Wave Velocity, m/s	1.75 m/s	2.625 m/s	--	--
Orientation, degrees	0	0	--	--
Length, mm	45	45	45	65
Thickness, mm	0.26	0.26	0.26	0.13125
Load at tip, g	--	--	500	1500
Time span, s	0.45	0.45	0.5	0.5
Total Energy, J	3.42E-9	1.89E-8	9.69E-6	1.38E-4
Average Power, W	7.60E-9	4.20E-5	1.94E-2	2.76E-1

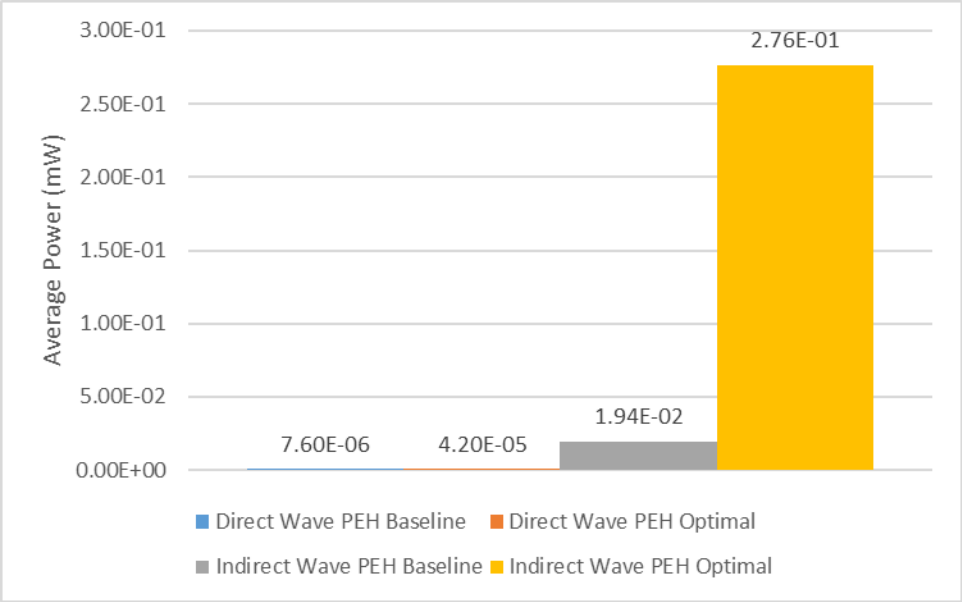

Figure 28: Calculated values for the average power production for baseline and optimal modeling cases for direct and indirect wave piezoelectric energy harvesters are shown, where the optimal case for the indirect wave PEH model far exceeds the other 3 cases in average power production.

As such, the number of piezoelectric elements required for a production of 10 W to power the instrumentation aboard the buoy is calculated. 10 W is sufficient to power over half of the instrumentation typically installed on an observation buoy, which is why this amount was chosen as a good representation for estimation purposes [163]. As shown in Figure 29 below, the number of elements needed for the baseline case direct wave model is by far the highest. In general, the indirect wave model requires fewer piezoelectric elements to produce the required power of 10 W, with the optimal case for the indirect wave model needing approximately 6 times less the number of elements than the optimal case for the direct wave model. It is also to be noted that the number of elements for the direct wave PEH optimal case is about 5 times less than that

required for the baseline case of the same model, whereas for the indirect wave model, the optimal case requires 14 times fewer elements than the baseline case.

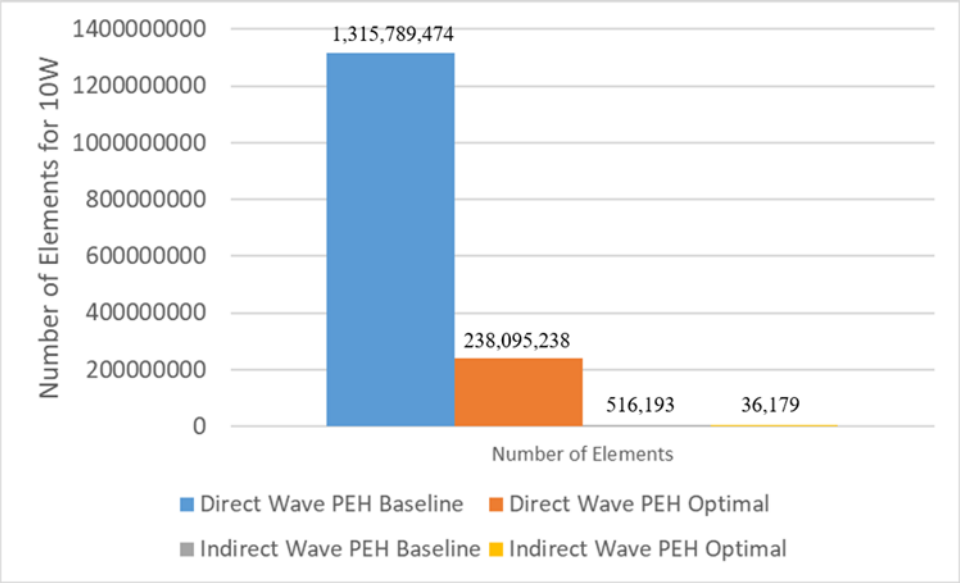

Figure 29: The number of piezoelectric elements required to supply 10 W for each of the cases.

The cost of the piezoelectric energy harvester is assumed to be majorly comprised of the cost of the piezoelectric elements, which is taken to be $0.50/element, given the low cost of PVDF and the scales of economy resulting from the massive amount of piezoelectric elements required. Hence, the case that requires the highest amount of piezoelectric elements would naturally cost more. As shown in Figure 30, the indirect wave PEH device incurs lesser costs in both baseline and optimal cases. The indirect wave PEH device in the optimal case has piezoelectric elements that cost approximately $18,000. These costs will of course increase when the wiring and circuitry, as well as the means to insulate the PEH device, is taken into account.

However, it can be predicted that the indirect wave PEH will cost less than the direct wave PEH because its elements do not need to be individually insulated and remain encased and out of direct contact with water.

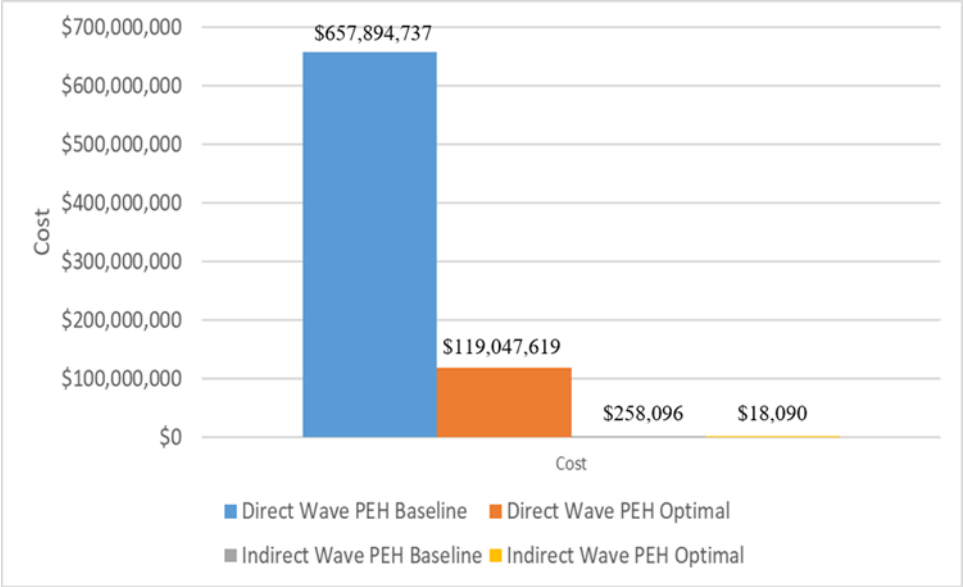

Figure 30: Cost estimation for the piezoelectric elements required to supply 10 W for each of the cases.

Lastly, the estimated combined volume of the elements for each of the devices in the two different cases is also calculated. The allowance for each element to bend and spring back was estimated to be 20*60*20 mm^3, corresponding to the thickness, length and width of the piezoelectric elements, respectively. As shown in Figure 31, both the baseline cases for direct and the indirect PEH devices will take up an enormous amount of space. Only the optimal case for the indirect wave PEH yields a volume that can be considered within reasonable bounds, especially when considering the volume of the buoy itself.

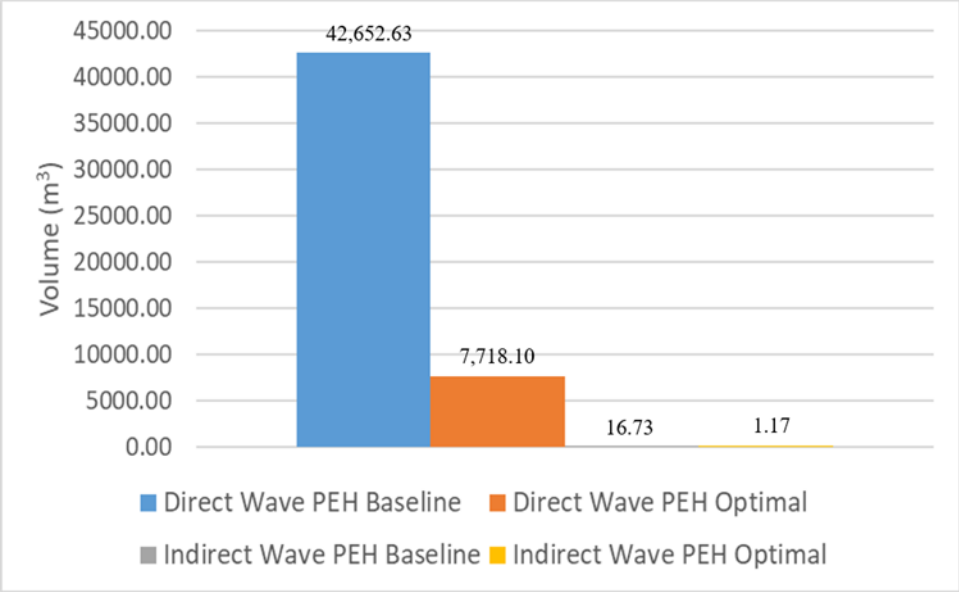

Figure 31: Volume estimation for the piezoelectric elements required to supply 10 W for each of the cases.

A comparison of the techno-economic analysis results of the direct wave and indirect wave piezoelectric energy harvester models leads to the understanding that the indirect wave model performs better than the direct wave model. Since the average power output per piezoelectric element is 4 orders higher for the indirect wave PEH model when compared to the direct wave model, it follows through that the number of piezoelectric elements required to meet a specified power production will be fewer for the indirect wave in comparison to the direct wave model. As such, the cost and volume taken up by the indirect model will also be less. This is especially true when the optimal cases are compared, leading us to infer that adjusting the input conditions for the indirect wave model can greatly improve performance

It is to be noted that the lowest possible cost achieved for producing 10 W of power to run the equipment on board the observation buoy is approximately $18,000. When comparing

this price estimate to existing energy harvesting technology leveraged by ocean buoys today, it is clear that PEH technology is not currently cost-competitive. For example, a commercially available 10-watt solar cell costs less than $50 currently, which is far less than the price estimated for the optimal case of the indirect wave PEH [171]. Those numbers, however, are the results of preliminary investigation, and shows that there is room for improvement and future research. In particular, piezoelectric energy harvesters with higher power output than PVDF could dramatically reduce the system size and cost.

3.5. Conclusion

This work consists of designing two separate piezoelectric energy harvester models with the purpose of harvesting energy from ocean waves. The models are tested to gauge their performance in harvesting energy to provide power for an ocean observation buoy deployed at sea. COMSOL Multiphysics® is used to set up simplified models for the direct wave and the indirect wave piezoelectric energy harvesters. Though both models essentially take advantage of piezoelectric conversion to harvest mechanical energy from the waves and transfer it to usable electrical energy within a circuit, the direct wave PEH has its piezoelectric elements in contact with the waves whereas the indirect PEH has its elements placed above water and excited by a frequency conversion system that has one end ideally in contact with surface waves. The simplified models for both these setups are designed to measure the power and voltage outputs for varying input conditions, as well as the resonant frequency that results from those different conditions for the indirect wave PEH model. Experiments are also conducted to validate the findings from the model and provide proof of concept for these piezoelectric energy harvesters.

The modeling results from COMSOL shows that the indirect wave PEH produces more power than the direct wave PEH, provided that it is functioning at its resonant frequency. It is seen that the cost and volume associated with the indirect wave PEH is also low in comparison, thus making it the more practical device to work with.

The scope of this research is to explore the potential for applying piezoelectric energy harvesters to capture ocean wave energy efficiently to power deep-sea vehicles such as ocean observation buoys. Though piezoelectric energy harvesting has been employed previously in harvesting energy from ambient vibrations in an industrial setting or from roadside vibrations, when applied to ocean waves, it shows a low output mainly due to the low frequency of the waves. This work attempts to explore a piezoelectric energy harvester design that can lead to potentially alleviating this problem by ramping up the frequency of vibrations from the waves when they impinge on its piezoelectric elements. Though the techno-economic results of this study indicate that piezoelectric wave energy harvesters aren't currently cost-competitive with other forms of renewable energy (e.g. solar power), future work should be done to explore other flexible piezoelectric composite materials that can achieve better power output. Also, the frequency ramp-up system used in the indirect wave PEH model should be explored more closely to investigate if the low frequency of ocean waves can be converted to a higher frequency.

4. Flexible Carbon Capture Using MOF Fixed Bed Reactors at an NGCC Plant

Novel carbon capture systems are necessary to help natural gas power plants approach net zero CO_2 emissions. We propose a hybrid carbon capture system attached to a natural gas combined cycle (NGCC) power plant that consists of a membrane system and a solid sorbent system, with this work focusing on the design and optimization of the solid sorbent system. We modeled fixed bed reactors that are packed with metal-organic framework (MOF) solid sorbents that adsorb CO_2 and undergo temperature swing desorption using steam from the power plant. Optimization of reactor conditions showed that ten 5-meter diameter beds adsorbing in parallel with 5 bars inlet gas pressure and 1.5 bars of steam pressure at a flow rate of 0.15 kmol/s led to optimized performance. This study enabled us to determine that the MOF bed reactor can attain 86.6% and 85.4% carbon capture during peak and off-peak operation, respectively. When combined with the membrane capture system, this results in overall capture rates of 98.4% and 98.9% during peak and off-peak operation, respectively. These results indicate that our hybrid carbon capture system could enable NGCC plants to obtain near-net zero carbon footprints.

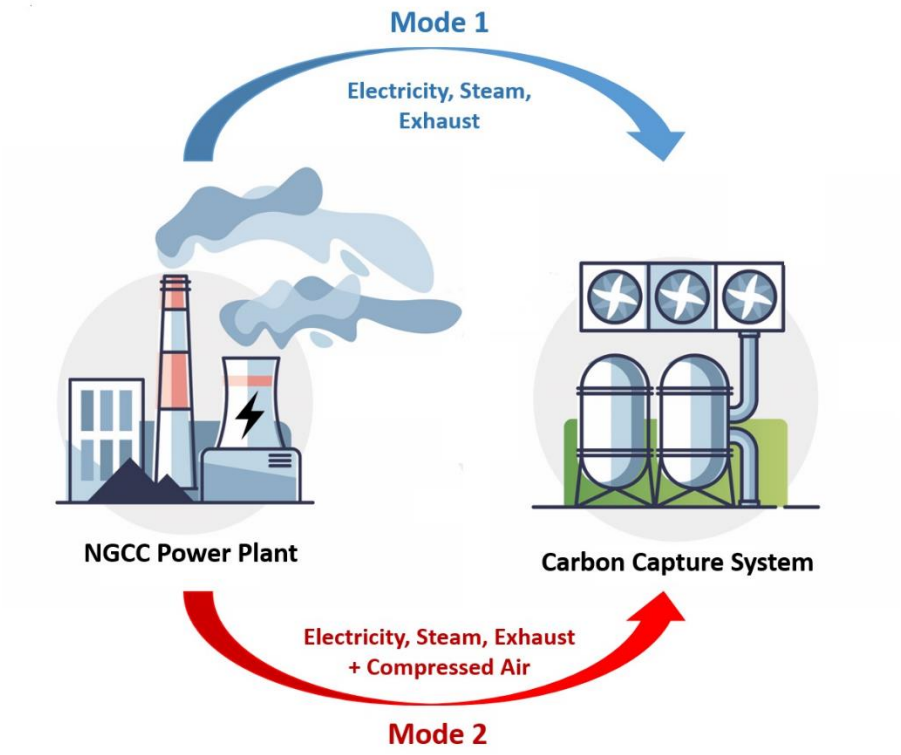

Figure 32: There are two modes of operation of the solid sorbent system: Mode 1, where CO_2 is captured from the NGCC plant's exhaust only, and Mode 2, where CO_2 is removed from the air in addition to the power plant's exhaust

4.1 Introduction

CO_2 concentration in the atmosphere has risen from 280 ppm to approximately 418 ppm due to the increased use of fossil fuels following the Industrial Revolution [172], [173]. This is cause for concern because CO_2 is a major greenhouse gas and is the primary cause of global warming [174]–[176]. A way to address this concern is by devising methods to capture CO_2 from power plant flue gas, i.e. post-combustion capture. For example, He et al. investigated the scheduling and optimization of a MEA-solvent based carbon capture plant that was integrated with an NGCC power plant to clean up its exhaust [177]. Diego et al. studied the integration of a

hybrid capture system that consisted of a CO_2 selective membrane and an amine scrubbing plant with an NGCC power plant [178]. While certain power production and manufacturing industries have devised point-source carbon capture systems to reduce the amount of CO_2 they release into the air, post-combustion capture is not yet feasible for other major CO_2 producing sectors, such as the transportation industry, which accounts for nearly 50% of greenhouse gas emissions [179]–[181]. Therefore, to mitigate global warming long-term, we must also implement negative emissions technologies, such as direct air capture, to offset difficult-to-abate long-term CO_2 emissions.

While using fossil fuels as the energy source for running direct air capture (DAC) may seem contradictory, it will be expensive and impractical to power DAC using renewable sources alone, as this will require massive land space and capital cost. Coupling DAC with fossil fuels could also enable rapid scale-up by leveraging existing infrastructure, and reduce operating costs by taking advantage of the electricity, steam, and compressed air from the power plant. The FLECCS (FLExible Carbon Capture and Storage) program under ARPA-E was designed to investigate how to leverage fossil fuels to perform DAC and other beneficial functions long-term. Research conducted under this program included work by Realff et al., which proposed combining an NGCC power plant with an amine scrubbing plant and a modular DAC system [182]. Another project funded by this program was led by Herzog et al., which involved capturing CO_2 from flue gas from a power plant using a calciner along with a lime-based DAC system [183]. The research presented in this paper, which is also a part of the FLECCS program, proposes the use of a hybrid membrane + solid sorbent carbon capture system retrofitted to an NGCC power plant. This is a novel concept that proposes operating the NGCC power plant during off-peak hours (when the plant would

normally power down) to perform direct air capture in the solid sorbent fixed bed system. The hybrid carbon capture system will thus capture CO_2 from both the power plant exhaust and from the air. The membrane system is upstream of the solid sorbent system and acts as the primary point-source carbon capture system, while the sorbent system captures both CO_2 from the membrane exhaust and CO_2 from the air. Thus, the hybrid carbon capture system is not only designed to perform high levels of carbon capture, but it is also adaptable to changes in the grid. Gokhan et al. from TDA Research have previously developed and successfully pilot-tested a hybrid membrane-sorbent system for post-combustion capture from large-scale CO_2 emitters such as refineries and coal power plants [184], [185]. Our work builds on this concept and takes it a step further to perform direct air capture in addition to point source capture during off-peak hours.

Note that the scope of this paper only involves the design and process optimization of the fixed bed reactor system, since the MTR membrane used in our system has already been extensively modeled and studied for NGCC capture [186]–[188]. Figure 33 below illustrates Modes 1 and 2 for our integrated system at a high level. During Mode 1 (normal operation), the NGCC plant sends electricity to the grid, and the hybrid carbon capture system simply captures CO_2 from the NGCC exhaust. For the solid sorbent system, this means that it only needs to process the membrane exhaust during Mode 1. During Mode 2 operation (off-peak operation), the NGCC plant no longer sends electricity to the grid, and only operates to power the carbon capture systems. During Mode 2, the solid sorbent beds remove CO_2 from both the membrane exhaust and from air. This air can come from a combination of ambient air and compressed air tapped from the natural gas compressor. The membrane system enables rapid response times, while the

sorbent system enables higher carbon capture rates. The proposed system could theoretically achieve net-zero or even net-negative CO_2 emissions overall if Mode 2 operates often enough and removes enough CO_2 from the air to offset CO_2 emissions during Mode 1.

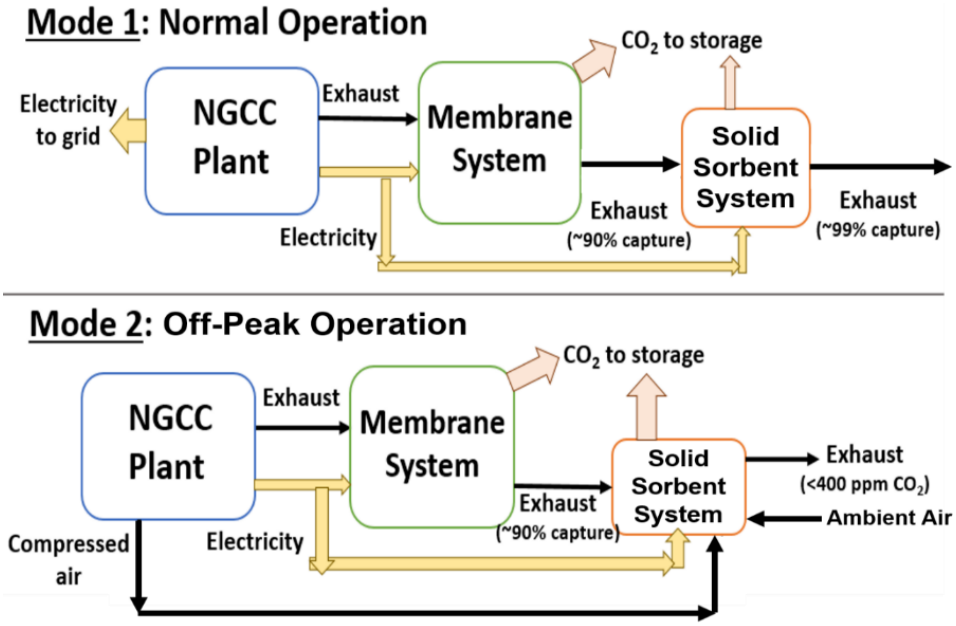

Figure 33: Mode 1 and Mode 2 operation of our integrated NGCC carbon capture system. Mode 1 refers to normal operation where the NGCC plant provides electricity to the grid and the hybrid carbon capture system captures CO_2 from the NGCC exhaust. Mode 2 refers to off-peak operation, where the NGCC plant does not send electricity to the grid. During Mode 2, the solid sorbent system captures CO_2 from air in addition to the membrane exhaust. This air can come from compressed air siphoned off the natural gas compressor and/or ambient air from the surroundings. If the CO_2 in the solid sorbent system exhaust is < 400 ppm, then the overall system is performing negative emissions in Mode 2.

We selected solid sorbents instead of aqueous solvents for our reactors because solid sorbents generally need lower energy and operating cost to run and can better handle low CO_2 concentration capture [189], [190]. The solid sorbent selected for our system must be able to

capture CO_2 under conditions ranging from NGCC exhaust (~40,000 ppm CO_2) to unpressurized air (~400 ppm CO_2). It was also important to select a sorbent that can withstand humid conditions and use steam for temperature swing desorption (since steam is abundant in NGCC plants). Metal-organic frameworks (MOFs) are a type of solid sorbent that consist of metal ions linked to an organic ligand that can adsorb gases selectively. Several MOFs have demonstrated high selectivity towards CO_2, and can be used for carbon capture in both post-combustion and direct air capture scenarios [191], [192]. For example, Sinha et al. investigated the adsorptive performance of two MOFs, MIL-101(Cr)-PEI-800 and mmen-Mg_2(dobpdc), for direct air capture, and found that the latter was favorable because of its lower energy requirements [193]. McDonald et al. found that mmen-Mg_2(dobpdc) has an CO_2 adsorption capacity of 2.0 mmol/g at 0.39 bars and 25 °C and 3.14 mmol/g at 0.15 bars and 40 °C, and is thus an excellent sorbent for both direct air capture and post-combustion capture conditions [194].

Since our carbon capture system is retrofitted to a NGCC power plant and captures CO_2 from power plant exhaust as well as air, we selected a solid sorbent that can capture CO_2 over that wide range of conditions. More specifically, we selected a tetraamine-appended Mg_2(dobpdc)(3-4-3) MOF material recently developed by Dr. Jeffrey Long's group at UC Berkeley [195]. This MOF material has a high breakthrough capacity of 2.0 ± 0.2 mmol/g at 100 °C under humid conditions and a 90% CO_2 capture rate for natural gas exhaust [195]. It shows stability in the presence of steam, and can thus be regenerated using low-grade steam instead of high temperatures. While this sorbent has been proposed as an excellent sorbent for post-combustion capture of natural gas, it was also shown to be capable of adsorbing CO2 at lower concentrations,

thus making it a potential sorbent for a direct air capture system. In addition to that, the unique dual-step shape of its isotherms can be exploited in our process-level design.

The scope of this paper covers the design and optimization of the solid sorbent carbon capture system. First we describe our efforts to model the isotherms of the tetraamine-appended MOF used in our fixed bed reactor model (Section 4.2.1). Next, we describe our MOF fixed bed reactor model setup and governing equations (Section 4.2.2). We then present the results of optimizations that we ran to determine the optimal adsorber bed design and operating conditions (Section 4.3.1). Then we present the results for Mode 1 & Mode 2 operation of our optimized adsorber beds (Section 4.3.2). Finally, we investigate the impact of adding excess ambient air to our adsorber bed during Mode 2 (Section 4.3.3) and discuss our conclusions (Section 4.4).

4.2 Methodology

4.2.1 Isotherm Modeling

To the best of our knowledge, no model exists that describes the isotherm behavior of the tetraamine-appended Mg_2(dobpdc) MOF material. The experimental adsorption isotherm data for this MOF material, for temperatures ranging between 90-120 °C, is shown below in Figure 34 (reproduced with permission from [195]). Its dual-step adsorption curve does not fit the traditional single-step isotherm models. However, several isotherm models exist that may be modified and adapted to fit this unique double-step shaped isotherm [196]–[200]. Of these isotherm models, Hughes et al. determined that the Dual-site Sips isotherm model could be fitted to a close degree to the step-shaped isotherms of a similar MOF material developed by the same

research group [200], [201]. Due to the similarities in structure between these two MOFs, it was determined that the Dual-site Sips model should be implemented to the tetraamine-appended Mg_2(dobpdc)(3-4-3) MOF selected for this study.

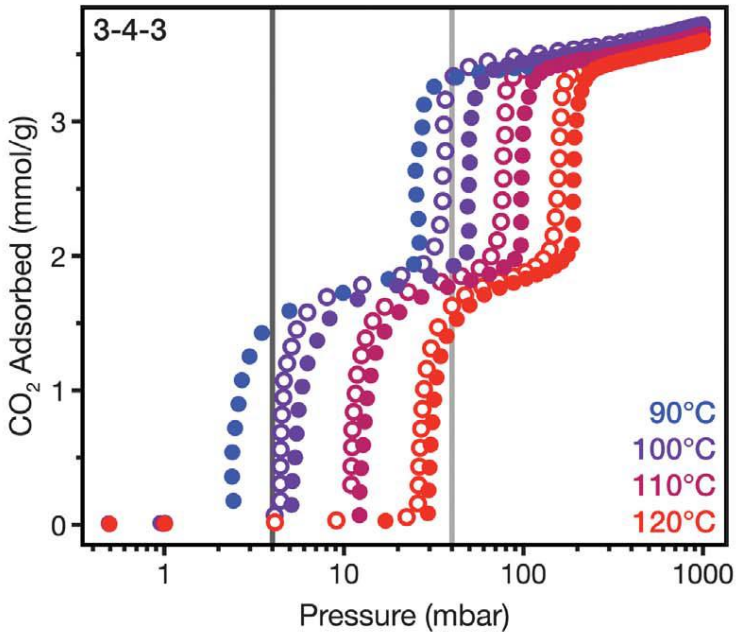

Figure 34: Experimental isotherm data for the Mg_2(dobpdc)(3-4-3) MOF material selected for our model, where filled circles denote adsorption isotherms and open circles denote desorption isotherms. Figure reproduced with permission from [195].

In order to adapt the Dual-site Sips model to our MOF material, the FMINCON optimization routine in MATLAB was used. This routine minimized the difference between the experimental isotherm data points and the data predicted by the isotherm model to yield the best possible fit of the model to the experimental isotherms. A detailed explanation of the isotherm model equations and the optimization function can be found in the work by Hughes et

al. [200], from which this model was adapted. A set of 12 fit parameters resulted from this optimization, which were then used to adapt the equations for the Dual-site Sips isotherm model such that they defined the isotherm curves of the tetraamine-appended MOF with acceptable accuracy. Table 5 presents the modified Dual-site Sips isotherm equations that fit the isotherm data for Mg_2(dobpdc)(3-4-3), where $q^*_{CO_2}$ is the total CO_2 equilibrium loading, n_{max_c} is the maximum chemisorption at a site, n_{ma_p} is the maximum physisorption at a site, b_a and b_b are adsorption equilibrium constants, n_a and n_b account for surface inhomogeneity, P is the pressure and T is the temperature, and reference temperature for the model is arbitrarily taken to be 385 K. Table 6 presents the fitted parameters for the isotherm model that have been found using the FMINCON routine on MATLAB. Initial values for the parameters were taken from a previously developed model by Hughes et al. [200], which fitted the Dual-site Sips isotherm model to a similar MOF, dmpn−Mg_2(dobpdc).

Table 5: Modified Dual-site Sips isotherm equations for the Mg_2(dobpdc)(3-4-3) MOF

$$q^*_{CO_2} = n_{max_c}\left[\frac{(b_a.P)^{\frac{1}{n_a}}}{1+(b_a.P)^{\frac{1}{n_a}}}\right] + n_{max_p}\left[\frac{(b_b.P)^{\frac{1}{n_b}}}{1+(b_b.P)^{\frac{1}{n_b}}}\right]$$	(4-1)
$$n_{max,c} = 3.840\left[\frac{\exp\left(-0.997+\frac{325.636}{T}\right)}{1+\exp\left(-0.997+\frac{325.636}{T}\right)}\right]$$	(4-2)

$$n_{max,p} = 1.772\left[\frac{\exp\left(-55.557 + \frac{28000.040}{T}\right)}{1 + \exp\left(-55.557 + \frac{28000.040}{T}\right)}\right] \quad (4\text{-}3)$$

$$n_a = 0.071\left\{\exp\left[\frac{60.655}{(8.314e^{-3})(385)}.\left(\frac{385}{T}\right) - 1\right]\right\} \quad (4\text{-}4)$$

$$n_b = n_{b_1} = 0.059 \quad (4\text{-}5)$$

$$b_a = 56.218\left\{\exp\left[\frac{94.095}{(8.314e^{-3})(385)}.\left(\frac{385}{T}\right) - 1\right]\right\} \quad (4\text{-}6)$$

$$b_b = 8.731\left\{\exp\left[\frac{79.382}{(8.314e^{-3})(385)}.\left(\frac{385}{T}\right) - 1\right]\right\} \quad (4\text{-}7)$$

Table 6: Parameters of the Dual-site Sips model fitted to the isotherm data

Theta	Parameter	Initial Value Used	Optimum Value
Theta (1)	b_{a0}	28.5	56.22
Theta (2)	Q_{sta}	72	94.09
Theta (3)	n_{a1}	0.3	0.07

Theta (4)	b_{b0}	0.7	8.73
Theta (5)	Q_{stb}	45	79.38
Theta (6)	n_{b1}	1.6	0.06
Theta (7)	n_{maxp1}	3	1.77
Theta (8)	K_a	-0.92	-1.00
Theta (9)	K_b	325	325.64
Theta (10)	E_{na}	11.29	60.66
Theta (11)	K_c	-71.14	-55.56
Theta (12)	K_d	28000	28000.04

Figure 35 compares the predictions of the optimized model to the experimental data, where the experimental data points are indicated by the asterisks, and the colored lines denote the isotherm curves predicted by the Dual-site Sips isotherm model. It can be seen that the Dual-site Sips isotherm model fits the experimental isotherm data for the tetraamine-appended Mg_2(dobpdc) MOF material to an acceptable degree, with slight variations at the top of the curves

explained by experimental drift behavior. Thus, we were able to use these fitted isotherm curves in our fixed bed reactor model to predict the MOF's adsorption behavior.

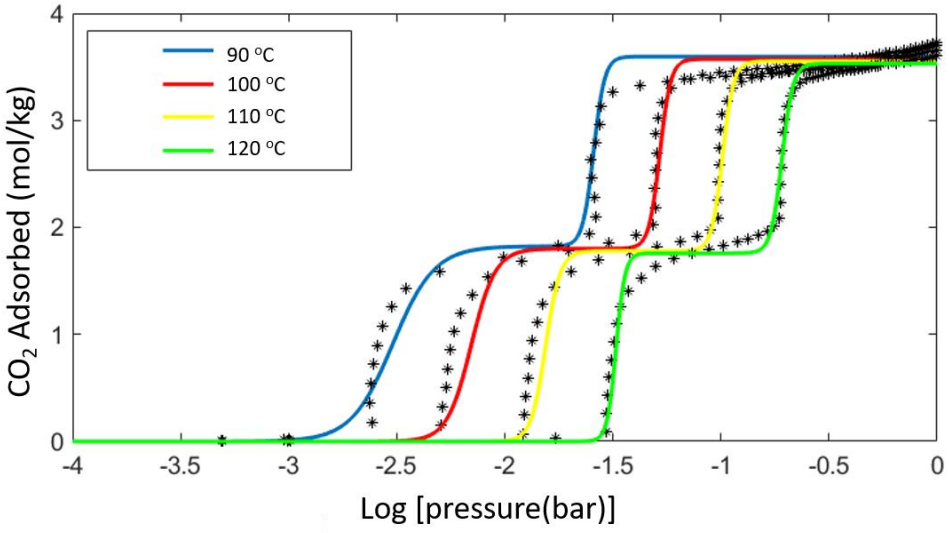

Figure 35: The Dual-site Sips model was fitted to the experimental isotherm data of the tetraamine-appended Mg_2(dobpdc) MOF material, where the experimental data is denoted by asterisks and the colored lines denote the model predictions.

4.2.2 Fixed Bed Reactor Model

The MOF fixed bed reactor system was modeled using Aspen Adsorption™ and was adapted from a similar model developed by Hughes et al. [200]. The MOF fixed bed reactor model is represented by the flow diagram shown in Figure 36. The reactor vessel in this model is a cylindrical-shaped, fixed bed packed with spherical, tetraamine-appended Mg_2(dobpdc) MOF particles with radii of approximately 0.2625 mm. Fixed bed reactors are chosen to reduce

attrition of particles and the bed size, while taking care to limit the pressure drop across the beds. One reactor bed is modeled undergoing adsorption & desorption cycles, the results of which will be multiplied to scale up because in reality, several beds would be operating simultaneously. The number and the dimension of the beds, as well as the conditions within the reactor (e.g., temperature, pressure, flow rate) are presented later in this paper.

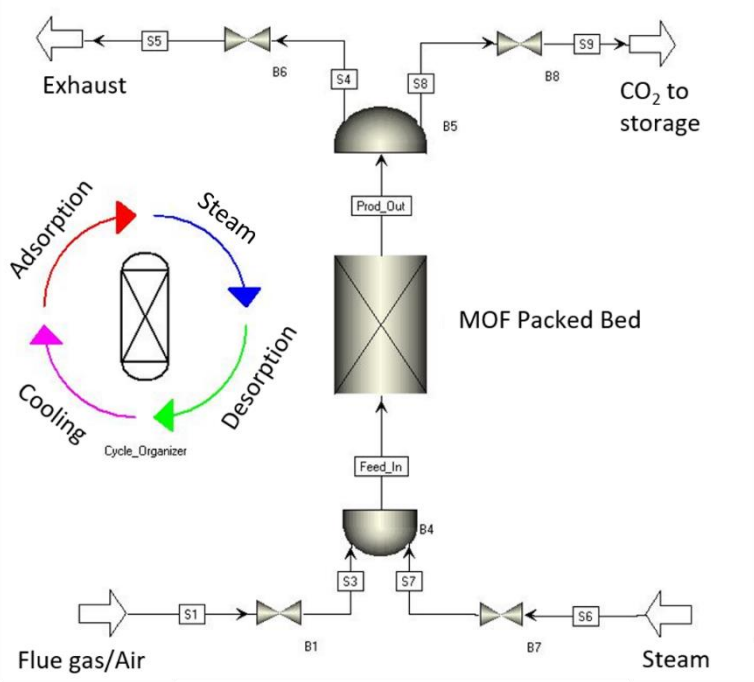

Figure 36: Flow diagram of MOF fixed bed reactor model developed in Aspen Adsorption™. The model is of a single packed bed of MOF solid sorbent pellets, and cycles between adsorption, steam pre-heating, steam desorption and cooling. The MOF packed bed is one dimensional in the flow direction with Node 1 at the bottom and the final node at the top.

The reactor bed needs to be heated and cooled in order for the MOF material to complete the temperature swing regeneration processes. The heating and cooling of the beds were achieved by internal heat exchangers that use water as the heat transfer medium, while the system outer boundaries were modeled as adiabatic. During the adsorption process, the heat exchanger maintained the bed temperature at 50 °C. During the desorption process, the heat exchanger rapidly raised the bed temperature using water at 150 °C passing at 275 kg/s within the heat exchanger. Once the MOF material desorption process was completed, the bed was cooled back down from 150 °C to 50 °C using a water flow rate of 500 kg/s at 50 °C. The internal heat exchangers were shell-and-tube exchangers with a tube diameter of 1 inch and pitch of 0.04 m. The heat transfer coefficient for the in-built heat exchanger within the fixed bed reactor was given by an equation derived by Penny et al. [202]:

$$\frac{h_{HX} d_t}{k_{eff}} = \left(0.333 + 0.26 {Re_{d_t}}^{0.533}\right) Pr^{0.33} \left(\frac{d_t}{d_p}\right)^{0.1} \quad (4\text{-}8)$$

where h_{HX} is the heat transfer coefficient, d_t is the heat exchanger tube diameter, k_{eff} is the effective thermal conductivity, Pr is the Prandtl number and d_p is the sorbent particle diameter. Re_{d_t} is the Reynolds number given by:

$$Re_{d_t} = \frac{d_t \rho_g v_g}{\mu_g} \quad (4\text{-}9)$$

where ρ_g is the gas density, v_g is the superficial gas velocity and μ_g is the gas viscosity.

It was shown in previous work that steam regeneration lowers the desorption temperature and promotes this MOF's stability [195]. Hence direct steam, which is extracted

from the NGCC power plant, is passed through the reactor during the desorption step. The Dual-site Sips isotherm model was incorporated into the fixed bed reactor model using Aspen Custom Modeler. With the help of the cycle organizer feature in Aspen Adsorption™, the reactor bed model was designed to continuously cycle through a 4-step process: adsorption, steam pre-heating, desorption, and cooling. Adsorption was set to occur until the bed was fully saturated with CO_2, followed by steam entering the bed for 120 seconds. Desorption was specified to continue until the average concentration of CO_2 in the bed decreased to 0.25 mol/kg. Finally, the cooling step used the heat exchangers to bring the bed temperature back down to 50 °C.

Mass transfer in the bed reactor was modeled using the following mass transfer coefficients:

$$\frac{1}{k_{OC}} = \frac{r_p^2}{15\varepsilon_p D_{eff}} + \frac{1}{k_{chem}} \tag{4-10}$$

$$\frac{1}{k_{OP}} = \frac{r_p^2}{15 D_{eff}} + \frac{1}{k_{phys}} \tag{4-11}$$

where k_{OC} and k_{OP} are the overall mass transfer coefficients for chemisorption and physisorption, respectively, r_p is the sorbent particle radius, and D_{eff} is the effective particle diffusion given by

$$D_{eff} = C_1 (T_S)^{0.5} \tag{4-12}$$

C_1 is a constant and T_S is the temperature [K]. The value of C_1 is the same value used in Hughes et al. [200] since the diamine-appended MOF material used in their work was similar in structure

and properties as the tetramine-appended MOF studied in this work. C_1 was optimally estimated by using experimental breakthrough data.

The parameters k_{chem} and k_{phys} are the mass transfer coefficients for chemisorption and physisorption given by

$$k_{chem} = k_{chem,0}\, exp\left[\frac{-E_{chem}}{RT_0}\left(\frac{T_0}{T} - 1\right)\right] \tag{4-13}$$

$$k_{phys} = k_{phys,0}\, exp\left[\frac{-E_{phys}}{RT_0}\left(\frac{T_0}{T} - 1\right)\right] \tag{4-14}$$

where $k_{chem,0}$, $k_{phys,0}$, E_{chem} and E_{phys} are fitted parameters, R is the ideal gas constant, T_0 is the reference temperature (285 K for our model), and T is the operating temperature [200]. The value of the fitting parameters, $k_{chem,0}$, $k_{phys,0}$, E_{chem} and E_{phys}, is the same as in Hughes et al., where these parameters were optimally estimated by using the experimental thermogravimetric analysis data for the powdered material. The CO_2 adsorption rate can be expressed as the summation of the chemisorption and physisorption rates:

$$\frac{dq_{CO_2}}{dt} = k_{chem}(q^*_{chem} - q_{chem}) + k_{phys}(q^*_{phys} - q_{phys}) \tag{4-15}$$

where $q_{chem}\ and\ q_{phys}$ are chemisorption and physisorption loadings, respectively, and q^*_{chem} and q^*_{phys} are predicted loadings at equilibrium given by the dual-site Sips model.

The Ergun equation was used to determine the pressure drop across the reactor bed:

$$\frac{\Delta P}{L} = \frac{150\mu_g(1-\varepsilon)^2 v_g}{\varepsilon^3 d_p^2} + \frac{1.75(1-\varepsilon)\rho_g v_g^2}{\varepsilon^3 d_p} \quad (4\text{-}16)$$

where μ_g is the gas viscosity, ε is the voidage, v_g is the superficial velocity of the gas, d_p is the diameter of the MOF particles and ρ_g is the gas density.

The equation for calculating the CO_2 capture rate of the adsorber bed is:

$$Adsorber\ CO_2\ capture\ rate\ = mean\left(\frac{(\dot{N}_{CO2})_{in,ads} - (\dot{N}_{CO2})_{out,ads}}{(\dot{N}_{CO2})_{in,ads}}\right) x\ 100\% \quad (4\text{-}17)$$

where $(\dot{N}_{CO2})_{in,mem}$ is the flow-rate of CO_2 from the NGCC exhaust into the membrane system [mol/s] and $(\dot{N}_{CO2})_{out,ads}$ is the flow-rate of CO_2 out of the adsorber bed [mol/s]. The time-average of the terms in the parentheses is taken over the adsorption cycle to obtain the mean CO_2 capture rate over the entire adsorption process. Net-zero operation occurs when Equation (4-17) gives 100% and net-negative operation occurs when it exceeds 100% (which can only occur when less than 400 ppm CO_2 exists in the adsorber outlet stream). Note that the CO_2 that enters the carbon capture systems via air is subtracted off from inlet stream terms- $(\dot{N}_{CO2})_{in,mem}$ and $(\dot{N}_{CO2})_{in,ads}$ to ensure that 100% capture is attained when the outlet exhaust stream has 400 ppm CO_2.

A key assumption made in this model is that the adsorption behavior of the tetraamine-appended Mg_2(dobpdc) MOF material does not change significantly with a shift to lower operating temperatures. The experimental isotherm data collected for the MOF material ranged from 90 to 120 °C, while the adsorber beds in this carbon capture system would ideally operate between 50 and 150 °C. In order to extrapolate these isotherms to these temperatures, we

assumed that the general shape of the isotherm curves remained unchanged.[1] We also assumed that the linear driving force kinetic model used by Hughes et al. [200] could be applied to this MOF since the MOF material used in their work was similar in structure and properties. It was also assumed that CO_2 is the only gas species to be significantly adsorbed by the MOF sorbent used in this system since the tetraamine-appended MOF was shown to be highly selective for CO_2 [193], [195].

4.3 Results and Discussion

In this section, the optimal sorbent bed conditions are first determined through a series of optimizations (Section 4.3.1). Mode 1 & 2 simulations are then performed using this optimal bed design to determine key outputs such as cycle times and CO_2 capture rates (Section 4.3.2). Finally, ambient air is added to the Mode 2 bed at varying flow rates to determine how excess air impacts bed performance (Section 4.3.3).

4.3.1 Optimizations

Optimizations were run in order to determine the best set of conditions and parameters for the fixed bed reactors that would result in the highest CO_2 bed loadings, shortest cycle times, and lowest costs. Table 7 lists some of the fixed parameters used in these simulations, some of which have been adopted from Hughes et al.'s work [200] due to the similarities of the MOF sorbents used. The three variable input parameters that are studied here are: bed diameter and number of beds (Section 4.3.1.1), inlet gas pressure (Section 4.3.1.2), and steam flow rate and

[1] This assumption has been backed by Dr. Long's group through verbal communication, who are also planning to publish data for isotherms at a lower temperature range in the near future.

pressure (Section 4.3.1.3). A summary of the optimized values for these variable input parameters is given at the end of this section in Table 8.

Table 7: Fixed parameters for the optmizations performed on the fixed bed reactor in this section. Bed height, bed voidage, particle diameter and bulk sorbent density values have been taken from Hughes et al. [200]

Parameter	Value	Units
Bed Height, h	10	m
Bed Voidage, ε	0.68	-
MOF Particle Diameter, d_p	525	μm
Bulk Sorbent Density, ρ_s	315.35	kg/m^3
Adsorption Bed Temperature	50	°C
Desorption Bed Temperature	150	°C
Inlet Gas Temperature	30	°C
Steam Temperature	139.85	°C
Steam Pressure	1.5	bar
Number of Nodes in Bed	80	-

4.3.1.1 Bed Diameter and Number of Beds

The influence of the adsorber bed diameter and the number of beds on pressure drop is investigated here to determine the minimal number and size of adsorber beds needed to maintain a reasonable pressure drop. Figure 37 shows the effects of changing the bed diameter

and the number of beds on the pressure drop across the beds. In Figure 37A, we fixed the number of adsorber beds to 10 and varied the bed diameter. As expected, pressure drop decreases significantly with respect to bed diameter, since pressure drop is proportional to gas velocity squared as shown in Equation (4-16), and gas velocity is inversely proportional to bed diameter squared for a fixed flowrate: $v_g = Q/(\pi D^2/4)$. We selected 5 meters as the optimal bed diameter based on these results because it is the smallest diameter that results in a pressure drop equal to 0.2 bars. Once we fixed the bed diameter to 5 meters, we varied the number of adsorber beds (Figure 37B). We decided to proceed with 10 adsorber beds based on these results because increasing the number of beds beyond 10 would result in excess capital cost with minimal operating cost gain (since pressure drop is already pretty low at 10 beds). Note that there would need to be more than 10 fixed beds total for our system since 10 are allocated for adsorption at a given time. Therefore, a few more beds will be needed to undergo the pre-heating, desorption and cooling steps in addition to the 10 beds undergoing adsorption. The exact number of total beds will be determined later in this paper.

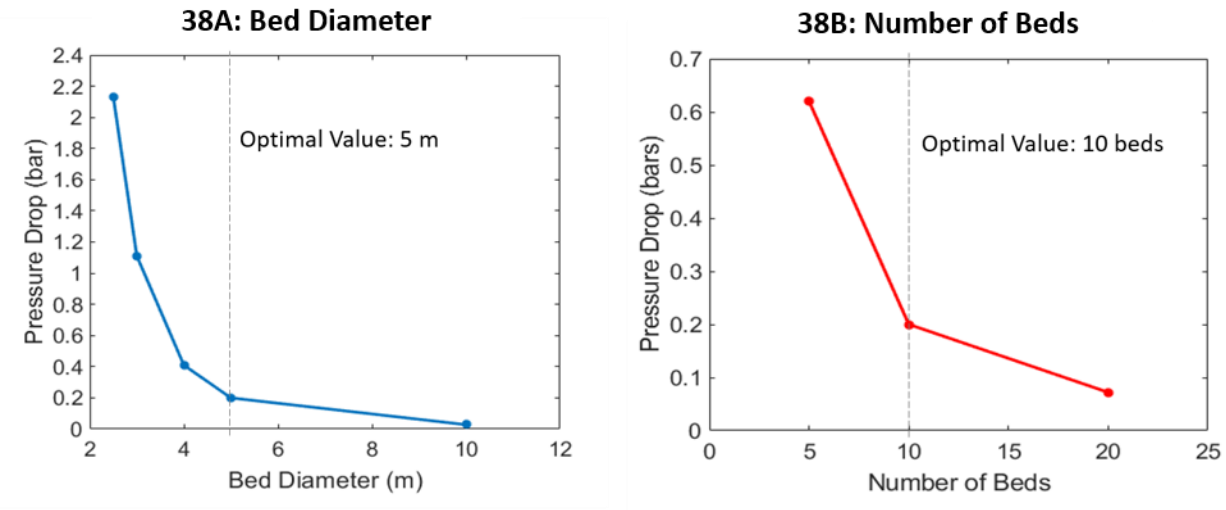

Figure 37: Pressure drop as a function of bed diameter, assuming 10 adsorber beds (37A, left), and as a function of number of adsorber beds of 5 m diameter (37B, right).

4.3.1.2 Inlet Pressure

Although pressurizing gas is typically not worth the added operating cost in traditional carbon capture systems, we have a unique design where excess electricity is available to our carbon capture system during off-peak NGCC operation (Mode 2). Therefore, pressurizing the inlet gas stream to our adsorber system could be beneficial in this application since the electricity is essentially "free" to the carbon capture system. The effect of inlet gas pressure on CO_2 loading capacity was observed by running the fixed bed simulation at pressures ranging between 1.5-7.5 bars. The number of beds and their diameters, as well as steam flowrate, are kept fixed for this simulation at the optimal values determined. It can be seen from Figure 38 that the average CO_2 loading in the bed increases with respect to inlet pressure. Increasing the pressure from 2.5 bars

to 5 bars, for example, increases the average bed loading from 1.55 mol/kg to 2.37 mol/kg, which is a ~150% increase in loading for doubling the pressure. .

The effect of inlet gas pressure on cycle time also appears to be significant. The cycle time changes from 149 to 192 minutes for a climb from 2.5 to 5 bars, which is a ~130% change in cycle time for doubling the inlet gas pressure. Increasing the inlet pressure increases the partial pressure of CO_2 in the adsorbers, thus increasing the amount of CO_2 adsorbed and desorbed during each cycle and hence the adsorption and desorption times. Since the inlet pressure significantly affects both the average bed loading and the cycle time, it is essential to determine and set a value for the inlet pressure which will create a balance between the two numbers. Observations seemed to suggest that specifying the inlet stream's pressure to 5 bars provides a balanced value that maximizes the bed loading and minimizes the cycle time at the same time. Therefore, 5 bars was selected as the gas inlet pressure (as indicated by the vertical dashed line in Figure 38).

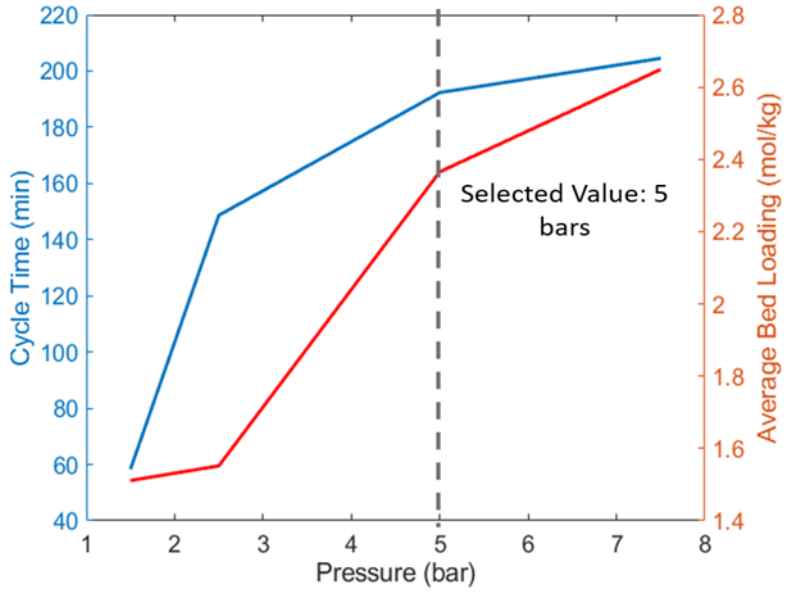

Figure 38: Final bed CO_2 loading (left y-axis, blue) and bed cycle time (right y-axis, red) as a function of inlet gas pressure. Both bed loading and cycle time increase minimally with respect to inlet gas pressure.

4.3.1.3 Steam Flow Rate and Pressure

The effects of steam flow rate and pressure on regeneration (desorption + cooling) time are investigated in this section. Figure 39A shows that increasing the steam flow rate leads to a significant drop in regeneration time, with a steep initial drop-off as steam flow rate approaches zero. The maximum practical limit for steam flow rate that could reasonably be extracted from our NGCC plant was 0.15 kmol/s (as indicated by the vertical dashed line in Figure 39A), so we selected that as our optimal value. The steam flowrate for each bed, presuming there are 10 beds, will then be 0.015 kmol/s. This value results in reasonably low regeneration times (~150 minutes). We also investigated the impact of steam pressure on regeneration time, as shown in Figure 38B. Raising steam pressure appears to have an adverse effect on regeneration time.

Therefore, we selected the lower limit (1.5 bars, shown with vertical dashed line in Figure 39B) as our optimal value to minimize regeneration time and avoid the energy penalty associated with pressuring the steam further.

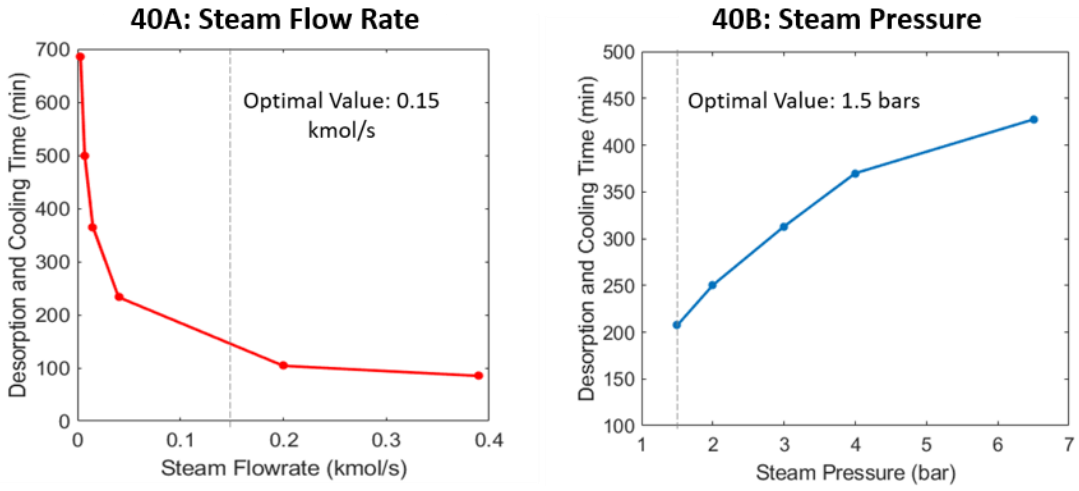

Figure 39: Desorption and cooling (regeneration) time as a function of steam flow rate (39A, left) and as a function of steam pressure (39B, right). Regeneration time decreases with increasing steam flow rate (39A), whereas it increases with steam pressure (39B).

4.3.1.4 Parameter Optimization Results

The optimal results based on varying bed diameter and number of beds (section 4.3.1.1), inlet gas pressure (Section 4.3.1.2), and steam flow rate and pressure (section 4.3.1.3) are summarized in Table 8. These values, in addition to the fixed values listed in Table 7, will serve as model inputs for the rest of the simulation results presented in this paper, unless otherwise stated.

Table 8: Summary of optimal values for input parameters varied in this section.

Parameter	Optimized Value	Units
Inlet Gas Pressure	4.9	bar
Steam Flow Rate	0.015	kmol/s
Steam Pressure	1.5	bar
Bed Number	10	-
Bed Diameter	5	m

4.3.2 Bed Performance in Modes 1 & 2

Now that the adsorber bed design has been optimized (section 4.3.1), we will use the optimal input values (listed in Table 8) along with the fixed input values (listed in Table 7) to simulate our system under NGCC hybrid conditions. More specifically, we will run our sorbent bed model in both Mode 1 & Mode 2 (as shown in Figure 33) to determine how it will perform under these conditions. The only inputs to our model that vary between Modes 1 & 2 are the inlet gas flow rate and mole fractions. In Mode 1, the inlet gas feed is purely membrane carbon capture exhaust, whereas in Mode 2, the inlet gas feed is a mixture of membrane exhaust, compressed air off the NGCC compressor and pressurized ambient air drawn in from the surroundings. We will also study the impact of adding increasing amounts of ambient air from the surroundings in Section 4.3.3. Values for the input parameters of the gas inlet stream entering the bed for Modes 1 and 2 are shown in Table 9. As seen from Table 8, the inlet gas molar flow rate increases when transitioning from Mode 1 to Mode 2 because of the addition of compressed

air from the NGCC power plant and inlet ambient air during Mode 2. The CO_2, H_2O, N_2 and O_2 mole fractions also vary between Modes 1 and 2 due to air being added to the membrane exhaust gas in Mode 2.

These values were obtained by running a complex optimization on the integrated NGCC + membrane + solid sorbent system in each mode of operation. Details about this rigorous optimization will be provided in a future publication by our team. As seen from Table 9, the inlet gas molar flow rate increases when transitioning from Mode 1 to Mode 2 because of the addition of compressed air from the NGCC power plant and inlet ambient air during Mode 2. The CO_2, H_2O, N_2 and O_2 mole fractions also vary between Modes 1 and 2 due to air being added to the membrane exhaust gas in Mode 2.

Table 9: Inlet gas stream conditions for Mode 1 & Mode 2 simulations.

Input Gas Parameters	**Mode 1**	**Mode 2**
Inlet Gas CO_2 mole fraction	0.0132	0.0115
Inlet Gas H_2O mole fraction	0.0611	0.0787
Inlet Gas N_2 mole fraction	0.7942	0.8764
Inlet Gas O_2 mole fraction	0.1315	0.0334
Inlet Gas Molar Flow Rate, kmol/s	0.9158	1.382

Source(s) of gas	100% membrane exhaust	97.98% membrane exhaust 1.42% compressed air 0.60% ambient air

The fixed bed reactor is subdivided into 80 nodes in the flow direction, with Node 1 corresponding to the inlet at the bottom of the bed and Node 80 corresponding to the outlet at the top of the bed. CO_2 loading curves will be shown for five representative nodes in the following plots: Node 1, Node 10, Node 40, Node 70 and Node 80 (as shown in Figure 40). These nodes were selected to understand how CO_2 loading vs. time varies at different bed locations.

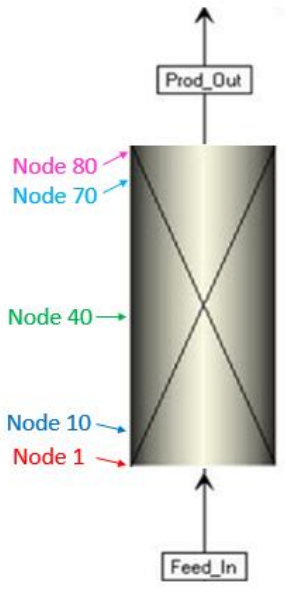

Figure 40: Graphic of fixed bed reactor with labeled nodes. The loading plots for these five representative nodes are shown for Mode 1 in Figure 42 and for Mode 2 in Figure 43.

Figure 41 shows the CO_2 loading profiles for Mode 1, where the five colored loading curves shown correspond to the five colored nodes shown in Figure 40. As expected, nodes closer to the inlet load with CO_2 earlier than nodes closer to the outlet. Furthermore, it can be seen that the nodes near the middle of the bed have higher final CO_2 loadings than the nodes at the inlet and outlet. This may be explained by the fact that the inlet gas stream enters the bed at 30 °C and takes a while to reach the bed temperature of 50 °C. Bed loading at the outlet (Node 80) is lower due to pressure drop and reduced CO_2 partial pressure at the end of the bed. During the Mode 1 cycle, 124.5 minutes are required for adsorption and 67.83 minutes are required for regeneration. Since the ratio of adsorption time to regeneration time is roughly 2:1 and we have 10 beds for adsorption, we would need to dedicate 5 more beds to regeneration (bringing the total number of system beds up to 15). This system design is depicted in Figure 43. The carbon capture rate of this adsorber system during Mode 1 operation 86.6% based on Equation (). When this system is combined with the membrane carbon capture system upstream, this results in a high overall carbon capture rate of 98.4% during Mode 1. These results are summarized along with Mode 2 carbon capture rates in Table 10.

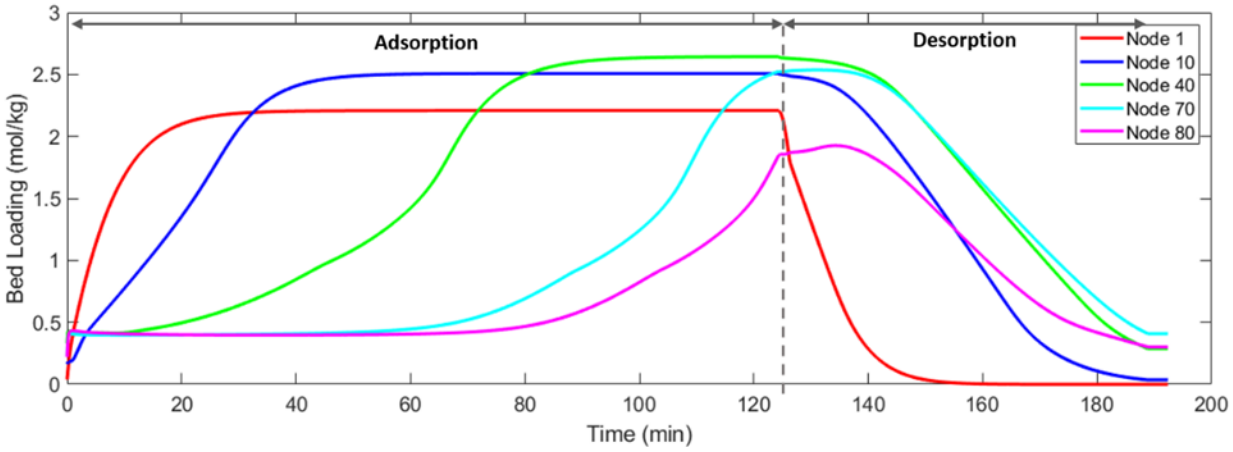

Figure 41 : MOF CO_2 loading vs. time in a fixed bed reactor for Mode 1 operation (NGCC power plant sending electricity to the grid). Bed loading is shown for five different nodes in the model (as shown in Figure 40: Node 1 (inlet node), Node 10, Node 40 (node half-way through the bed), Node 70 and Node 80 (outlet node). Total cycle time is 1902.33 minutes: 124.5 minutes for adsorption + 64.5 minutes for desorption + 3.33 minutes for cooling.

Mode 2 operation involved CO_2 adsorption from the membrane-based CCS system exhaust from the compressed air redirected from the NGCC power plant, and ambient air from the surroundings. Membrane exhaust accounts for 97.98% of the total input flow rate to the system, while compressed air from the NGCC plant accounts for 1.42% and ambient air accounts for 0.60%. The membrane exhaust (1,641,007 kg/hr) is determined by the flowrate of gases exiting the NGCC plant, the other percentages were limited by the amount of compressed air that could be drawn out from the NGCC plant (approximately 23,809 kg/hr) as well as from ambient air (10,000 kg/hr). As depicted in Figure 42, total cycle time during Mode 2 is approximately 160.67 minutes, with 96.33 minutes spent in adsorption and 64.34 minutes spent in regeneration. Mode 2 has a lower cycle time than Mode 1 because of the higher gas flow rate caused by the additional

air streams. The ratio of adsorption to regeneration time is approximately 2:1 for Mode 2 as well, meaning that the system design of 15 beds (10 adsorption + 5 regeneration) should work well for both modes (shown in Figure 43). Carbon capture rate for the solid sorbent system during Mode 2 was found to be 85.4%, and the overall carbon capture rate of the membrane + solid sorbent system in Mode 2 was 98.9%. These results are summarized along with the Mode 1 carbon capture results in Table 10. These results indicate that our hybrid system is capable of attaining near net-zero conditions. The system could theoretically approach net-zero or net-negative conditions if more ambient air were added to the mix, as explored in the next section.

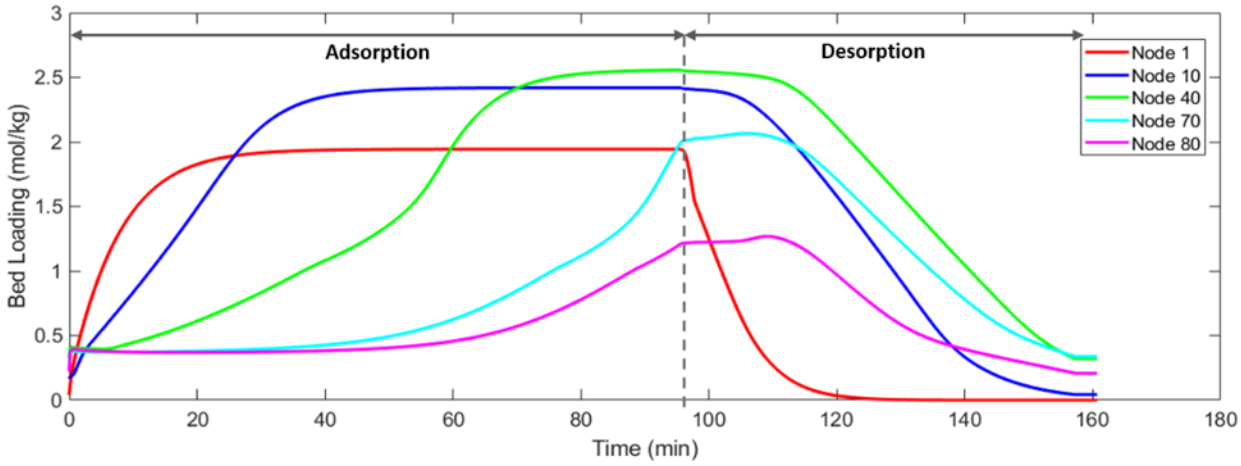

Figure 42: CO_2 loading in the MOF adsorber bed vs. time for Mode 2 operation (adsorber processes air in addition to membrane exhaust). Bed loading is shown for five different nodes in the model (depicted in Figure 40): Node 1 (inlet node), Node 10, Node 40 (node half-way through the bed), Node 70 and Node 80 (outlet node). Total cycle time is 160.67 minutes: 96.33 minutes for adsorption + 61 minutes for desorption + 3.34 minutes for cooling.

Table 10: Modes 1 & 2 capture rates for the sorbent system, membrane system and the overall capture system (comprised of both the solid sorbent and membrane systems).

	Mode 1	**Mode 2**
Solid Sorbent System	86.6%	85.4%
Membrane System	88.8%	92.6%
Overall Carbon Capture System	98.4%	98.9%

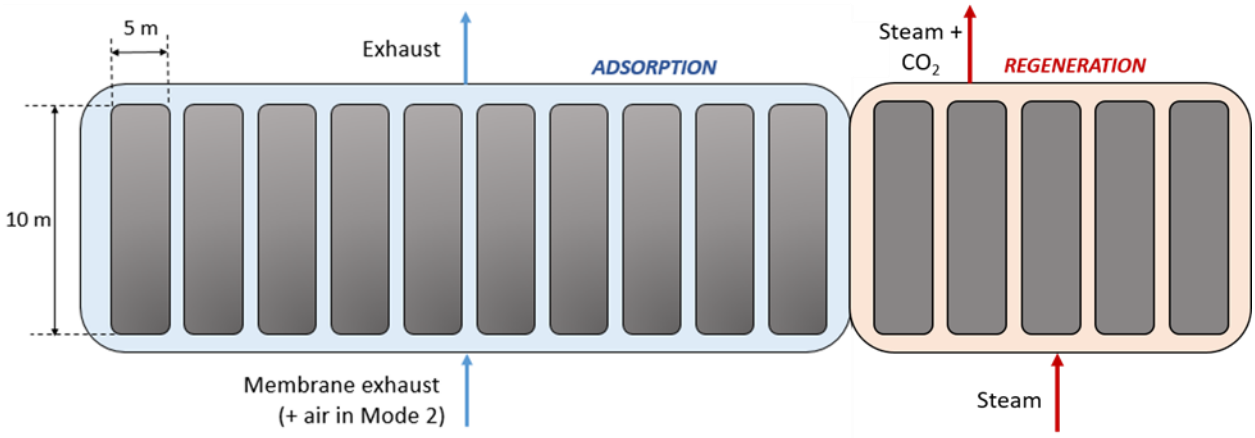

Figure 43: Design of solid sorbent carbon capture system, which consists of 15 beds (5 m diameter, 10 m height) filled with MOF solid sorbent spheres. 10 beds are undergoing adsorption from the membrane exhaust (mixed with air for Mode 2) at a given time, while 5 beds are undergoing steam regeneration. The beds remain fixed in space while the membrane exhaust and steam get routed to different beds on a timer.

4.3.3 Effect of Adding Excess Ambient Air in Mode 2

In Section 4.3.2, we demonstrated that 98-99% overall carbon capture efficiency is possible for our hybrid system. However, our system could theoretically attain 100+% efficiency (negative emissions) if it is able to remove enough CO_2 from air during Mode 2 to offset any CO_2 emitted during Mode 1. In Section 4.3.2, we assumed that the air input to the adsorber beds was 10,000 kg/hr pressurized ambient air and 23,809 kg/hr compressed air siphoned off the NGCC compressor. In this section, we study the effect of supplementing that stream with excess ambient air drawn in from the surroundings during Mode 2. To study the impact of excess ambient air on bed performance, we added ambient air in quantities such that 8%, 30% and 45% of the inlet gas stream entering the absorber bed consisted of ambient air, respectively.

Figure 44 shows the CO_2 loading of an average bed node (Node 40) vs. time for each of these air cases. The bed loadings for 8%, 30% and 45% excess ambient air are shown in comparison to 0.6% ambient air, which was the amount added for Mode 2 operation. Two trends are clear from Figure 44: 1) cycle time decreases as more air is added, and 2) CO_2 loading decreases as more air is added. These trends are correlated because cycle time decreases as a result of the bed reaching (lower) capacity sooner. The decrease in CO_2 loading with excess air is undesirable since the goal is to capture more CO_2 in order to reach negative emissions. However, the trend also makes sense because flooding the inlet stream with air lowers the partial pressure of CO_2 in the mixture, resulting in lower CO_2 capacity in the sorbent. Ultimately, the results in Figure 44 demonstrate that the MOF sorbent selected for our model performs worse under DAC conditions. Future work in this area should consider solid sorbents that are better suited for DAC than the one selected for this study.

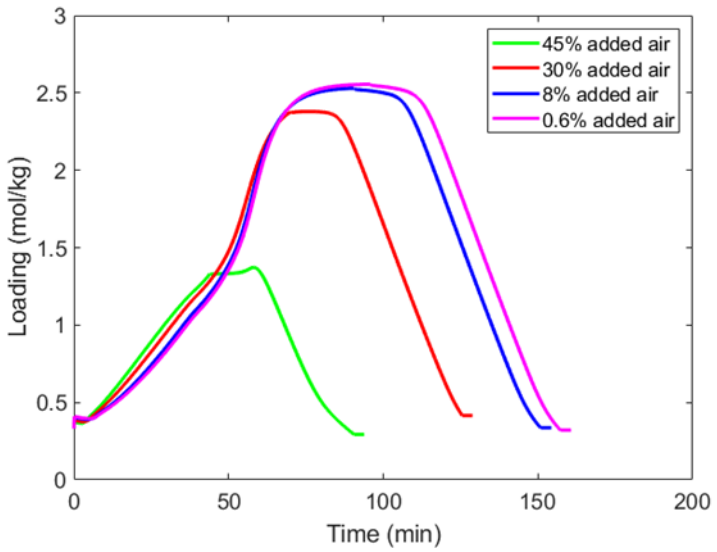

Figure 44: CO_2 bed loading at the middle of the bed (Node 40) as a function of time for four cases: added air in Mode 2 (0.6%), 8% added air, 30% added air, and 45% added air (where air is added to the adsorber bed inlet stream). CO_2 loading and cycle time decrease as more air is added because the lower partial pressure of CO_2 in the mixture reduces sorbent performance.

4.4 Conclusions

This work consisted of designing and optimizing the performance of a MOF fixed bed adsorber system coupled to an NGCC power plant and upstream membrane carbon capture system. The purpose of this fixed bed adsorber system is to capture excess CO_2 from the membrane exhaust during normal operation and to capture additional CO_2 from the air during off-peak hours. This novel hybrid carbon capture system could theoretically attain net-zero or net-negative CO_2 footprints for natural gas plants in the future by using CO_2 captured from air to offset any CO_2 emissions. However, we were unable to reach net-zero or net-negative emissions

in this study due to limitations in our solid sorbent selection and in the amount of compressed air that could be tapped from the compressor.

In order to optimize and investigate the performance of the fixed bed adsorber system, we fitted the Dual-site Sips isotherm model to published isotherm data for a high-performing MOF developed by Dr. Jeffrey Long's team at UC Berkeley. We embedded these isotherms into a fixed bed adsorber model in Aspen Adsorption™, which represents a single fixed bed adsorber cycling between adsorption and steam regeneration. We performed parametric variations on this model to determine the best input values that would result in minimal pressure drop, maximum CO_2 loading and minimum cycle time. We selected values of 5 meters for the bed diameter with 10 beds adsorbing in parallel, gas inlet pressure of 5 bars, and a steam flow rate and pressure of 0.15 kmol/s and of 1.5 bars, respectively. After the operating conditions and parameters were optimized, Modes 1 and 2 of operation were simulated, where Mode 1 corresponds to normal plant operation (sending power to the grid, capturing CO_2 from the power plant exhaust) and Mode 2 corresponds to off-peak operation (no power to the grid, fixed beds capture CO_2 from air from NGCC compressor and the surroundings in addition to exhaust). We found that the cycle times were 192.33 minutes and 160.67 minutes for Modes 1 & 2, respectively. These simulations also showed that the fixed bed adsorbers were able to attain carbon capture rates of 86.6% and 85.4% (for Modes 1 & 2), which correspond to overall capture rates of 98.4% and 98.9% (for Modes 1 & 2) when combined with the membrane carbon capture system. These results indicate that our hybrid carbon capture system is capable of attaining a near net-zero CO_2 footprint for an NGCC power plant.

This research emphasizes that near net-zero operation can be attained for a NGCC plant by using a hybrid carbon capture system that performs higher capture during off-peak hours. Future research should be conducted on alternate solid sorbents that can perform better under direct air capture conditions. Using a solid sorbent better suited for those conditions would enable much higher volumes of air to be processed by the fixed bed adsorbers, enabling it to potentially achieve net-zero or net-negative CO_2 emissions. Finally, future work should explore the techno-economic benefits of coupling direct air capture technology with natural gas infrastructure. By leveraging the steam, electricity and compressed air of NGCC plants, direct air capture operating costs could be significantly reduced.

5. Conclusions

The underlying goal of this thesis is to find ways to mitigate the effects of global warming and climate change. Increased industrialization has led to higher usage of fossil fuels and subsequent increase in global temperatures. One of the major contributing factors is the sharp increase in CO_2 levels, which must be curbed in order to control global warming. In an effort to offer a solution to this global problem, this thesis focuses on developing a new and sustainable method of harvesting renewable energy and promoting carbon capture to reduce the amount of CO_2 being emitted into the atmosphere. The first part of this thesis presents an overview of the different classes of piezoelectric materials and their applications, with an emphasis placed on sensor and energy harvesting technology. This review offers the scope to explore materials for piezoelectric energy harvesting, especially from renewable sources or from wasted energy. Piezoelectric materials are divided into the material classes of ceramics, polymers and composites, and it is concluded that composites are the most versatile of piezoelectric materials and therefore hold the greatest potential in a variety of applications since their properties can be adjusted to meet the requirement of the application. The second part of this thesis proposes two different models for piezoelectric energy harvesting from ocean waves in order to power buoys. Modeling and experimentation results show that though the indirect wave piezoelectric energy harvester model has a power output that is 4 orders higher than the direct model, when compared to other renewable sources like solar power, piezoelectric energy harvesting from ocean waves cannot yet compete in terms of cost. Since piezoelectric energy harvesting from ocean waves is still in the exploratory stage, work must be done to improve its performance by using enhanced piezoelectric materials or

by implementing a frequency conversion system that increases the frequency of the waves, thus enhancing the power output of the device. The last part of this thesis presents modeling work on carbon capture from an NGCC power plant using a solid sorbent adsorber system that undergoes temperature swing adsorption aided by steam. Input parameters are tested in the simulations in order to arrive at values such that near net-zero CO2 emissions could be achieved for the NGCC power plant when retrofitted with a hybrid carbon capture system consisting of a membrane capture system and a solid sorbent adsorber system. This could play a significant role in curbing CO2 emissions from power plants that run on fossil fuels.

All the projects involved in this thesis focus on promoting sustainability. Piezoelectric materials could potentially become a source of renewable energy for ocean buoys when they are used to harvest ocean wave energy. Though the results arrived at in this project are not very promising yet, they show that this technology holds potential. In the other project, carbon capture using a solid sorbent adsorber system in conjunction to a membrane capture system yields better capture rates than either of the systems working alone. Moreover, retrofitting this system to a natural gas combined cycle power plant can yield net-zero CO2 emissions and potentially negative emissions in the future, thus providing a cleaner way to use fossil fuels.

Bibliography

[1] K. S. Ramadan, D. Sameoto, and S. Evoy, “A review of piezoelectric polymers as functional materials for electromechanical transducers,” *Smart Mater. Struct.*, vol. 23, no. 3, 2014.

[2] J. Hao, W. Li, J. Zhai, and H. Chen, “Progress in high-strain perovskite piezoelectric ceramics,” *Mater. Sci. Eng. R Reports*, vol. 135, no. July 2018, pp. 1–57, 2019.

[3] J. F. Tressler, S. Alkoy, and R. E. Newnham, “Piezoelectric sensors and sensor materials,” *J. Electroceramics*, vol. 2, no. 4, pp. 257–272, 1998.

[4] T. R. Dargaville *et al.*, “Characterization, Performance and Optimization of PVDF as a Piezoelectric Film for Advanced Space Mirror Concepts,” 2005.

[5] H. Hoshyarmanesh and Y. Maddahi, “Poling Process of Composite Piezoelectric Sensors for Structural Health Monitoring: A Pilot Comparative Study,” *IEEE Sensors Lett.*, vol. 2, no. 1, pp. 1–4, 2018.

[6] C. Park, Z. Ounaies, K. E. Wise, and J. S. Harrison, “In situ poling and imidization of amorphous piezoelectric polyimides,” *Polymer (Guildf).*, vol. 45, no. 16, pp. 5417–5425, Jul. 2004.

[7] W. Tian, Z. Ling, W. Yu, and J. Shi, “A review of MEMS scale piezoelectric energy harvester,” *Appl. Sci.*, vol. 8, no. 4, pp. 1–20, 2018.

[8] R. Xu and S.-G. Kim, “Figures of Merits of Piezoelectric Materials in Energy,” *PowerMEMS*, pp. 464–467, 2012.

[9] W. Wersing, W. Heywang, and K. Lubitz, *Piezoelectricity Evolution and Future of a Technology*. 2008.

[10] T. S. Low and W. Guo, “Modeling of a three-layer piezoelectric bimorph beam with hysteresis,” *J. MEMS*, vol. 4, no. 4, p. 234, 1995.

[11] Z. Butt, R. A. Pasha, F. Qayyum, Z. Anjum, N. Ahmad, and H. Elahi, “Generation of

electrical energy using lead zirconate titanate (PZT-5A) piezoelectric material: Analytical, numerical and experimental verifications," *J. Mech. Sci. Technol.*, vol. 30, no. 8, pp. 3553–3558, 2016.

[12] X. Zhu, *Piezoelectric Ceramic Materials: Processing, Characterization, and Applications*, vol. 21, no. 1. New York, NY: Nova Science Publishers, 2010.

[13] T. Fujii, "Application of lead zirconate titanate thin film displacement sensors for the atomic force microscope," *J. Vac. Sci. Technol. B Microelectron. Nanom. Struct.*, vol. 13, no. 3, p. 1119, May 1995.

[14] A. Tawfik, O. M. Hemeda, A. M. A. Henaish, and A. M. Dorgham, "High piezoelectric properties of modified nano lead titanate zirconate ceramics," *Mater. Chem. Phys.*, vol. 211, pp. 1–8, 2018.

[15] M. Safaei, H. A. Sodano, and S. R. Anton, "A review of energy harvesting using piezoelectric materials: State-of-the-art a decade later (2008-2018)," *Smart Mater. Struct.*, vol. 28, no. 11, 2019.

[16] M. I. Rua Taborda *et al.*, "Key features in the development of unimorph stainless steel cantilever with screen-printed PZT dedicated to energy harvesting applications," *International Journal of Applied Ceramic Technology*, vol. 17, no. 6. pp. 2533–2544, 2020.

[17] S. Bai, Q. Xu, L. Gu, F. Ma, Y. Qin, and Z. L. Wang, "Single crystalline lead zirconate titanate (PZT) nano/micro-wire based self-powered UV sensor," *Nano Energy*, vol. 1, no. 6, pp. 789–795, 2012.

[18] H. Cho, J. Park, and J. Y. Park, "Micro-fabricated flexible PZT cantilever using d 33 mode for energy harvesting," *Micro Nano Syst. Lett.*, vol. 5, no. 1, pp. 4–8, 2017.

[19] K. Wasa, T. Matsushima, H. Adachi, I. Kanno, and H. Kotera, "Thin-film piezoelectric materials for a better energy harvesting MEMS," *J. Microelectromechanical Syst.*, vol. 21, no. 2, pp. 451–457, 2012.

[20] I. Smeltere, M. Antonova, M. Dunce, M. Livinsh, and B. Garbarz-glos, "Electrical and

mechanical properties of KNN based lead-free ceramics," *Solid State Phys.*, vol. 1, no. 3, pp. 5–7, 2011.

[21] J. Rödel, W. Jo, K. T. P. Seifert, E. M. Anton, T. Granzow, and D. Damjanovic, "Perspective on the development of lead-free piezoceramics," *J. Am. Ceram. Soc.*, vol. 92, no. 6, pp. 1153–1177, 2009.

[22] Y. Saito, H. Takao, and T. Tani, "Lead-free piezoceramics," *Nature*, vol. 432, no. November, pp. 2–5, 2004.

[23] P. Li *et al.*, "High-performance potassium-sodium niobate lead-free piezoelectric ceramics based on polymorphic phase boundary and crystallographic texture," *Acta Mater.*, vol. 165, pp. 486–495, 2019.

[24] P. Li *et al.*, "Ultrahigh Piezoelectric Properties in Textured (K,Na)NbO3-Based Lead-Free Ceramics," *Adv. Mater.*, vol. 30, no. 8, pp. 1–9, 2018.

[25] K. Uchino, *The development of piezoelectric materials and the new perspective*. Woodhead Publishing, 2010.

[26] J. Gao, D. Xue, W. Liu, C. Zhou, and X. Ren, "Recent Progress on BaTiO3-Based Piezoelectric Ceramics for Actuator Applications," *Actuators*, vol. 6, no. 3, p. 24, 2017.

[27] T. Karaki, K. Yan, T. Miyamoto, and M. Adachi, "Lead-free piezoelectric ceramics with large dielectric and piezoelectric constants manufactured from BaTiO3 nano-powder," *Japanese J. Appl. Physics, Part 2 Lett.*, vol. 46, no. 4–7, p. L97, Feb. 2007.

[28] W. Liu and X. Ren, "Large piezoelectric effect in Pb-free ceramics," *Phys. Rev. Lett.*, vol. 103, no. 25, p. 257602, Dec. 2009.

[29] G. A. Smolenski, V. A. Isupov, and A. I. Aganovskaya, "No Title," *J. Sov. Phys. Solid State*, vol. 2, no. 2651, 1961.

[30] K. Reichmann, A. Feteira, and M. Li, "Bismuth Sodium Titanate Based Materials for Piezoelectric Actuators," *Materials (Basel).*, vol. 8, pp. 8467–8495, 2015.

[31] H. He *et al.*, “Probing the Coexistence of Ferroelectric and Relaxor States in Bi0.5Na0.5TiO3-Based Ceramics for Enhanced Piezoelectric Performance,” *ACS Appl. Mater. Interfaces*, vol. 12, no. 27, pp. 30548–30556, 2020.

[32] I. L. Guy, S. Muensit, and E. M. Goldys, “Extensional piezoelectric coefficients of gallium nitride and aluminum,” *Appl. Phys. Lett.*, vol. 4133, no. June 1999, 1999.

[33] F. Gerfers *et al.*, “Sputtered AlN Thin Films for Piezoelectric MEMS Devices - FBAR Resonators and Accelerometers,” *Solid State Circuits Technol.*, no. January, 2010.

[34] M. Al Ahmad and R. Plana, “Vertical displacement detection of an aluminum nitride piezoelectric thin film using capacitance measurements,” *Int. J. Microw. Wirel. Technol.*, vol. 1, no. 1, pp. 5–9, 2009.

[35] B. R. Tittmann, D. A. Parks, S. O. Zhang, B. Tittman, D. A. Parks, and O. Zhang, “High Temperature Piezoelectrics - A Comparison,” *13th Int. Symp. Nondestruct. Characterisation Mater.*, no. May, pp. 20–24, 2013.

[36] E. Yarar, V. Hrkac, C. Zamponi, A. Piorra, L. Kienle, and E. Quandt, “Low temperature aluminum nitride thin films for sensory applications,” *AIP Adv.*, vol. 6, no. 7, 2016.

[37] S. Islam, “Piezoelectric and Dielectric Properties of LiNbO3, PMN-PT, and PZT-5A Materials at Cryogenic Temperatures,” University of Alberta, 2018.

[38] “Lithium Niobate - Boston Piezo-Optics Inc.” [Online]. Available: https://www.bostonpiezooptics.com/lithium-niobate. [Accessed: 11-Aug-2020].

[39] R. Wang, S. A. Bhave, and K. Bhattacharjee, “Design and fabrication of S0 Lamb-wave thin-film lithium niobate micromechanical resonators,” *J. Microelectromechanical Syst.*, vol. 24, no. 2, pp. 300–308, Apr. 2015.

[40] V. Plessky, S. Yandrapalli, P. J. Turner, L. G. Villanueva, J. Koskela, and R. B. Hammond, “5 GHz laterally-excited bulk-wave resonators (XBARs) based on thin platelets of lithium niobate,” *Electron. Lett.*, vol. 55, no. 2, pp. 98–100, Jan. 2019.

[41] Y. Yang, R. Lu, T. Manzaneque, and S. Gong, “Toward Ka Band Acoustics: Lithium Niobate Asymmetrical Mode Piezoelectric MEMS Resonators,” *IFCS 2018 - IEEE Int. Freq. Control Symp.*, pp. 21–25, 2018.

[42] M. McQUARRIE and F. W. BEHNKE, “Structural and Dielectric Studies in the System (Ba, Ca) (Ti, Zr)O3,” *J. Am. Ceram. Soc.*, vol. 37, no. 11, pp. 539–543, 1954.

[43] W. Liu and X. Ren, “Large piezoelectric effect in Pb-free ceramics,” *Phys. Rev. Lett.*, vol. 103, no. 25, p. 257602, Dec. 2009.

[44] S. Merselmiz *et al.*, “Design of lead-free BCZT-based ceramics with enhanced piezoelectric energy harvesting performances,” *Phys. Chem. Chem. Phys.*, vol. 24, no. 10, pp. 6026–6036, 2022.

[45] C. Shu, C. Q. Wang, S. Luo, and D. Y. Zheng, “Effects of BNT precursor prepared by molten salt method on BCZT-based lead-free piezoelectric ceramics,” *J. Mater. Sci. Mater. Electron.*, vol. 33, no. 8, pp. 5456–5467, 2022.

[46] Q. Li *et al.*, “Enhanced ferroelectric and piezoelectric responses of (Ba0.85Ca0.15)(Zr0.1Ti0.9)O3 ceramics by Tm3+ amphoteric substitution,” *Mater. Chem. Phys.*, vol. 252, no. May, 2020.

[47] L. Zhang *et al.*, “High-temperature stability of Ba0.99Ca0.01Zr0.02Ti0.98O3-doped LiTaO3 lead-free ceramics,” *J. Mater. Sci. Mater. Electron. 2022*, pp. 1–8, Feb. 2022.

[48] R. Agrawal and H. D. Espinosa, “Giant piezoelectric size effects in zinc oxide and gallium nitride nanowires. A first principles investigation,” *Nano Lett.*, vol. 11, no. 2, pp. 786–790, 2011.

[49] J. Zhou *et al.*, “Mechanical-electrical triggers and sensors using piezoelectric micowires/nanowires,” *Nano Lett.*, vol. 8, no. 9, pp. 2725–2730, 2008.

[50] L. Z. Kou, W. L. Guo, and C. Li, “Piezoelectricity of ZNO and its nanostructures,” *2008 Symp. Piezoelectricity, Acoust. Waves, Device Appl. SPAWDA 2008*, pp. 354–359, 2008.

[51] Z. L. Wang and J. Song, “Piezoelectric nanogenerators based on zinc oxide nanowire arrays,” *Science (80-.).*, vol. 312, no. 5771, pp. 242–246, 2006.

[52] Q. He, X. Li, J. Zhang, H. Zhang, and J. Briscoe, “P–N junction-based ZnO wearable textile nanogenerator for biomechanical energy harvesting,” *Nano Energy*, vol. 85, no. December 2020, p. 105938, 2021.

[53] A. Nechibvute, A. Chawanda, and P. Luhanga, “Piezoelectric Energy Harvesting Devices: An Alternative Energy Source for Wireless Sensors,” *Smart Mater. Res.*, vol. 2012, pp. 1–13, 2012.

[54] J. Ryu *et al.*, “Ubiquitous magneto-mechano-electric generator,” *Energy Environ. Sci.*, vol. 8, no. 8, pp. 2402–2408, 2015.

[55] S. K. Ghosh and D. Mandal, “High-performance bio-piezoelectric nanogenerator made with fish scale,” *Appl. Phys. Lett.*, vol. 109, no. 10, 2016.

[56] Z. L. Wang and J. Song, “Piezoelectric Nanogenerators Based on Zinc Oxide Nanowire Arrays,” *Science (80-.).*, vol. 312, no. 5771, pp. 242–246, 2006.

[57] G.-T. Hwang *et al.*, “A reconfigurable rectified flexible energy harvester via solid-state single crystal grown PMN-PZT,” *Adv. Energy Mater.*, vol. 5, no. 10, pp. 1–8, 2015.

[58] G.-T. Hwang *et al.*, “Self-Powered Wireless Sensor Node Enabled by an Aerosol-Deposited PZT Flexible Energy Harvester,” *Adv. Energy Mater.*, vol. 6, no. 13, p. 1600237, 2016.

[59] H. Kozuka, S. Takenaka, H. Tokita, T. Hirano, Y. Higashi, and T. Hamatani, “Stress and cracks in gel-derived ceramic coatings and thick film formation,” *J. Sol-Gel Sci. Technol.*, vol. 26, no. 1–3, pp. 681–686, 2003.

[60] D. R. Patil, V. Annapureddy, J. Kaarthik, A. Thakre, J. Akedo, and J. Ryu, “Piezoelectric thick film deposition via powder/granule spray in Vacuum: A review,” *Actuators*, vol. 9, no. 3, 2020.

[61] D. Xue, Y. Zhou, H. Bao, C. Zhou, J. Gao, and X. Ren, “Elastic, piezoelectric, and dielectric properties of Ba(Zr0.2Ti0.8)O3-50(Ba0.7Ca0.3)TiO3Pb-free ceramic at the morphotropic phase boundary,” *J. Appl. Phys.*, vol. 109, no. 5, pp. 1–8, 2011.

[62] M.-K. Lee, B.-H. Kim, and G.-J. Lee, “Piezoelectric voltage constant and sensitivity enhancements through phase boundary structure control of lead-free (K,Na)NbO3-based ceramics,” *J. Eur. Ceram. Soc.*, May 2022.

[63] L. Egerton and D. M. Dillon, “Piezoelectric and Dielectric Properties of Ceramics in the System Potassium-Sodium Niobate,” *Ceram. Int.*, vol. 42, no. 9, pp. 438–442, 2012.

[64] R. Vaish, “Piezoelectric and pyroelectric materials selection,” *Int. J. Appl. Ceram. Technol.*, vol. 10, no. 4, pp. 682–689, 2013.

[65] R. Vaish, “Piezoelectric and pyroelectric materials selection,” *Int. J. Appl. Ceram. Technol.*, vol. 10, no. 4, pp. 682–689, 2013.

[66] “No Title,” in *IEEE 5th International Symposium on Micro Machine and Human Science proceedings*, 1994, p. 75.

[67] N. P. Maria Joseph Raj, A. Ks, G. Khandelwal, N. R. Alluri, and S. J. Kim, “A lead-free ferroelectric Bi0.5Na0.5TiO3 based flexible, lightweight nanogenerator for motion monitoring applications,” *Sustain. Energy Fuels*, vol. 4, no. 11, pp. 5636–5644, 2020.

[68] E. Taghaddos, H. Charalambous, T. Tsakalakos, and A. Safari, “Electromechanical properties of flash sintered BNT-based piezoelectric ceramic,” *J. Eur. Ceram. Soc.*, vol. 39, no. 9, pp. 2882–2888, 2019.

[69] Y. He, J. Guo, and T. Zhou, “A kind of high mechanical properties sodium potassium niobate base leadless piezoelectric ceramics material and its preparation method and application,” 2017.

[70] T. Herzog, S. Walter, S. Hillmann, and H. Heuer, “Aluminum Nitride Thin Films for High Frequency Smart Ultrasonic Sensor Systems,” in *18th World Conference on*

Nondestructive Testing, 2012.

[71] S. Tadigadapa and K. Mateti, “Piezoelectric MEMS sensors: State-of-the-art and perspectives,” *Meas. Sci. Technol.*, vol. 20, no. 9, 2009.

[72] J. F. Shackelford and W. Alexander, *The CRC Materials Science and Engineering Handbook*. 1992.

[73] R. Hou, D. Hutson, and K. J. Kirk, “Development of sputtered AlN thin film ultrasonic transducers for durable high temperature applications,” *51st Annu. Conf. Br. Inst. Non-Destructive Test. 2012, NDT 2012*, pp. 279–292, 2012.

[74] I. Coondoo *et al.*, “A comparative study of structural and electrical properties in lead-free BCZT ceramics: Influence of the synthesis method,” *Acta Mater.*, vol. 155, pp. 331–342, 2018.

[75] E. Broitman, M. Y. Soomro, J. Lu, M. Willander, and L. Hultman, “Nanoscale piezoelectric response of ZnO nanowires measured using a nanoindentation technique,” *Phys. Chem. Chem. Phys.*, vol. 15, no. 26, pp. 11113–11118, Jul. 2013.

[76] J. Cardoso, F. F. Oliveira, M. P. Proenca, and J. Ventura, “The influence of shape on the output potential of ZnO nanostructures: Sensitivity to parallel versus perpendicular forces,” *Nanomaterials*, vol. 8, no. 5, May 2018.

[77] M. A. Haque, M. P. Manoharan, A. V. Desai, and G. Neely, “Synthesis and elastic characterization of zinc oxide nanowires,” *J. Nanomater.*, vol. 2008, no. 1, 2008.

[78] H. Kawai, “The Piezoelectricity of Poly (vinylidene Fluoride),” *Jpn. J. Appl. Phys.*, vol. 8, no. 7, pp. 975–976, Jul. 1969.

[79] S. Bauer and F. Bauer, *Piezoelectricity*, vol. 114. Springer, Berlin, Heidelberg, 2008.

[80] Z. Ounaies, J. A. Young, and J. S. Harrison, “An overview of the piezoelectric phenomenon in amorphous polymers,” *ACS Symp. Ser.*, vol. 726, pp. 88–103, 1999.

[81] K. K. Sappati and S. Bhadra, “Piezoelectric polymer and paper substrates: A review,” *Sensors (Switzerland)*, vol. 18, no. 11, 2018.

[82] J. Gomes, J. Nunes, V. Sencadas, and S. Lanceros-Méndez, “Influence of the β-phase content and degree of crystallinity on the piezo-and ferroelectric properties of poly(vinylidene fluoride),” *Fac. Eng. Inf. Sci. - Pap. Part A*, p. 1, Jan. 2010.

[83] D. Singh, A. Choudhary, and A. Garg, “Flexible and Robust Piezoelectric Polymer Nanocomposites Based Energy Harvesters,” *ACS Appl. Mater. Interfaces*, vol. 10, no. 3, pp. 2793–2800, 2018.

[84] X. Liu, Y. Shang, J. Zhang, and C. Zhang, “Ionic Liquid-Assisted 3D Printing of Self-Polarized β-PVDF for Flexible Piezoelectric Energy Harvesting,” *ACS Appl. Mater. Interfaces*, vol. 13, no. 12, pp. 14334–14341, 2021.

[85] N. Soin *et al.*, “Novel ‘3-D spacer’ all fibre piezoelectric textiles for energy harvesting applications,” *Energy Environ. Sci.*, vol. 7, no. 5, pp. 1670–1679, 2014.

[86] S. M. Damaraju, S. Wu, M. Jaffe, and T. L. Arinzeh, “Structural changes in PVDF fibers due to electrospinning and its effect on biological function,” *Biomed. Mater.*, vol. 8, no. 4, 2013.

[87] A. M. Hudzik, “HYDROKINETIC OSCILLATORS FOR ENERGY HARVESTING VIA COUPLING POLYVINYLIDENE FLUORIDE (PVDF) AND ELECTROMAGNETICS,” University of Pittsburgh, 2009.

[88] J. Harrison and Z. Ounaies, “Piezoelectric polymers,” 2001.

[89] L. Persano *et al.*, “High performance piezoelectric devices based on aligned arrays of nanofibers of poly(vinylidenefluoride-co-trifluoroethylene),” *Nat. Commun.*, vol. 4, pp. 1610–1633, 2013.

[90] C. Li, P. M. Wu, S. Lee, A. Gorton, M. J. Schulz, and C. H. Ahn, “Flexible dome and bump shape piezoelectric tactile sensors using PVDF-TrFE copolymer,” *J. Microelectromechanical Syst.*, vol. 17, no. 2, pp. 334–341, 2008.

[91] V. Bhavanasi, V. Kumar, K. Parida, J. Wang, and P. S. Lee, “Enhanced Piezoelectric Energy Harvesting Performance of Flexible PVDF-TrFE Bilayer Films with Graphene Oxide,” *ACS Appl. Mater. Interfaces*, vol. 8, no. 1, pp. 521–529, 2016.

[92] S. Anwar, M. Hassanpour Amiri, S. Jiang, M. M. Abolhasani, P. R. F. Rocha, and K. Asadi, “Piezoelectric Nylon-11 Fibers for Electronic Textiles, Energy Harvesting and Sensing,” *Adv. Funct. Mater.*, vol. 31, no. 4, pp. 1–8, 2021.

[93] H. KAWAI and I. HENJI, “No Title,” *Oyo Buturi*, no. 39, p. 413, 1970.

[94] J. I. Scheinbeim, “Piezoelectricity in γ-form Nylon 11,” *J. Appl. Phys.*, vol. 52, no. 10, pp. 5939–5942, Oct. 1981.

[95] B. A. Newman, P. Chen, K. D. Pae, and J. I. Scheinbeim, “Piezoelectricity in nylon 11,” *J. Appli*, 1980.

[96] J. Wu, Y. Fu, G. H. Hu, S. Wang, and C. Xiong, “Effect of stretching on crystalline structure, ferroelectric and piezoelectric properties of solution-cast nylon-11 films,” *Polymers (Basel).*, vol. 13, no. 13, pp. 1–12, 2021.

[97] J. Simpson, Z. Ounaies, and C. Fay, “Polarization and Piezoelectric Properties of a Nitrile Substituted Polyimide,” in *Materials Research Society Symposium*, 1997, p. 6.

[98] G. M. Atkinson, R. E. Pearson, Z. Ounaies, C. Park, J. S. Harrison, and J. A. Midkiff, “Piezoelectric Polyimide Tactile Sensors,” *Bienn. Univ. Microelectron. Symp. - Proc.*, pp. 308–311, 2003.

[99] J. D. Sherman, J. Elloian, J. Jadwiszczak, and K. L. Shepard, “On the Temperature Dependence of the Piezoelectric Response of Prepoled Poly(vinylidene fluoride) Films,” *ACS Appl. Polym. Mater.*, vol. 2, no. 11, pp. 5110–5120, Nov. 2020.

[100] L. Yang *et al.*, “Preparation and characterization of a novel piezoelectric nanogenerator based on soluble and meltable copolyimide for harvesting mechanical energy,” *Nano Energy*, vol. 67, no. 104220, 2019.

[101] T. D. Usher, K. R. Cousins, R. Zhang, and S. Ducharme, “The promise of piezoelectric polymers,” *Polym. Int.*, vol. 67, no. 7, pp. 790–798, 2018.

[102] K. Kirjavainen, “Electromechanical film and procedure for manufacturing same,” 20-Nov-1984.

[103] A. Mohebbi, F. Mighri, A. Ajji, and D. Rodrigue, “Cellular Polymer Ferroelectret: A Review on Their Development and Their Piezoelectric Properties,” *Adv. Polym. Technol.*, vol. 37, no. 2, pp. 468–483, Mar. 2018.

[104] O. Hamdi, F. Mighri, and D. Rodrigue, “Piezoelectric cellular polymer films: Fabrication, properties and applications,” *AIMS Mater. Sci.*, vol. 5, no. 5, pp. 845–869, 2018.

[105] Z. Luo *et al.*, “Energy harvesting study on single and multilayer ferroelectret foams under compressive force,” *IEEE Trans. Dielectr. Electr. Insul.*, vol. 22, no. 3, pp. 1360–1368, 2015.

[106] Y. Cao, W. Li, and N. Sepulveda, “Performance of Self-Powered, Water-Resistant Bending Sensor Using Transverse Piezoelectric Effect of Polypropylene Ferroelectret Polymer,” *IEEE Sens. J.*, vol. 19, no. 22, pp. 10327–10335, 2019.

[107] C. Song *et al.*, “Multi-frequency sound energy harvesting using Helmholtz resonators with irradiated cross-linked polypropylene ferroelectret films,” *AIP Adv.*, vol. 11, no. 11, 2021.

[108] V. Kulichikhin, A. Semakov, E. Frenkin, A. Shabeko, and D. Tur, “Linear polyorganophosphazene films as flexible piezoelectrics and actuators,” *Polym. Sci. - Ser. B*, vol. 57, no. 6, pp. 687–701, 2015.

[109] V. Kulichikhin, A. Semakov, and D. Tur, “New flexible piezoelectrics and actuators based on polyorganophosphazenes,” *Sensors Actuators, A Phys.*, vol. 252, pp. 48–53, 2016.

[110] T. Furukawa, “Ferroelectric properties of vinylidene fluoride copolymers,” *Phase Transitions*, vol. 18, no. 3–4, pp. 143–211, Aug. 1989.

[111] S. Fotouhi, R. Akrami, K. Ferreira-Green, G. A. M. Naser, M. Fotouhi, and C. Fragassa,

"Piezoelectric PVDF sensor as a reliable device for strain/load monitoring of engineering structures," *IOP Conf. Ser. Mater. Sci. Eng.*, vol. 659, no. 1, 2019.

[112] K. Koga and H. Ohigashi, "Piezoelectricity and related properties of vinylidene fluoride and trifluoroethylene copolymers," *J. Appl. Phys.*, vol. 59, no. 6, pp. 2142–2150, Mar. 1986.

[113] H. Elahi, M. Eugeni, and P. Gaudenzi, "A review on mechanisms for piezoelectric-based energy harvesters," *Energies*, vol. 11, no. 7, 2018.

[114] R. G. Kepler and R. A. Anderson, "Ferroelectric polymers," *Adv. Phys.*, vol. 41, no. 1, pp. 1–57, Jan. 1992.

[115] A. Jain, S. J. Kumar, D. R. Mahapatra, and V. T. Rathod, "Development of P(VDF-Trfe) films and its quasi-static and dynamic strain response," *Int. J. Eng. Res. Technol.*, vol. 2, no. 12, pp. 2598–2605, 2013.

[116] F. Fang, S. C. Shan, and W. Yang, "A multipeak phenomenon of magnetoelectric coupling in Terfenol-D/P(VDF-TrFE)/Terfenol-D laminates," *J. Appl. Phys.*, vol. 108, no. 10, p. 104505, Nov. 2010.

[117] J. Simpson, Z. Ounaies, and C. Fay, "POLARIZATION AND PIEZOELECTRIC PROPERTIES OF A NITRILE SUBSTITUTED POLYIMIDE," *MRS Online Proc. Libr. , Vol. 459 Symp. Y – Mater. Smart Syst. II*, vol. 59, 1996.

[118] J. Sun, Z. Yu, X. Wang, and D. Wu, "Synthesis and performance of cyclomatrix polyphosphazene derived from trispiro-cyclotriphosphazene as a halogen-free nonflammable material," *ACS Sustain. Chem. Eng.*, vol. 2, no. 2, pp. 231–238, 2014.

[119] K. Uchino, *Advanced Piezoelectric Materials*, 2nd Editio. State College: Elsevier, 2017.

[120] D. P. Skinner, Newnham, Robert E., and L. E. Cross, "Connectivity and piezoelectric-pyroelectric composites," *Mat. Res. Bull.*, vol. 13, pp. 599–607, 1978.

[121] S. M. Pilgrim, R. E. Newnham, and L. L. Rohlfing, "Extension of the composite

nomenclature scheme," *Mat. Res. Bull.*, vol. 22, pp. 677–684, 1987.

[122] E. K. Akdogan, M. Allahverdi, and A. Safari, "Piezoelectric composites for sensor and actuator applications," *IEEE Trans. Ultrason. Ferroelectr. Freq. Control*, vol. 52, no. 5, pp. 746–775, 2005.

[123] K. K. Sappati and S. Bhadra, "Flexible Piezoelectric 0-3 PZT-PDMS Thin Film for Tactile Sensing," *IEEE Sens. J.*, vol. 20, no. 9, pp. 4610–4617, 2020.

[124] X. Lv *et al.*, "High-Performance 0-3 Type Niobate-Based Lead-Free Piezoelectric Composite Ceramics with ZnO Inclusions," *ACS Appl. Mater. Interfaces*, vol. 10, no. 36, pp. 30566–30573, 2018.

[125] T. Kitayama and S. Sugawara, "Piezoelectric and Pyroelectric of Polymer-Ferroelectrics Composites," *Study Comm Electron. Circuit Components Mater*, no. CPM72-17, 1972.

[126] S. H. Wankhade, S. Tiwari, A. Gaur, and P. Maiti, "PVDF–PZT nanohybrid based nanogenerator for energy harvesting applications," *Energy Reports*, vol. 6, pp. 358–364, 2020.

[127] G. Tian *et al.*, "Rich lamellar crystal baklava-structured PZT/PVDF piezoelectric sensor toward individual table tennis training," *Nano Energy*, vol. 59, no. February, pp. 574–581, 2019.

[128] S. Siddiqui *et al.*, "A durable and stable piezoelectric nanogenerator with nanocomposite nanofibers embedded in an elastomer under high loading for a self-powered sensor system," *Nano Energy*, vol. 30, no. October, pp. 434–442, 2016.

[129] Y. Yang *et al.*, "Flexible piezoelectric pressure sensor based on polydopamine-modified BaTiO3/PVDF composite film for human motion monitoring," *Sensors Actuators, A Phys.*, vol. 301, p. 111789, 2020.

[130] H. Fu and R. E. Cohen, "Polarization rotation mechanism for ultrahigh electromechanical response in single-crystal piezoelectrics," *Nature*, vol. 403, no. 6767, pp. 281–283, 2000.

[131] R. Zhang, W. Jiang, B. Jiang, and W. Cao, “Elastic, Dielectric and Piezoelectric Coefficients of Domain Engineered 0.70Pb(Mg1/3Nb2/3)O3-0.30 PbTiO3 Single Crystal,” *AIP Conf. Proc.*, vol. 3, 2002.

[132] S. Xu, Y. W. Yeh, G. Poirier, M. C. McAlpine, R. A. Register, and N. Yao, “Flexible piezoelectric PMN-PT nanowire-based nanocomposite and device,” *Nano Lett.*, vol. 13, no. 6, pp. 2393–2398, 2013.

[133] F. Wu, W. Cai, Y. W. Yeh, S. Xu, and N. Yao, “Energy scavenging based on a single-crystal PMN-PT nanobelt,” *Sci. Rep.*, vol. 6, no. February, pp. 1–10, 2016.

[134] B. Moorthy *et al.*, “Piezoelectric energy harvesting from a PMN-PT single nanowire,” *RSC Adv.*, vol. 7, no. 1, pp. 260–265, 2017.

[135] Y. Zhang *et al.*, “Flexible energy harvesting polymer composites based on biofibril-templated 3-dimensional interconnected piezoceramics,” *Nano Energy*, vol. 50, no. April, pp. 35–42, 2018.

[136] C. Jin *et al.*, “Flexible piezoelectric nanogenerators using metal-doped ZnO-PVDF films,” *Sensors Actuators, A Phys.*, vol. 305, pp. 1–28, 2020.

[137] J. Li *et al.*, “High Performance Piezoelectric Nanogenerators Based on Electrospun ZnO Nanorods/Poly(vinylidene fluoride) Composite Membranes,” *J. Phys. Chem. C*, vol. 123, no. 18, pp. 11378–11387, 2019.

[138] M. Wu *et al.*, “High-performance piezoelectric-energy-harvester and self-powered mechanosensing using lead-free potassium-sodium niobate flexible piezoelectric composites,” *J. Mater. Chem. A*, vol. 6, no. 34, pp. 16439–16449, 2018.

[139] L. Gu *et al.*, “Enhancing the current density of a piezoelectric nanogenerator using a three-dimensional intercalation electrode,” *Nat. Commun.*, vol. 11, no. 1, pp. 1–9, 2020.

[140] J. Wu, X. Chen, Z. Chu, W. Shi, Y. Yu, and S. Dong, “No Title,” *Appl. Phys. Lett.*, vol. 109, no. 173901, 2016.

[141] N. V. Viet, Q. Wang, and A. Carpinteri, “Development of an ocean wave energy harvester with a built-in frequency conversion function,” *Int. J. Energy Res.*, vol. 42, no. 2, pp. 684–695, Feb. 2018.

[142] F. A. Khan, N. Pal, and S. H. Saeed, “Review of solar photovoltaic and wind hybrid energy systems for sizing strategies optimization techniques and cost analysis methodologies,” *Renew. Sustain. Energy Rev.*, vol. 92, pp. 937–947, 2018.

[143] I. López, J. Andreu, S. Ceballos, I. Martínez De Alegría, and I. Kortabarria, “Review of wave energy technologies and the necessary power-equipment,” *Renew. Sustain. Energy Rev.*, vol. 27, pp. 413–434, Nov. 2013.

[144] A. LiVecchi, “Exploring Opportunities for Marine Renewable Energy in Maritime Markets,” Washington D.C., 2019.

[145] Office of Energy Efficieny and Renewable Energy, “Powering the Blue Economy: Exploring Opportunities for Marine Renewable Energy in Martime Markets,” 2019.

[146] N. O. and A. A. N. W. S. N. D. B. C. US Department of Commerce, “National Data Buoy Center.” [Online]. Available: https://www.ndbc.noaa.gov/. [Accessed: 02-Apr-2023].

[147] and M. National Academies of Sciences, Engineering, “Sustaining Ocean Observations to Understand Future Changes in Earth’s Climate,” The National Academies Press, Washngton D.C., Oct. 2017.

[148] P. Veers *et al.*, “Grand challenges in the science of wind energy,” *Science (80-.).*, vol. 366, no. 6464, Oct. 2019.

[149] W. I. Ibrahim, M. R. Mohamed, R. M. T. R. Ismail, P. K. Leung, W. W. Xing, and A. A. Shah, “Hydrokinetic energy harnessing technologies: A review,” *Energy Reports*, vol. 7, pp. 2021–2042, 2021.

[150] M. I. Yuce and A. Muratoglu, “Hydrokinetic energy conversion systems: A technology status review,” *Renew. Sustain. Energy Rev.*, vol. 43, pp. 72–82, Mar. 2015.

[151] A. Babarit, *Ocean wave energy conversion : resource, technologies and performance*. 2017.

[152] N. Delmonte, D. Barater, F. Giuliani, P. Cova, and G. Buticchi, "Review of oscillating water column converters," *IEEE Trans. Ind. Appl.*, vol. 52, no. 2, pp. 1698–1710, 2016.

[153] R. Xu, H. Wang, Z. Xi, W. Wang, and M. Xu, "Recent Progress on Wave Energy Marine Buoys," *J. Mar. Sci. Eng.*, vol. 10, no. 5, 2022.

[154] M. H. Gebreselassie, S. H. Alshafie, M. A. Abdal-Hafeez, and K. M. Ibrahim, "Application of piezoelectric energy harvesting with an industrial machine," *Proc. Int. Conf. Comput. Control. Electr. Electron. Eng. 2019, ICCCEEE 2019*, Sep. 2019.

[155] L. M. Miller, "Micro-scale piezoelectric vibration energy harvesting: from fixed-frequency to adaptable-frequency devices." 2012.

[156] F. Huet, V. Boitier, and L. Seguier, "Tunable Piezoelectric Vibration Energy Harvester With Supercapacitors for WSN in an Industrial Environment," *IEEE Sens. J.*, vol. 22, no. 15, pp. 15373–15384, Aug. 2022.

[157] Y. Zhang, Q. Lai, J. Wang, and C. Lü, "Piezoelectric Energy Harvesting from Roadways under Open-Traffic Conditions: Analysis and Optimization with Scaling Law Method," *Energies*, vol. 15, no. 9, 2022.

[158] R. Trafford, D. Russo, C. Clark, S. Shin, and J. L. Schmalzel, "Characterization of Piezoelectric Cantilever Beams for use in Roadside Vibration Energy Harvesting," *SAS 2019 - 2019 IEEE Sensors Appl. Symp. Conf. Proc.*, May 2019.

[159] V. Vivekananthan, N. R. Alluri, Y. Purusothaman, A. Chandrasekhar, and S. J. Kim, "A flexible, planar energy harvesting device for scavenging road side waste mechanical energy via the synergistic piezoelectric response of K0.5Na0.5NbO3-BaTiO3/PVDF composite films," *Nanoscale*, vol. 9, no. 39, pp. 15122–15130, Oct. 2017.

[160] X. Jiang, Y. Li, J. Li, J. Wang, and J. Yao, "Piezoelectric energy harvesting from traffic-induced pavement vibrations," *J. Renew. Sustain. Energy*, vol. 6, no. 4, 2014.

[161] K. Li, Q. He, J. Wang, Z. Zhou, and X. Li, “Wearable energy harvesters generating electricity from low-frequency human limb movement,” *Microsystems Nanoeng. 2018 41*, vol. 4, no. 1, pp. 1–13, Sep. 2018.

[162] Y. Liu *et al.*, “Piezoelectric energy harvesting for self-powered wearable upper limb applications,” *Nano Sel.*, vol. 2, no. 8, pp. 1459–1479, Aug. 2021.

[163] M. O. Kim *et al.*, “Flexible and multi-directional piezoelectric energy harvester for self-powered human motion sensor,” *Smart Mater. Struct.*, vol. 27, no. 3, p. 035001, Jan. 2018.

[164] R. W. Yeung, A. Peiffer, N. Tom, and T. Matlak, “Design, Analysis, and Evaluation of the UC-Berkeley Wave-Energy Extractor,” *J. Offshore Mech. Arct. Eng.*, vol. 134, no. 2, p. 021902, 2012.

[165] G. W. Taylor, J. R. Burns, S. A. Kammann, W. B. Powers, and T. R. Welsh, “The Energy Harvesting Eel: A Small Subsurface Ocean/River Power Generator,” *IEEE J. Ocean. Eng.*, vol. 26, no. 4, pp. 539–547, 2001.

[166] S. Pobering and N. Schwesinger, “A Novel Hydropower Harvesting Device,” in *2004 International Conference on MEMS, NANO and Smart Systems (ICMENS’04)*, pp. 480–485.

[167] P. M. Koola and A. Ibragimov, “The dynamics of wave carpet - A novel deep water wave energy design,” *Ocean. 2003 Celebr. Past... Teaming Towar. Futur.*, vol. 4, pp. 2288–2293, 2003.

[168] A. Jbaily and R. W. Yeung, “Piezoelectric devices for ocean energy: a brief survey,” *J. Ocean Eng. Mar. Energy*, vol. 1, no. 1, pp. 101–118, Feb. 2015.

[169] T. Connectivity, “LDT1-028K PIEZO SENSOR w/ Leads Attached,” 2015.

[170] R. Murray and J. Rastegar, “Novel two-stage piezoelectric-based ocean wave energy harvesters for moored or unmoored buoys,” 2009, vol. 7288, p. 72880E.

[171] “SolarLand Solar Panel 10W 12V - SLP010-12U .” [Online]. Available:

https://www.solarpanelstore.com/products/solarland-10w-12v. [Accessed: 21-Apr-2023].

[172] A. Kiani, K. Jiang, and P. Feron, “Techno-Economic Assessment for CO2 Capture From Air Using a Conventional Liquid-Based Absorption Process,” *Front. Energy Res.*, vol. 8, no. May, pp. 1–13, 2020.

[173] S. M. Hashemi, M. H. Sedghkerdar, and N. Mahinpey, “Calcium looping carbon capture: Progress and prospects,” *Can. J. Chem. Eng.*, vol. 100, no. 9, pp. 2140–2171, Sep. 2022.

[174] X. Shi *et al.*, “Sorbents for the Direct Capture of CO2 from Ambient Air,” *Angew. Chemie - Int. Ed.*, vol. 59, no. 18, pp. 6984–7006, 2020.

[175] J. Hansen, R. Ruedy, M. Sato, and K. Lo, “Global surface temperature change,” *Rev. Geophys.*, vol. 48, no. 4, pp. 1–29, 2010.

[176] N. J. L. Lenssen *et al.*, “Improvements in the GISTEMP Uncertainty Model,” *J. Geophys. Res. Atmos.*, vol. 124, no. 12, pp. 6307–6326, 2019.

[177] Z. He and L. A. Ricardez-Sandoval, “Dynamic modelling of a commercial-scale CO2 capture plant integrated with a natural gas combined cycle (NGCC) power plant,” *Int. J. Greenh. Gas Control*, vol. 55, pp. 23–35, Dec. 2016.

[178] M. E. Diego, J. M. Bellas, and M. Pourkashanian, “Techno-economic analysis of a hybrid CO2 capture system for natural gas combined cycles with selective exhaust gas recirculation,” *Appl. Energy*, vol. 215, no. February, pp. 778–791, 2018.

[179] C. A. Seipp, N. J. Williams, M. K. Kidder, and R. Custelcean, “CO2 Capture from Ambient Air by Crystallization with a Guanidine Sorbent,” *Angew. Chemie*, vol. 129, no. 4, pp. 1062–1065, 2017.

[180] K. S. Lackner, S. Brennan, J. M. Matter, A. H. A. Park, A. Wright, and B. Van Der Zwaan, “The Urgency of the Development of CO2 Capture from Ambient Air,” *Proc. Natl. Acad. Sci. U. S. A.*, vol. 109, no. 33, pp. 13156–13162, Aug. 2012.

[181] S. Choi, J. H. Drese, P. M. Eisenberger, and C. W. Jones, “Application of amine-tethered

solid sorbents for direct CO 2 capture from the ambient air," *Environ. Sci. Technol.*, vol. 45, no. 6, pp. 2420–2427, 2011.

[182] M. Realff *et al.*, "Positive Power with Negative Emissions: Flexible Ngcc Enabled By Modular Direct Air Capture (DAC)," in *AIChe Annual Meeting*, 2021.

[183] M. Sheha, E. Graham, and H. Herzog, "Steady State and Dynamic Modeling of a Flexible Carbon Capture-Equipped Power Plant Integrated with Lime-Based Direct Air Capture," in *AIChe Annual Meeting*, 2021.

[184] D. Gribble *et al.*, "Demo-scale testing of a hybrid membrane-sorbent system for post-combustion CO2 capture," *SSRN Electron. J.*, Oct. 2022.

[185] G. Alptekin, "Membrane-Sorbent Hybrid System for Post-combustion Carbon Capture," Nov. 2020.

[186] T. C. Merkel, H. Lin, X. Wei, and R. Baker, "Power plant post-combustion carbon dioxide capture: An opportunity for membranes," *J. Memb. Sci.*, vol. 359, no. 1–2, pp. 126–139, Sep. 2010.

[187] R. W. Baker, B. Freeman, J. Kniep, X. Wei, and T. Merkel, "CO2 capture from natural gas power plants using selective exhaust gas recycle membrane designs," *Int. J. Greenh. Gas Control*, vol. 66, pp. 35–47, Nov. 2017.

[188] T. C. Merkel, X. Wei, Z. He, L. S. White, J. G. Wijmans, and R. W. Baker, "Selective Exhaust Gas Recycle with Membranes for CO2 Capture from Natural Gas Combined Cycle Power Plants," *Ind. Eng. Chem. Res.*, vol. 52, no. 3, pp. 1150–1159, Jan. 2012.

[189] D. W. Keith, G. Holmes, D. St. Angelo, and K. Heidel, "A Process for Capturing CO2 from the Atmosphere," *Joule*, vol. 2, no. 8, pp. 1573–1594, 2018.

[190] M. M. Sadiq *et al.*, "A Pilot-Scale Demonstration of Mobile Direct Air Capture Using Metal-Organic Frameworks," *Advanced Sustainable Systems*, vol. 4, no. 12. 2020.

[191] A. R. Millward and O. M. Yaghi, "Metal-organic frameworks with exceptionally high

capacity for storage of carbon dioxide at room temperature," *J. Am. Chem. Soc.*, vol. 127, no. 51, pp. 17998–17999, Dec. 2005.

[192] J. R. Li, R. J. Kuppler, and H. C. Zhou, "Selective gas adsorption and separation in metal–organic frameworks," *Chem. Soc. Rev.*, vol. 38, no. 5, pp. 1477–1504, Apr. 2009.

[193] A. Sinha, L. A. Darunte, C. W. Jones, M. J. Realff, and Y. Kawajiri, "Systems Design and Economic Analysis of Direct Air Capture of CO2 through Temperature Vacuum Swing Adsorption Using MIL-101(Cr)-PEI-800 and mmen-Mg2(dobpdc) MOF Adsorbents," *Ind. Eng. Chem. Res.*, vol. 56, no. 3, pp. 750–764, 2017.

[194] T. M. McDonald, W. R. Lee, J. A. Mason, B. M. Wiers, C. S. Hong, and J. R. Long, "Capture of carbon dioxide from air and flue gas in the alkylamine-appended metal-organic framework mmen-Mg 2(dobpdc)," *J. Am. Chem. Soc.*, vol. 134, no. 16, pp. 7056–7065, 2012.

[195] E. J. Kim *et al.*, "Cooperative carbon capture and steam regeneration with tetraamine-appended metal-organic frameworks," *Science (80-.).*, vol. 369, no. 6502, pp. 392–396, 2020.

[196] M. Hefti, L. Joss, Z. Bjelobrk, and M. Mazzotti, "On the potential of phase-change adsorbents for CO2 capture by temperature swing adsorption," *Faraday Discuss.*, vol. 192, no. 0, pp. 153–179, Oct. 2016.

[197] J. Kundu, J. F. Stilck, J. H. Lee, J. B. Neaton, D. Prendergast, and S. Whitelam, "Cooperative Gas Adsorption without a Phase Transition in Metal-Organic Frameworks," *Phys. Rev. Lett.*, vol. 121, no. 1, p. 015701, Jul. 2018.

[198] K. N. Pai, J. D. Baboolal, D. A. Sharp, and A. Rajendran, "Evaluation of diamine-appended metal-organic frameworks for post-combustion CO2 capture by vacuum swing adsorption," *Sep. Purif. Technol.*, vol. 211, pp. 540–550, Mar. 2019.

[199] Z. Bao, L. Yu, Q. Ren, X. Lu, and S. Deng, "Adsorption of CO2 and CH4 on a magnesium-based metal organic framework," *J. Colloid Interface Sci.*, vol. 353, no. 2, pp. 549–556, Jan. 2011.

[200] R. Hughes *et al.*, “Isotherm, Kinetic, Process Modeling, and Techno-Economic Analysis of a Diamine-Appended Metal-Organic Framework for CO2Capture Using Fixed Bed Contactors,” *Energy and Fuels*, vol. 35, no. 7, pp. 6040–6055, 2021.

[201] R. L. Siegelman *et al.*, “Water Enables Efficient CO2 Capture from Natural Gas Flue Emissions in an Oxidation-Resistant Diamine-Appended Metal-Organic Framework,” *J. Am. Chem. Soc.*, vol. 141, no. 33, pp. 13171–13186, 2019.

[202] C. Penny, D. Naylor, and J. Friedman, “Heat transfer to small cylinders immersed in a packed bed,” *Int. J. Heat Mass Transf.*, vol. 53, no. 23–24, pp. 5183–5189, Nov. 2010.

[203] S. Voskian, P. Brown, C. Halliday, K. Rajczykowski, and T. A. Hatton, “Amine-Based Ionic Liquid for CO2Capture and Electrochemical or Thermal Regeneration,” *ACS Sustain. Chem. Eng.*, vol. 8, no. 22, pp. 8356–8361, 2020.

[204] S. Voskian and T. A. Hatton, “Faradaic electro-swing reactive adsorption for CO2 capture,” *Energy and Environmental Science*, vol. 12, no. 12. pp. 3530–3547, 2019.

[205] N. McQueen, K. V. Gomes, C. McCormick, K. Blumanthal, M. Pisciotta, and J. Wilcox, “A review of direct air capture (DAC): scaling up commercial technologies and innovating for the future,” *Prog. Energy*, vol. 3, no. 3, p. 032001, 2021.